Title
Scanning Tunneling Microscopy of Graphene Quantum Dots

Author
Lee, Juwon

Publication Date
2017

Peer reviewed|Thesis/dissertation

Scanning Tunneling Microscopy of Graphene Quantum Dots

by

Juwon Lee

A dissertation submitted in partial satisfaction of the
requirements for the degree of
Doctor of Philosophy

in

Physics

in the

Graduate Division

of the

University of California, Berkeley

Committee in charge:

Professor Michael F. Crommie, Chair
Professor Jeffrey Neaton
Professor Andrew Minor

Fall 2017

Abstract

Scanning Tunneling Microscopy of Graphene Quantum Dots

by

Juwon Lee

Doctor of Philosophy in Physics

University of California, Berkeley

Professor Michael F. Crommie, Chair

Quantum confinement of Dirac fermions is an important frontier in graphene research. In this dissertation, we report on our use of a scanning tunneling microscope (STM) to investigate electrostatically confined Dirac fermions in graphene quantum dots. We first describe a technique for patterning embedded gates in backgated graphene/hexagonal boron nitride (hBN) heterostructures by STM manipulation of defect charges within the hBN substrate. In conjunction with a tunable backgate, this allows us to engineer p-n junctions in monolayer and bilayer graphene whose geometries can be flexibly designed with nanoscale precision. Using scanning tunneling spectroscopy (STS), we image and spatially characterize the behavior of Dirac fermions in the vicinity of p-n junctions and show that circular p-n junctions in monolayer and bilayer graphene act as gate-tunable quantum dots with unique energy spectra. For monolayer graphene quantum dots, comparison with theoretical simulations of the massless Dirac equation enables us to identify each experimentally observed spectroscopic peak as a quantum dot eigenstate with a unique set of quantum numbers. In bilayer graphene, we demonstrate a gate-tunable evolution of locally gated graphene from classical dots to quantum dots and achieve control over the number of massive Dirac fermions contained in a quantum dot by using the STM tip as a top gate. Furthermore, we explore the electronic properties of quantum double dots and non-circular monolayer graphene p-n junctions using spatially resolved STS. Our work yields insight into the spatial behavior of Dirac fermions under the influence of local electrostatic potentials and provides a platform for further experimental investigation of physics related to p-n junctions in graphene.

Dedicated to my loving parents.

Contents

List of Figures

List of Abbreviations

2DEG	Two-Dimensional Electron Gas
a.c.	Alternating Current
hBN	Hexagonal Boron Nitride
$\mathrm{d}I/\mathrm{d}V_s$	Differential Tunneling Conductance
DOS	Electronic Density of States
DP	Dirac Point
e	Absolute Value of the Electron Charge
E_C	Charging Energy
E_{CNP}	Charge Neutrality Point Energy
E_D	Dirac Point Energy
E_F	Fermi energy
LDOS	Local Density of States
LT	Low Temperature
rms	Root Mean Square
QD	Quantum Dot
STM	Scanning Tunneling Microscopy *or* Scanning Tunneling Microscope
STS	Scanning Tunneling Spectroscopy
UHV	Ultrahigh Vacuum
V_g	Backgate Voltage
V_s	Sample Bias

Acknowledgments

As I reflect on the many individuals who have supported me throughout my academic career, I am overwhelmed with a deep sense of gratitude and indebtedness. First I must acknowledge that these relationships, as well as all other material and circumstantial blessings in my life, are unmerited favors graciously lavished on me by God. He is the very author of physical laws and the sustainer of my being, so I cannot but gladly acknowledge and give thanks to him in all things pertaining to my life including this dissertation. May I be granted a persevering faith, so that at the end of my ephemeral sojourn I may stand before the Creator unashamed, without regrets, and eternally magnifying the sacrifice of Jesus Christ on the cross. *Maranatha!*

Without the unwavering support of my family, none of my accomplishments would have been possible. My parents have been remarkable embodiments of selfless, unconditional love in my life. Remembering their sacrifice reduces me to tears and I only hope that I can live up to their loving example in the future. Vicky has been a caring older sister whose friendship I will always treasure. *Gam-sa-hab-ni-da.*

I am very grateful to have Professor Michael Crommie as my thesis advisor. I walked away from my first meeting with Mike impressed by his contagious excitement for science. This initial impression was confirmed in the subsequent years when every so often our intensely engaging subgroup meetings would prolong for several hours, leaving all graduate students exhausted except for Mike, who would move on to the next subgroup meeting unabated. Mike is a gifted educator who taught me the importance of developing clear, precise physical pictures and communicating ideas effectively by carefully thinking from the audience's perspective. Thank you Mike for your mentorship, for teaching me valuable skills that will stick with me for life, and for giving me the privilege of working in a collaborative, world-class research lab.

Dillon Wong is a studious physicist and a top-notch intellectual who taught me everything I know about STM experimentation. The countless hours I spent in the second floor basement of Birge were made tolerable in large part due to our lively exchange of ideas on a wide range of topics outside of physics. I enjoyed how the differences in our perspectives would often refine my own worldview. Dillon always made himself available as the go-to person when other graduate students needed clarification on a physical concept. Thank you Dillon for your generous offer of assistance and for your collaborative spirit.

Hsin-Zon Tsai is the most resourceful person in the lab who constantly helped me navigate through my time in the lab. Some researchers only focus on their own projects, but Hsin-Zon is an instinctive team player who goes beyond the call of duty to facilitate collaborations and to look after others in the lab sometimes even at the expense of his own efficiency. I cherish the many hours we spent together traveling, conversing over meals, and working out at the RSF. Thank you Hsin-Zon for your advices, your loyal friendship and for lending me umbrellas on rainy days.

Jairo Velasco Jr. is an exceptional scientist and a disciplined project executor. Thanks to Jairo's respectfully collaborative and meticulously methodical approach to research, our

collaboration has been highly effective and productive. Jairo loves to mentor younger scientists and would habitually give me career advice, which were considerate gestures that I deeply appreciated. Thank you Jairo for mentoring me to be a good scientist.

Salman Kahn is a talented and hard-working undergraduate researcher who was involved in so many projects that he deserves an honorary PhD. Thank you Salman for making our samples and for all your contributions.

Zahra Pedramrazi is an energetic and multitalented adventurer and scientist who became the successor of our STM. Thank you for your friendship and for inspiring me to rediscover my Korean roots.

In addition to close collaborators, there are many other individuals who have helped me or been important part of my graduate school experience. Thank you Giang Nguyen for connecting me to the Crommie lab when I came back from my leave of absence and giving me detailed advice. Chad Germany was friendly and fun company while he worked with us in B207. Thank you Chen Chen for inviting me and others over for hot pot and games, I enjoyed hanging out on many occasions and I wish I could have played more soccer with you. Thank you Trinity Joshi for your pleasant presence and for inviting me to my first Nepalese birthday party. Thank you Franklin Liou for helping me get signatures and submit this dissertation, I enjoyed traveling and eating out with you. Aaron Bradley kindly gave me helpful and practical career advice, it was very much appreciated. I also thank Sebastian Wickenburg for taking the time to answer my questions and giving me helpful advices. Long Ju is probably the best young experimentalist I know, I enjoyed our collaboration. It was great to see Patrick Forrester and Andrew Aikawa be plugged into the Crommie group and on their way to become great physicists. I enjoyed having Dan Rizzo drop by B207 with always pithy, humorous comments. Yi Chen was always a pleasant company and a great roommate at APS. Other members of the Crommie lab have also been valuable part of my time: Caihong Jia, Ivan Pechenezhskiy, Miguel Ugeda, Kacey Meaker, Jiong Lu, Yang Wang, Christopher Bronner, and Arash A. Omrani. Thank you all.

On the administrative side of things, Anne Takizawa has always been super helpful my whole time in the physics department. Lisa Partida was always very nice and helpful with various matters within the Crommie group. I also thank Donna Sakima and other administrative staff in the physics department.

Finally I would like to express my sincere appreciation for my qualifying exam and dissertation committee members: Professors Jeffrey Neaton, Andrew Minor, and Alessandra Lanzara. Thank you very much for so graciously and promptly agreeing to serve as committee members.

Chapter 1

Introduction

Monolayer and bilayer graphene are two-dimensional allotropes of carbon that have attracted much attention from researchers due to their unique and applicable electronic properties. In monolayer graphene, charge carriers behave like massless Dirac fermions with light-like energy dispersion[1, 2]. This provided a condensed matter analogue to quantum electrodynamics, creating an unprecedented testbed for otherwise inaccesible physics of the ultrarelativistic regime[3]. In bilayer graphene, quasiparticles behave like *massive* Dirac fermions with rich physical properties and additional tunability afforded by the layer degree of freedom. Even after more than a decade of intense research, numerous aspects of graphene's electronic properties remain active areas of study.

Charge localization is an important area of graphene research and is critical for understanding graphene's electronic properties and its incorporation into nanoelectronic devices. Since its discovery, various techniques have been employed to confine graphene quasiparticles such as etching, deposition of adatoms, and the use of magnetic fields[4–14]. An alternative method for charge carrier confinement is electrostatic gating. In the case of semiconductor heterojunctions, a precursor to graphene as a two-dimensional electronic system, gate-defined quantum dots produced scientific discoveries and technological applications for many years. This provides a strong incentive to explore whether electrostatically confined graphene charge carriers can be used to generate similarly rich physics and applications. In this dissertation, we report on our use of a scanning tunneling microscope (STM) to fabricate and study graphene quantum dots defined by gate-induced p-n junctions.

Recently there has been a resurgence of interest in electron-optic phenomena at graphene p-n junctions such as Veselago lensing[15, 16], whispering gallery modes[17–20], and cloaked electronic states[21, 22]. These unique phenomena are made possible in graphene by its rare electronic properties that continue to inspire experimental and theoretical investigations. Our work contributes to this direction of research by providing a platform for real-space wavefunction visualization of Dirac fermions within graphene p-n junctions of various geometries. This ability to obtain spatially resolved spectroscopic information should provide valuable insight into the distinct anisotropic distribution of Dirac fermions at graphene p-n junctions.

1.1 The Electronic Structure of Graphene

Monolayer graphene is a two-dimensional carbon crystal arranged in a triangular lattice with two-atom basis, as depicted in Figure 1.1. Linear energy-momentum dispersion and pseudospin chirality define monolayer graphene's unique electronic structure. Both of these properties emerge in a basic tight-binding model computation of graphene's band structure. The energy-momentum dispersion of graphene obtained from incorporating the first and the second nearest neighbors in a tight-binding model gives:[1, 2]:

$$E_{\pm}(\vec{k}) = \pm t\sqrt{3 + f(\vec{k})} - t\prime f(\vec{k}), \tag{1.1}$$

where

$$f(\vec{k}) = 2\cos\sqrt{3}k_y a + 4\cos\frac{\sqrt{3}}{2}k_y a\cos\frac{3}{2}k_x a, \tag{1.2}$$

t is the nearest neighbor hopping energy and $t\prime$ is the next nearest-neighbor hopping energy. This produces a band structure with two Dirac cones at K and $K\prime$ points [1]. The low-energy quasiparticle dynamics is determined by the states near the K and $K\prime$ points. Expanding about the K point using $k-p$ perturbation results in the two-dimensional massless Dirac Hamiltonian[1]:

$$\hat{H} = v_F\hat{\vec{\sigma}}\cdot\hat{\vec{p}} \tag{1.3}$$

where $\vec{\sigma}$ are Pauli matrices and $v_F \approx 1\times 10^6 m/s$ is a constant known as the Fermi velocity of graphene [23, 24]. Written more explicitly in matrix form, the Hamiltonian is:

$$\hat{H} = v_F\begin{pmatrix} 0 & p_x - ip_y \\ p_x + ip_y & 0 \end{pmatrix} = v_F|\vec{p}|\begin{pmatrix} 0 & e^{-i\phi} \\ e^{i\phi} & 0 \end{pmatrix}, \tag{1.4}$$

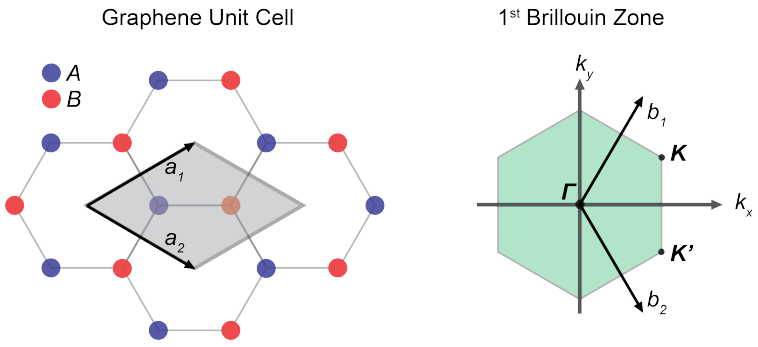

Figure 1.1: Crystal Structure of Monolayer Graphene (a) In graphene carbon atoms are arranged in a hexagonal honeycomb structure. The crystal structure is a triangular lattice with two-atom basis. The two points within a unit cell are referred to as sublattice A and sublattice B. a_1 and a_2 are the primitive vectors. (b) The first Brillouin zone is a regular hexagon. K and K' points are indicated on the diagram. b_1 and b_2 are the reciprocal primitive vectors.

where $e^{\pm i\phi} = \frac{p_x \pm i p_y}{|\vec{p}|}$. The eigenstates of this Hamiltonian are:

$$\psi_{e,h}(\vec{p}) = \frac{1}{\sqrt{2}} \begin{pmatrix} e^{-i\phi/2} \\ \pm e^{i\phi/2} \end{pmatrix}, \tag{1.5}$$

and the eigenenergies:

$$E(\vec{p}) = \pm v_F |\vec{p}|, \tag{1.6}$$

where + sign corresponds to electron states and − sign corresponds to hole states. Thus, graphene quasiparticles have a linear energy-momentum dispersion unlike typical metals and semiconductors that have parabolic band structures.

Another unique aspect of graphene's electronic structure is its chirality, which refers to the projection of pseudospin on momentum[3]. Applying the chirality operator on the quasiparticle eigenstates we obtain:

$$\frac{\hat{\vec{\sigma}} \cdot \hat{\vec{p}}}{|\vec{p}|} \psi_{e,h}(\vec{p}) = \frac{\hat{H}}{v_F |\vec{p}|} \psi_{e,h}(\vec{p}) = \pm \psi_{e,h}(\vec{p}), \tag{1.7}$$

where + (-) sign corresponds to electron (hole) states as before. This indicates that graphene electrons always have pseudospin and momentum in parallel direction, while graphene holes have pseudospin and momentum in anti-parallel directions. The expectation value of the pseudospin is:

$$< \hat{\sigma} >= \pm(\cos\phi, \sin\phi). \tag{1.8}$$

And the group velocity is:

$$\vec{v} = \nabla_{\vec{p}} E(\vec{p}) = \pm v_F \vec{p}/|\vec{p}|, \tag{1.9}$$

where + (-) sign corresponds to electron (hole) states.

1.1.1 Klein Tunneling

The unique band structure of graphene leads to a condensed matter analogue of a phenomenon in quantum electrodynamics known as the Klein paradox[3, 25–28]. Following an example outlined in [29], we examine a simple special case of graphene quasiparticle transmission across an electrostatic barrier that captures the fundamental aspects of Klein tunneling phenomena in graphene. As shown in Figure 1.2, an electrostatic potential $V(x)$ is applied to graphene, where

$$V(x) = \begin{cases} 0, \text{ for } x < 0 \\ V_0, \text{ for } x > 0 \end{cases} . \tag{1.10}$$

This electrostatic potential induces a p-n junction in graphene at $x = 0$ so that graphene is n-doped for $x < 0$ and p-doped for $x > 0$. To simplify computation, we consider the case when the total energy of a graphene quasiparticle E_0 is half of the potential step, i.e.

$E_0 = V_0/2$. Since $E = \hbar v_F k_F$, k_F has the same magnitude on both sides of the p-n junction. Following the scheme shown in Figure 1.2 (c), the incident, reflected, and transmitted waves can then be represented as follows:

$$\psi_{in} = \frac{1}{\sqrt{2}} \begin{pmatrix} e^{-i\phi/2} \\ e^{i\phi/2} \end{pmatrix} e^{ik_x x + ik_y y}, \tag{1.11}$$

$$\psi_{re} = \frac{r}{\sqrt{2}} \begin{pmatrix} e^{-i(\pi-\phi)/2} \\ e^{i(\pi-\phi)/2} \end{pmatrix} e^{-ik_x x + ik_y y}, \tag{1.12}$$

$$\psi_{tr} = \frac{t}{\sqrt{2}} \begin{pmatrix} e^{-i(\pi-\phi)/2} \\ -e^{i(\pi-\phi)/2} \end{pmatrix} e^{-ik_x x + ik_y y}. \tag{1.13}$$

The boundary condition at $x = 0$ implies $\psi_{in} + \psi_{re} = \psi_{tr}$. Plugging in above expressions for plane waves:

$$\frac{1}{\sqrt{2}} \begin{pmatrix} e^{-i\phi/2} \\ e^{i\phi/2} \end{pmatrix} + \frac{r}{\sqrt{2}} \begin{pmatrix} -ie^{i(\phi)/2} \\ ie^{-i(\phi)/2} \end{pmatrix} = \frac{t}{\sqrt{2}} \begin{pmatrix} -ie^{i(\phi)/2} \\ -ie^{-i(\phi)/2} \end{pmatrix}. \tag{1.14}$$

Matching the components of the spinor and solving the system of two equations we obtain:

$$r = -sin(\phi), t = icos(\phi). \tag{1.15}$$

The probability of transmission is:

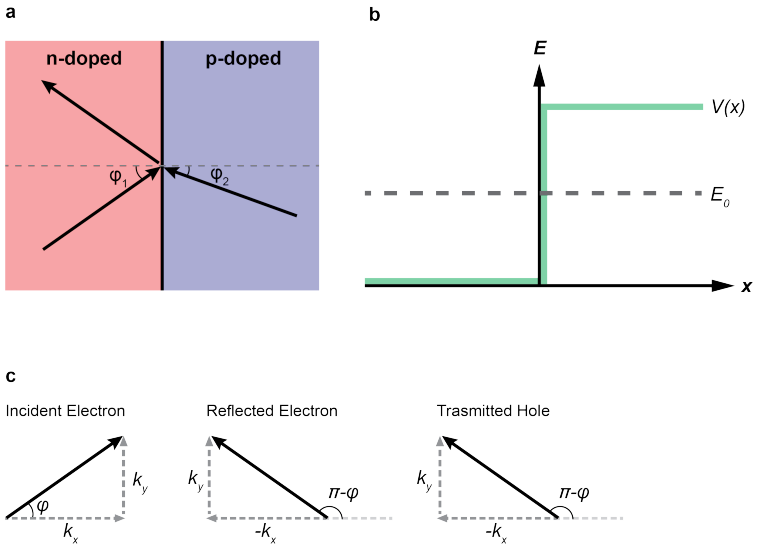

Figure 1.2: Particle Transmission across a Graphene P-N Junction (a) An electron is incident on a graphene p-n junction at angle ϕ_1. A hole is transmitted at angle ϕ_2. (b) The electrostatic potential $V(x)$ is a step function that jumps to a constant value at $x = 0$. The total energy of the particle is indicated by E_0. (c) Graphic representation of group velocity vectors of incident, reflected, and transmitted quasiparticles.

$$T = |t|^2 = cos^2(\phi). \tag{1.16}$$

The result above indicates that when a quasiparticle is normally incident on a p-n junction ($\phi = \pi/2$), the probabiliy of transmission becomes $T = 1$. This complete suppression of backscattering at normal incidence is referred to as Klein tunneling. A heuristic picture behind this effect is that the pseudospin of graphene quasiparticles must be conserved in a scattering process [3], which is a valid assumption for scattering potentials that vary slowly in the lengthscale of the graphene lattice constant. The perpendicularly incident electron has pseudospin pointing parallel to its momentum, which is in the same direction as the pseudospin of the forward scattering hole. The backscattering electron, however, has pseudospin pointing in the opposite direction. Therefore, pseudospin conservation prohibits backscattering and only allows forward scattering. In our toy model, the transmission coefficient is proportional to the dot product of the incident and transmitted spinors [29]:

$$< \psi_{in}|\psi_{tr} > \propto cos(\phi). \tag{1.17}$$

Hence, the transmission amplitude can be thought of as the 'overlap' of the pseudospin between the incident wave and the transmitted wave[29].

1.2 The Electronic Structure of Bilayer Graphene

Bilayer graphene consists of two layers of single layer graphene vertically stacked on top of each other. In this dissertation, we examine Bernal stacked bilayer graphene where a sublattices of the top layer lies directly on top of a sublattice of the bottom layer. Quasiparticles in bilayer graphene behave like *massive* Dirac fermions, providing a useful and interesting comparison to massless Dirac quasiparticles in monolayer graphene[2, 30]. Furthermore, the additional layer degree of freedom in bilayer graphene makes it possible to use vertical electric fields to tune its bandgap and modify the chiral properties of its charge carriers[31–35].

The massive Dirac fermions in gapless bilayer graphene are effectively governed by the following Hamiltonian[3]:

$$\hat{H} = \frac{1}{2m*}\begin{pmatrix} 0 & (p_x - ip_y)^2 \\ (p_x + ip_y)^2 & 0 \end{pmatrix} = \frac{|\vec{p}|^2}{2m*}\begin{pmatrix} 0 & e^{-2i\phi} \\ e^{2i\phi} & 0 \end{pmatrix}, \tag{1.18}$$

where $e^{\pm i\phi} = \frac{p_x \pm ip_y}{|\vec{p}|}$. And the energy eigenstates and eigenvalues of this Hamiltonian are:

$$\psi_{e,h}(\vec{p}) = \frac{1}{\sqrt{2}}\begin{pmatrix} e^{-i\phi} \\ \pm e^{i\phi} \end{pmatrix} \tag{1.19}$$

$$E(\vec{p}) = \pm\frac{|\vec{p}|^2}{2m*}, \tag{1.20}$$

where + sign corresponds to electron states and − sign corresponds to hole states.

Expectation value of pseudospin in bilayer graphene is:

$$< \hat{\sigma} >= \pm(\cos 2\phi, \sin 2\phi). \tag{1.21}$$

In bilayer graphene, pseudospin is a function of 2ϕ, in contrast to ϕ in monolayer graphene. And group velocity is:

$$\vec{v} = \pm\vec{p}/m*, \tag{1.22}$$

where + (-) sign corresponds to electron (hole) states.

In monolayer graphene, pseudospin conservation prohibited backscattering and led to unit transmission for normal incidence at p-n junctions. In bilayer graphene, the unique chiral nature of its massive Dirac fermions produces an opposite effect where transmission is completely suppressed. Here we show the essential aspects of anti-Klein tunneling by considering the same problem of particle transmission as we did for monolayer graphene shown in Figure 1.2, which was derived in Ref.[29]. For bilayer graphene, the incident, reflected, and transmitted waves can be represented as:

$$\psi_{in} = \frac{1}{\sqrt{2}} \begin{pmatrix} e^{-i\phi} \\ e^{i\phi} \end{pmatrix} e^{ik_x x + ik_y y}, \tag{1.23}$$

$$\psi_{re} = \frac{r}{\sqrt{2}} \begin{pmatrix} e^{-i(\pi-\phi)} \\ e^{i(\pi-\phi)} \end{pmatrix} e^{-ik_x x + ik_y y}, \tag{1.24}$$

$$\psi_{tr} = \frac{t}{\sqrt{2}} \begin{pmatrix} e^{-i(\pi-\phi)} \\ -e^{i(\pi-\phi)} \end{pmatrix} e^{-ik_x x + ik_y y}. \tag{1.25}$$

Imposing the boundary conditions at $x = 0$:

$$r = -\cos(2\phi), t = i\sin(2\phi). \tag{1.26}$$

The probability of transmission is:

$$T = |t|^2 = \sin^2(2\phi). \tag{1.27}$$

Thus, a massive Dirac fermion experiences a complete suppression of transmission at normal incidence, i.e. $T = 0$ when $\phi = \pi/2$. The same heuristic explanation used for Klein tunneling in monolayer graphene also can be applied here[29]. An incoming electron has pseudospin parallel to its velocity (Equations 1.21 and 1.22). The forward scattering hole, however, has a pseudospin pointing in the antiparallel direction as its velocity while the backscattering electron's pseudospin is in the same direction as the incident electron. Hence, pseudospin conservation during this process would then prohibit the incident electron from forward scattering.

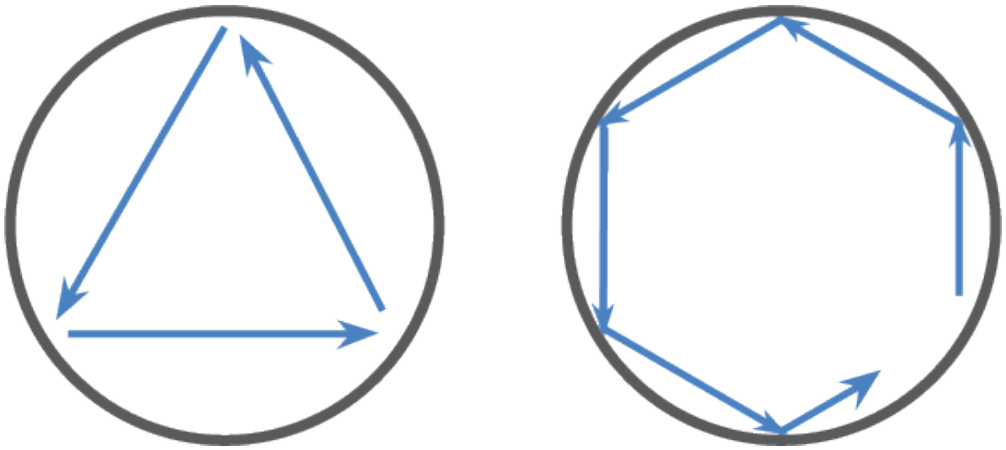

Figure 1.3: Electron paths in a circular p-n junction for a low angular momentum particle (a) and high angular momentum particle (b).

1.3 Circular P-N Junctions in Graphene

The unique anisotropic transmission of Dirac quasiparticles at graphene p-n junctions results in interesting quasi-bound states within circular p-n junctions. In monolayer graphene, Klein tunneling prevents complete charge carrier trapping and formation of bound states. However, the coefficient of reflection at monolayer graphene p-n junctions increases as a function of the angle of incidence. Cheianov *et al.* theoretically modelled electron transmission across a smooth p-n junctions and showed that the transmission probability $T \propto e^{-\sin(\phi)^2}$[27]. Then for electron trajectories like those shown in Fig. 1.3 partial confinement is expected. Indeed, Matulis *et al.* [36] have predicted the existence of quasi-bound quantum dot eigenstates with finite lifetimes in cylindrically symmetry electrostatic step potentials. They predicted that due to Klein tunneling, low angular momentum states (Fig. 1.3a) should be less well confined, and therefore have larger linewidths, than higher angular momentum modes (Fig. 1.3b). For bilayer graphene, however, the opposite trend is expected where higher angular momentum eigenstates are more weakly confined than lower angular momentum electronic states. Furthermore, gate-tunable bandgap and pseudospin chirality in bilayer graphene provide a unique confinement mechanism for charge carriers in bilayer graphene quantum dots [37].

1.4 Scanning Tunneling Microscopy

In order to understand the electronic structure of graphene quantum dots, we use scanning tunneling microscopy (STM) and scanning tunneling spectroscopy (STS). In this section, we discuss how to physically interpret our STM/STS data.

$\mathbf{dI/dV_s}$ Spectrum. Differential conductance of STM tunneling current $\mathrm{d}I/\mathrm{d}V_s$ is pro-

portional to the sample local density of states[38–40]:

$$\frac{dI}{dV_s}(\vec{r}) \propto LDOS(\vec{r}, E_F + eV_s), \tag{1.28}$$

where $\vec{r}$ is the location of the STM tip, E_F is the sample Fermi level and V_s is the sample bias defined as the negative of the STM tip bias voltage. Since V_s can be positive or negative, $\mathrm{d}I/\mathrm{d}V_s$ spectroscopy probes the sample electronic structure for a range of energies above and below the sample's Fermi level.

STM Topography. Our STM topographs are performed in constant-current mode where the tip height is adjusted to maintain a constant tunneling current. A simplified expression for STM tunneling current is given by:

$$I(\vec{r}, V_s) \propto e^{-z/\lambda} \int_0^{V_s} LDOS(\vec{r}, E_F + eV)dV, \tag{1.29}$$

where z is the STM tip height and λ is the effective local decay length. Hence, the STM tunneling current decays exponentially as a function of tip-sample distance, which enables measurements that are highly sensitive to the surface topography. However, since the expression for current in Equation 1.29 also depends on sample local density of states (LDOS), a constant-current STM topograph represents a convolution of surface topography and sample LDOS.

$\mathbf{dI/dV_s}$ Map. Our $\mathrm{d}I/\mathrm{d}V_s$ maps are obtained for a specific value of V_s in constant-current mode. This means that our $\mathrm{d}I/\mathrm{d}V_s$ signal observed in our experimentally measured $\mathrm{d}I/\mathrm{d}V_s$ maps are proportional to the local density of states with a proportionality factor[18]:

$$\frac{dI}{dV_s}(\vec{r}) \propto \frac{LDOS(\vec{r}, E_F + eV_s)}{|\int_0^{V_s}(\vec{r}, E_F + eV)dV|}. \tag{1.30}$$

Hence, intensities in $\mathrm{d}I/\mathrm{d}V_s$ maps reveal spatial variations in the sample electronic structure but are not necessarily directly proportional to LDOS.

Chapter 2

Engineering Embedded Gates

Electrostatic gating is an important method for tuning electronic properties of conducting materials. In particular, local electrostatic gates have been extensively used for quantizing charge carriers in two-dimensional electron gas systems (e.g. GaAs 2DEG's). As discussed in Section 1.3, gate-induced p-n junctions also provide a platform for charge confinement in graphene. Common techniques for fabricating local electrostatic gates involve some combination of lithography and metal deposition. However, these methods often introduce contamination on the sample surface and prevent access to surface probe instruments like STM. In this chapter, we present a procedure for in-situ creation of local embedded gates in graphene/hexagonal boron nitride(hBN) heterostructures using hBN defect charge manipulation. This novel method is versatile, reversible, and does not introduce surface contamination.

In Section 2.2, we describe the use of STM to provide microscopic characterization of charged impurities within hBN. Recently, hexagonal boron nitride (hBN) has surfaced as one of the most important components in van der Waals heterostructures. It is often used as an ultra-flat substrate for various two-dimensional materials and also as an encapsulating layer for protection against contaminants. The reason why hBN is useful for these purposes is that it is an inert, large-gap insulator that introduces much less charge inhomogeneity than SiO_2. Previous studies have shown, however, that hBN is not entirely free from impurities[41]. In this Section, we discuss the detection and characterization of these hBN impurities using STM on graphene/hBN heterostructures. We show that there are both positively and negatively charged defects in hBN at various layer depths from the graphene-hBN interface. Using scanning tunneling spectroscopy, we are able to provide quantitative characterization on defect energy levels.

In Section 2.3, we show that the charge state of hBN impurities can be manipulated via STM. We show that when a voltage pulse is applied to a scanning tunneling microscope tip near the graphene surface, electric-field-induced tunneling allows microscopic control over the charge state of hBN defects. $\mathrm{d}I/\mathrm{d}V_s$ maps before and after STM tip voltage pulses reveal that defect charges can be added, removed, and flipped in polarity.

In Section 2.4, we demonstrate our technique for fabricating local embedded gates in

graphene/hBN heterostructures by local accumulation of hBN defect charges. We accomplish this by exploiting our control over the charge state of hBN defects in conjunction with a backgate electric field. This allows us to engineer local electrostatic gates on graphene of variable polarity, shape, and magnitude. Using scanning tunneling spectroscopy, we confirm that our embedded gates locally dope the overlaid graphene. This technique for local gate fabrication does not introduce additional contamination nor prevent surface probe characterization of graphene, creating many potential applications in the field of van der Waals heterostructures.

Sections 2.1, 2.2, and 2.3 are adapted from the following published paper with permission from co-authors: D. Wong *et al.*, "Characterization and manipulation of individual defects in insulating hexagonal boron nitride using scanning tunneling microscopy," *Nature Nanotech.* **10**, 949953 (2015). Copyright 2015 Macmillan Publishers Limited.

2.1 Introduction

Hexagonal boron nitride (hBN) is an essential component in many new and technologically promising devices that incorporate two-dimensional materials[42–44] and so it is crucial to understand the nature of intrinsic defects in hBN layers. Previous cathodoluminescence and elemental analysis of high-purity single-crystal hBN synthesized at high pressure and temperature indicated the existence of residual impurities and defects[41, 44]. Optoelectronic experiments have revealed that these defects give rise to photoactive states within the hBN bandgap[45, 46]. So far, however, these studies have been limited to spatially averaged defect behavior, and the investigation of individual defects at the nanoscale remains an outstanding challenge. In this chapter, we provide microscopic characterization and manipulation of individual hBN defects using STM.

2.2 Defects in Hexagonal Boron Nitride

Figure 2.1 represents our experimental setup where a graphene/hBN heterostructure is placed on SiO_2/silicon wafer (the silicon is heavily doped in order to act as a backgate). The graphene is grounded with a gold contact and its surface is accessible to an STM tip with a bias voltage $-V_s$. Here we follow the convention where V_s, the sample bias, is defined as the negative of the STM tip voltage. A backgate voltage V_g is applied to the heavily doped silicon and can be used to tune the Fermi level of the entire graphene flake.

Figure 2.2(a) is a typical scanning tunneling microscopy (STM) topographic image of our graphene/hBN heterostructures, where a 7 nm moiré pattern can be seen on top of long-range height fluctuations spanning tens of nanometers, similar to previous imaging of graphene on BN[47, 48]. Localized shallow dips and a protrusion are also visible ($\Delta z < 0.1$Å). More revealing, however, are the differential conductance ($\mathrm{d}I/\mathrm{d}V_s$) maps shown in Fig. 2.2(b). Striking new features are visible in these data. We observe randomly distributed

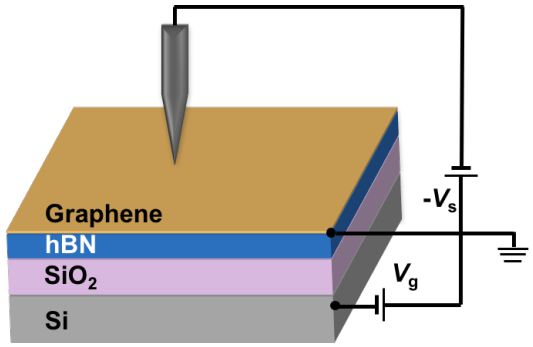

Figure 2.1: Schematic diagram of scanning tunneling microscopy on a backgate graphene/hBN heterostructure.

bright (high $\mathrm{d}I/\mathrm{d}V_s$) and dark (low $\mathrm{d}I/\mathrm{d}V_s$) circular dots (∼20 nm in diameter) that have varying degrees of intensity. Another common feature, as seen at the right edge of the map in Fig. 2.2(b), is a sharp ring structure with an interior that does not obscure the moiré pattern. Close-up topographic studies of these defects reveal unblemished atomically resolved graphene honeycomb structure with occasional slight dips or a protrusion with $|\Delta z| < 0.1$Å. Maps obtained at numerous locations with many tips across different devices replicate these observations.

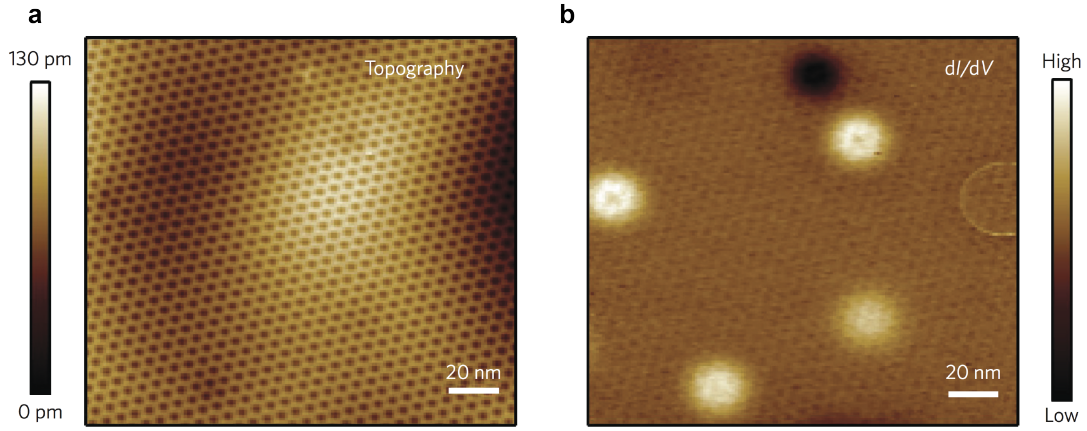

Figure 2.2: STM topography and corresponding $\mathrm{d}I/\mathrm{d}V_s$ map for a graphene/hBN device. (a) STM topographic image of a clean graphene/hBN area. (b) A $\mathrm{d}I/\mathrm{d}V_s$ map ($I = 0.4nA$, $V_s = 0.25V$) acquired simultaneously with a exhibits various new features: bright dots, a dark dot and a ring.

Figure 2.3a,b presents higher-resolution $\mathrm{d}I/\mathrm{d}V_s$ maps of representative bright and dark dot defects. These maps show clearly that the graphene moiré pattern is not obscured by the defects. To determine the effect of these defects on the electronic structure of graphene, we performed $\mathrm{d}I/\mathrm{d}V_s$ spectroscopy at varying distances from the dot centers (each spectrum

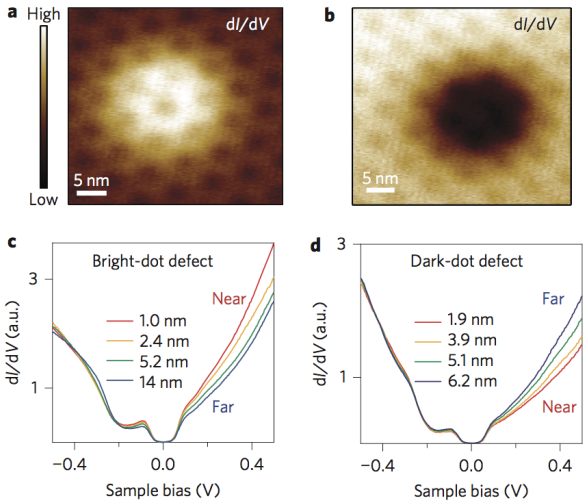

Figure 2.3: dI/dV_s maps and spatially dependent dI/dV_sspectroscopy determining the defect charge state. (a,b) dI/dV_s maps (I = 0.4 nA, $V_s = 0.3$ V, $V_g = 5$ V) for bright- and dark-dot defects. (c) dI/dV_s spectroscopy (initial tunneling parameters: I = 0.4 nA, $V_s = 0.5$ V, $V_g = 20$ V) measured on graphene at different lateral distances from the center of the bright dot in (a). (d), Same as in (c), but for the dark dot in (b). Distance-dependent dI/dV_s spectroscopy reveals that (a) and (b) represent positively and negatively charged defects in hBN, respectively.

was started with the same tunnel current I and sample bias V_s). These data are plotted in Fig. 2.3c,d for the bright and dark dots, respectively. The spectra are characteristic of undamaged graphene[49], but show an electron/hole asymmetry that is dependent on the tip position relative to the center of a defect. In Fig. 2.3 c, for example, we see that dI/dV_s ($V_s > 0$) increases as the tip approaches the bright-dot center. Figure 2.3d shows the opposite trend, as seen by the decrease in dI/dV_s ($V_s > 0$) as the STM tip approaches the dark-dot center. These basic trends were seen for all bright and dark dot defects, regardless of the intensity and tipheight configuration (Supplementary Section 4 of Ref [50]). These observations can be understood by recalling that dI/dV_s reflects the graphene local density of states (LDOS). The distance-dependent enhancement of dI/dV_s above the Dirac point ($V_s \approx -0.17$ V) as the tip nears a bright dot in Fig. 2.3c can therefore be interpreted as arising from the attraction of negatively charged Dirac fermions to the dot center. We thus conclude that the bright dot in Fig. 2.3a reflects a positively charged defect in BN [14, 51]. Similarly, the dis- tance-dependent reduction of dI/dV_s above the Dirac point in Fig. 2.3d arises from the repulsion of negatively charged Dirac fer- mions from the defect. We thus conclude that the dark dots are negatively charge[14, 51].

We now focus on the ring defects, as displayed at the right edge of Fig. 2.2b. We find that the ring radius depends on the values of V_s and backgate voltage V_g. Figure2.4 shows that the ring radius changes from 2 nm (Fig. 2.4a) to 11 nm (Fig. 2.4b) as V_g is changed from

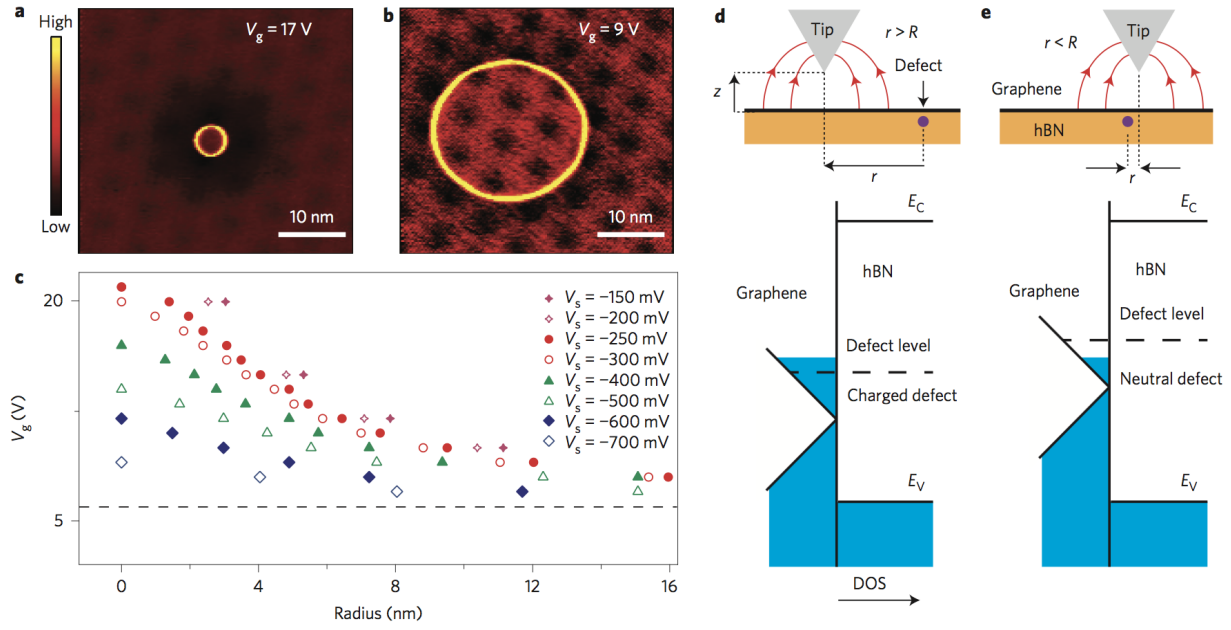

Figure 2.4: $\mathrm{d}I/\mathrm{d}V_s$ maps of ring defect enable energy-level characterization. (a,b) $\mathrm{d}I/\mathrm{d}V_s$ maps (I = 0.4 nA, V_s = 0.3 V) of the same ring defect at backgate voltages of V_g = 17 V and 9 V, respectively. (c) Ring radius R for different V_s and V_g. The ring radius was extracted from $\mathrm{d}I/\mathrm{d}V_s$ maps taken at the same location as in (a) and (b). (d,e) Schematic model (energies not to scale) for ring formation due to charge transfer between graphene and a defect in the top layer of hBN. When the distance r between the tip and the defect is larger than the ring radius R (d), the defect level is filled and negatively charged. When $r < R$ (e), local gating from the tip lowers the local electron density so that the Fermi level is below the defect level, neutralizing the defect. For negative tip potentials and n-doped graphene, R increases as reduced V_g shifts the unperturbed defect level closer to the Fermi energy.

V_g = 17 V to 9 V (with constant V_s = 0.3 V). Figure 2.4c shows the dependence of the ring radius on V_g for various V_s values (denoted by distinct symbols). These data were obtained by measuring the ring radius from $\mathrm{d}I/\mathrm{d}V_s$ maps taken at the same location as Fig. 2.4a,b, but with different V_s and V_g configurations. Although the precise ring radius depends on the sharpness of the STM tip[52], the qualitative behavior shown in Fig. 2.4c is typical of the vast majority of ring defects observed here. In general, for fixed V_s , the ring radius increases with decreasing V_g until a critical backgate voltage ($V_c = 6 \pm 1$V) is reached, whereupon the ring vanishes.

We now discuss the origin of the dot and ring defects observed in our $\mathrm{d}I/\mathrm{d}V_s$ maps. Three general scenarios are possible: (1) adsorbates bound to the surface of graphene; (2) adsorbates trapped at the interface between the graphene and hBN; and (3) intrinsic defects within the insulating hBN substrate. Our data imply that (3) is the correct scenario, for

the following reasons. First we rule out scenario (1) because weakly bound adsorbates would have a higher height profile than the topographically small features observed[51, 53] (Supplementary Section 3 of Ref [50]) and would also probably get swept away by the STM tip when it is brought close enough to observe the graphene honeycomb structure[14]. Strongly bound adsorbates in scenario (1) would also probably have taller height profiles as seen for other graphene adsorbates (Supplementary Section 3 of Ref [50]) and should disrupt the graphene honeycomb lattice[54] (which was not observed). Also, strongly bound adsorbates should lead to changes in the graphene spectroscopy due to the formation of localized bonding states[54], which are not seen. Scenario (2) can be ruled out because an adsorbate trapped beneath graphene would cause a bump in graphene at least an order of magnitude larger than the $|\Delta z| < 0.1$Å feature observed here. We would also expect a trapped adsorbate to locally delaminate the graphene from the hBN substrate, thus disrupting the moiré pattern, which is not seen.

Scenario (3) — intrinsic charged hBN defects — is thus the most likely explanation for the defects observed here. Polycrystalline hBN has been shown to host several varieties of charged defects, as seen from electron paramagnetic resonance [55] and luminescence experiments[56, 57], as well as theoretical investigations[58]. In those studies the most abundantly reported defects were nitrogen vacancies, which were shown to act as donors, and carbon impur- ities substituted at nitrogen sites, which were shown to act as acceptors. Secondary ion mass spectroscopy studies of high-purity single-crystal BN synthesized at high pressure and temperature have also identified oxygen and carbon impurities[41]. A comparison between optoelectronic experiments[45, 46] on new, high-purity single- crystal hBN and recent theoretical work[59] shows that the nature of the defects in the new, high-purity hBN crystals is consistent with observations of carbon impurities and nitrogen vacancies in previous polycrystalline studies (although the influence of oxygen impurities remains ambiguous). Such defects, when ionized, could induce the bright and dark dots observed in graphene/BN via a graphene screening response[60] (Figs 2.2 and 2.3). The fact that these defects are embedded in the hBN explains why the dots have such a small topographic deflection, as well as why the graphene lattice and moiré pattern are not disrupted, and also why no new states arise in the graphene spectroscopy[53, 54]. Variations in the intensity of bright and dark defects are explained by hBN defects lying at different depths relative to the top graphene layer.

It is possible to extract quantitative information regarding the electronic configuration of hBN defects from the STM $\mathrm{d}I/\mathrm{d}V_s$ signal measured from the graphene capping layer. This can be achieved for the ring defects by analysing the gate (V_g) and bias (V_s) dependent ring radius, shown in Fig. 2.4c. Similar rings have been observed in other systems and have been attributed to the charging of an adsorbate or defect [52, 53, 61, 62]. Because the ring in Fig. 2.4 is highly responsive to the presence of the STM tip and displays no charge hysteresis, we expect that it lies in the topmost hBN layer and is strongly coupled to the graphene electronic structure. The STM tip is capacitively coupled to the graphene directly above the defect through the equation $|e|\delta n = C(r)V_{tip}$, where δn is the local change in graphene electron density, $C(r)$ is a capacitance (per area) that increases with decreasing lateral tipdefect distance r, V_{tip} is the tip electrostatic potential ($V_{tip} = V_s + constant$, see

Supplementary Section 6 of Ref [50]), and $|e|$ is the charge of an electron. For the $\mathrm{d}I/\mathrm{d}V_s$ maps in Fig. 2.4, $V_{tip} < 0$, so the electrostatic gating from the tip lowers the electron density of the (n-doped) graphene directly beneath the tip. Figure 2.4d schematically depicts the local electronic structure of the graphene immediately above the defect when r is large and V_g is set such that the defect level is filled and carries negative charge. As the tip approaches the defect, $C(r)$ increases and thus δn becomes more negative. Eventually, the defect level crosses the Fermi level (and switches to a neutral state) when the tip is at a distance R away from the defect, thus causing a perturbation in the tunnel current that leads to the observation of a ring of radius R. Figure 2.4e shows the case ($r < R$) where the defect is in a neutral charge state through interaction with the tip. The energy level of the defect can be found by tuning V_g such that the Fermi level matches the defect level in the absence of the tip. This will cause the radius of the charging ring to diverge. As seen in Fig. 2.4c, this occurs for the observed ring defects when $V_g = 6 \pm 1$V, thus resulting in a defect level 30 ± 10 meV above the graphene Dirac point energy (because the Dirac point energy can be measured with respect to the Fermi level), which is expected to be 4 eV below the hBN conduction band-edge[63]. Interestingly, this is similar to a previously observed carbon substitution defect level [56], suggesting that the ring defect arises from a carbon impurity.

2.3 Scanning Tunneling Microscope Manipulation of Defect Charge in Hexagonal Boron Nitride

Figure 2.5(a) presents a $\mathrm{d}I/\mathrm{d}V_s$ map exhibiting numerous charged defects. To manipulate the charge state of the observed hBN defects, the STM tip was positioned 1 nm over the center point of this area and a bias of $V_s = 5$ V was applied for 10 s. After applying this voltage pulse, a $\mathrm{d}I/\mathrm{d}V_s$ map was acquired over the same region at low bias, as shown in Fig. 2.5(b). Figure 2.5(c) shows the same region after similar application of a second pulse. Inspection of Fig 2.5(b,c) shows that the hBN defect configurations are significantly altered by application of such voltage pulses. The defects are seen to reversibly switch between charged and neutral states, as well as between states having opposite charge. To highlight this behavior, we denote changes to defect states (compared to the preceding image) with colored arrows. A red arrow signifies the disappearance of a charged defect, a blue arrow represents the appearance of a charged defect, and a green arrow indicates where a defect has changed the sign of its charge. We find that defects that disappear after a tip pulse always reappear in the same location after subsequent tip pulses. Additionally, dark dots tend to switch into metastable neutral states (that is, disappear) at a higher rate than bright dots. Ring defects, as well as the darkest and brightest dots, remain unchanged by tip pulses. Similar manipulation has been performed previously to switch the charge state of defects in semiconductors[64] as well as adatoms on top of ultrathin insulating films[65].

This tip-induced manipulation of hBN defects can be explained by electric-field-induced emission of charge carriers from hBN defect states. By tilting the local potential landscape,

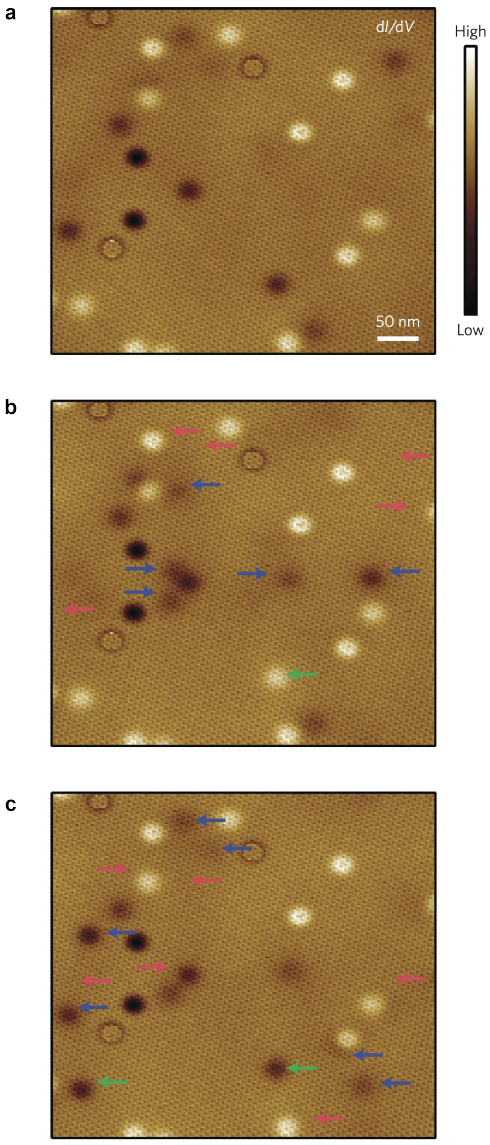

Figure 2.5: Manipulating defects in hBN with an STM tip. Tip pulses with V_s= 5 V and Δt= 10 s are used to toggle the charge states of the dot defects. (a) $\mathrm{d}I/\mathrm{d}V_s$ map (I = 0.4 nA, V_s = 0.25 V) of graphene/hBN reveals various dots and rings. (b) $\mathrm{d}I/\mathrm{d}V_s$ map of the same region after a tip pulse is applied at the center of the region in a. (c) $\mathrm{d}I/\mathrm{d}V_s$ map of the same region after another tip pulse. Red arrows mark the disappearance of dots relative to the previous image, blue arrows mark the appearance of dots, and green arrows mark dot defects that have changed the sign of their charge.

the STM tip causes charge carriers to tunnel through the ionization barrier between different defects, charging some while neutralizing others. This accounts for the disappearance and reappearance of the dots in the same location, which cannot be described by defect migration through the hBN lattice. In addition, the observation of a higher rate of switching for the dark dots (acceptors) than bright dots (donors) suggests it is more energetically favorable for neutral acceptors to emit holes than for neutral donors to emit electrons (and the same for the reverse processes). Hence, the acceptor states are probably closer to the valence band than the donor states are to the conduction band. Because the rings, as well as the darkest and brightest dots, never change under tip pulses, we surmise that they are in the top layers of hBN and in direct electrical contact with the graphene. Their charge states thus depend only on graphene's local chemical potential and show no hysteresis or metastability with

the electric field (for example, the ring defects smoothly and reversibly alter their charge in response to the passage of the STM tip and always return to the same charge state). The defects that switch into new metastable charge states (that is, exhibit hysteresis) must thus be in lower hBN layers, out of direct contact with the graphene.

2.4 Local Electrostatic Gates in Graphene/hBN Heterostructures

This section was adapted from the following published paper with permission from co-authors: J. Velasco Jr. *et al.* "Nanoscale Control of Rewriteable Doping Patterns in Pristine Graphene/Boron Nitride Heterostructures," *Nano Lett.* **16**, 16201625 (2016). Copyright 2016 American Chemical Society.

Having established that individual defects in hBN can be ionized by STM tip voltage pulses, we now employ the gate electric field to produce net charge exchange between graphene and the insulating substrate. We applied tip voltage pulses to a graphene/hBN device using the experimental setup sketched in Figure 3.1(a). Figure 2.6(a) shows $\mathrm{d}I/\mathrm{d}V_s$ spectra obtained with $\tilde{V}_g = 0$ V after applying $V_s = 5$ V tip voltage pulses while holding V_g at different values (the $\mathrm{d}I/\mathrm{d}V_s$ spectra were obtained at the same location the tip pulses were applied). The red trace shows the reference spectrum measured before application of any tip pulses. Here we observe an ~ 130 mV gaplike feature at the Fermi energy[48, 49] that is known to arise due to phonon-mediated inelastic tunneling[49]. To the right of this inelastic tunneling feature is a dip (black arrow) that marks the DP. Because the DP lies to the right of the Fermi energy ($V_s = 0$ V), we see that this region of the surface has residual p-doping ($\sim 5 \times 10^{11} cm^2$) at zero gate voltage. The yellow, green, and blue traces show the $\mathrm{d}I/\mathrm{d}V_s$ spectra measured after applying tip pulses lasting 30s with the gate voltage set respectively to $\tilde{V}_g = 10, 20$, and 30 V (the height of the tip in each case was approximately 1.5 nm away from the surface). As shown by the black arrows, the DP shifts down in energy as each tip pulse is delivered with a more negative gate voltage. The sample is seen to locally change from p-type doping to n-type doping after the first pulse and then to become more heavily n-doped after each pulse. This behavior is consistent with the local hBN charge landscape becoming increasingly positively charged after tip pulses performed at increasingly negative gate voltages. Reversing the polarity of the gate field, while leaving everything else the same, results in local graphene doping with the exact opposite polarity[66].

We were able to gain insight into the spatially varying dopant landscape that results from a tip pulse by performing $\mathrm{d}I/\mathrm{d}V_s$ imaging of the area beneath the STM tip both before and after a tip pulse. All maps exhibited a 7 nm moiré pattern, indicating a clean graphene/hBN interface. Figure 2.6(b) shows a $\mathrm{d}I/\mathrm{d}V_s$ map of a patch of graphene right before performing a tip pulse. It contains a number of point-like defects due to charge centers in the hBN layer[50] but otherwise exhibits a smooth charge landscape. We next brought the STM tip to the top right corner of this region and applied a tip voltage pulse while holding the gate

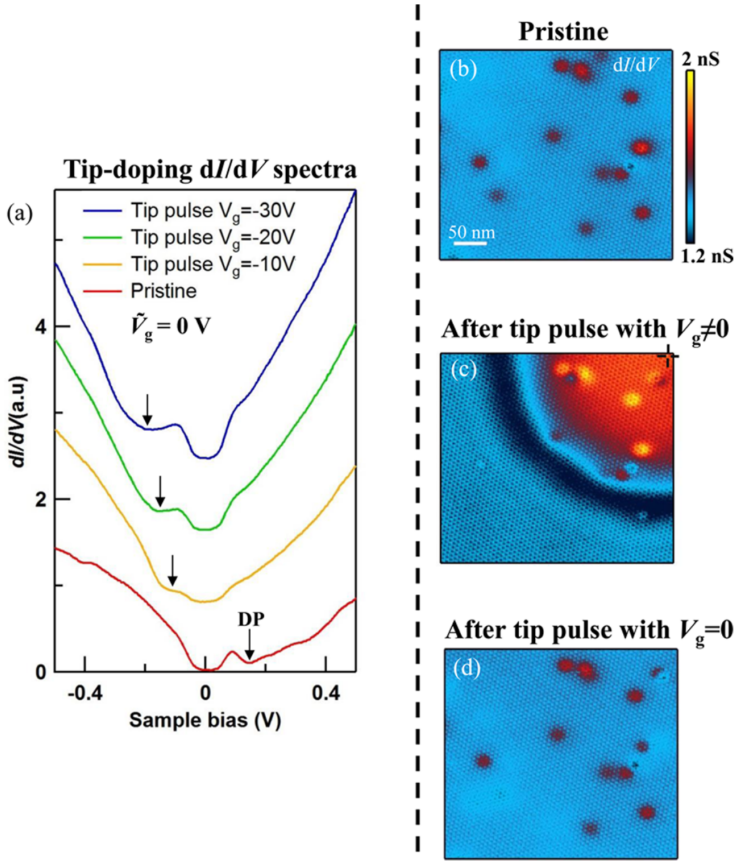

Figure 2.6: Nanoscale doping patterns in graphene controlled with an STM tip voltage pulse. (a) The $\mathrm{d}I/\mathrm{d}V_s$ spectroscopy of a pristine surface before a tip pulse (red) and after a tip pulse (V_s =5V,30s) for V_g =10V (yellow), 20 V (green), and 30 V (blue). Initial tunneling parameters: $I = 0.4$ nA, $V_s = 0.5$ V, V $\tilde{V}_g = 0$. The curves are vertically offset for clarity. (b) $\mathrm{d}I/\mathrm{d}V_s$ map of pristine graphene/hBN ($I = 0.4$ nA, $V_s = 0.25$ V, $\tilde{V}_g = 5$ V). (c) The $\mathrm{d}I/\mathrm{d}V_s$ map of the same region after a tip pulse was applied in the corner of the map (location denoted by cross hair), while holding $V_g = 20$ V ($I = 0.4$ nA, $V_s = 0.25$ V, $\tilde{V}_g = 10$ V). (d) The $\mathrm{d}I/\mathrm{d}V_s$ map of the same region after another tip pulse was applied in the same location, while holding $V_g = 0$ V ($I = 0.4$ nA, $V_s = 0.25$ V, $\tilde{V}_g = 5$ V). All data were acquired from a device with a 44 μm width and 39 μm source-drain separation.

voltage at $V_g = 20$ V. Figure 2.6(c) shows a $\mathrm{d}I/\mathrm{d}V_s$ map of the same region after applying the tip pulse. The most striking feature in the $\mathrm{d}I/\mathrm{d}V_s$ map after the tip pulse is the emergence of a red disk region in the upper right quadrant of the map, which also exhibits a darkened halo around the perimeter. Although only one quadrant is shown, the new red region exhibits rough circular symmetry. The altered charge landscape is stable at $T = 5$ K long after the pulse has been applied, but it can be erased by application of an identical tip pulse with the gate voltage held at $\tilde{V}_g = 0$V. Figure 2.6(d) shows a $\mathrm{d}I/\mathrm{d}V_s$ image of the same graphene

patch after application of such an "eraser" pulse. The altered red disk is now completely gone and the graphene is returned to its pristine state.

The new charge-doping landscape induced by the tip pulse can be explained by a combination of field-induced defect ionization and charge diffusion within the hBN insulator. The strong electric field of the tip pulse penetrates through the gated graphene into the insulator region, causing a strong potential gradient around hBN defects and resulting in enhanced defect field emission. When the gate is on during a tip pulse, the gate electric field causes released electrons to drift either into the graphene electrode ($V_g < 0$, resulting in a positive space charge layer in the hBN) or away from the graphene electrode ($V_g > 0$, resulting in a negative space charge layer in the hBN). Pulses applied with $V_g = 0$V allow charge to freely diffuse and recover the initial state of graphene. The net result is that both p-type and n-type doping profiles can be written and erased in pristine graphene/hBN with a spatial resolution determined by the potential gradient surrounding an STM tip. For example, the red region in Figure 2.6(c) is n-doped graphene while the blue region surrounding it is p-doped graphene, and the boundary between these two regions defines a rewritable nanoscale p-n junction.

Chapter 3

Monolayer Graphene Quantum Dots

In this chapter, we provide experimental and theoretical investigation of monolayer graphene quantum dots defined by circular p-n junctions. Using scanning tunneling microscopy, we fabricate gate-tunable quantum dots in graphene/hBN heterostructure and characterize their electronic structures. Theoretical calculations of massless Dirac fermions in circular p-n junctions are presented to support our experimental findings.

In Section 3.2, we use the technique for creating local embedded gates described in Section 2.4 to create gate-tunable circular p-n junctions in monolayer graphene. We then provide spectroscopic evidence that these circular p-n junctions confine graphene charge carriers to form discrete quantum dot energy levels. Spatially resolved scanning tunneling spectroscopy reveals quasi-bound eigenstates within circular p-n junctions and Friedel-like interference patterns outside. We then compare our experimental observations with theoretical simulations of the massless Dirac Hamiltonian in two-dimensional harmonic oscillator potential, which allows us to identify and associate each observed peak in our experimental data with a unique set of radial and angular quantum numbers. Finally, we create a circular p-n junction of opposite polarity to show that by changing the polarity of the local gate, we can create electron graphene quantum dots as well as hole quantum dots.

In Section 3.3, we explore the origin of the confinement potential in our graphene quantum dots. In our theoretical simulation of the massless Dirac equation presented in Section 3.2, we approximate the confinement potential as a quadratic function. We explain how the potential strength was extracted from experimental data and show that a harmonic oscillator potential is a reasonable approximation for our experiment. Furthermore, we solve a simplified Poisson equation to show that the experimentally observed local potential can be plausibly attributed to the collective effect of many charged hBN defects.

In Section 3.4, we discuss the competing effect of the STM tip acting as a floating top gate with the local embedded bottom gate within hBN. We show that the effect of the STM tip work function can be made negligible by tuning the strength of the embedded bottom gate potential.

Content from the following paper has been included in this chapter with permission from co-authors: Lee, J. *et al.* Imaging electrostatically confined Dirac fermions in graphene

quantum dots. *Nature Physics* **12**, 10321036 (2016).

3.1 Introduction

Quantum confinement of charge carriers in conducting materials is important for the control and application of orbital and spin properties of electrons. Since the discovery of graphene, many different methods have been used to localize graphene's charge carriers, including lithographic techniques for mechanically carving graphene[4–7], chemical deposition of graphene islands[8–10], utilization of band-bending in graphene edges[11], unfolding C_{60} molecules [12], magnetic fields with charge inhonogeneity[13], and deposition and accumulation of adatoms on pristine graphene[14]. Yet another method for electron confinement in graphene is by using local electrostatic gating to induce circular p-n junctions in graphene, as discussed in Section 1.3. A recent tunnelling spectroscopy experiment[17] revealed signatures of electron confinement induced by the electrostatic potential created by a charged STM tip. However, since the confining potential moves with the STM tip, this method allows neither spatial imaging of the resulting confined modes nor patterning control of the confinement potential. Another recent experiment[19] showed spectroscopic signatures of electrostatic charge confinement in graphene grown on copper. However, this method also does not provide flexible control of quantum dot geometry. In this chapter, we employ the technique described in Chapter 2 to create local embedded gates that allows us to fabricate stationary graphene quantum dots and spatially map their electronic structures.

3.2 Electronic Structure of a Circular Graphene P-N Junction

Here we employ the previously described patterning technique that allows the creation of stationary circular p–n junctions in a graphene layer on top of hexagonal boron nitride. Figure 3.1(a) illustrates how stationary circular graphene pn junctions are created. We start with a graphene/hBN heterostructure resting on a SiO_2/Si substrate. The doped Si substrate acts as a global backgate while the hBN layer provides a tunable local embedded gate after being treated by a voltage pulse from an STM tip[66]. To create this embedded gate the STM tip is first retracted approximately 2 nm above the graphene surface and a voltage pulse of V_s = 5 V is then applied to the STM tip while simultaneously holding the backgate voltage to $\tilde{V}_g$ = 40 V. The voltage pulse ionizes defects in the hBN region directly underneath the tip [50] and the released charge migrates through the hBN to the graphene[66]. This leads to a local space-charge build-up in the hBN that effectively screens the backgate and functions as a negatively charged local embedded gate[66] (using the opposite polarity gate voltage during this process leads to an opposite polarity space charge). Adjusting V_g afterwards allows us to tune the overall doping level so that the graphene is n-doped globally, but p-doped

inside a circle centered below the location where the tip pulse occurred (it is also possible to control the charge carrier density profile as well as create opposite polarity p-n junctions by changing the V_g applied during the tip pulse). As shown schematically in Figure 3.1(b), the STM tip can then be moved to different locations to probe the electronic structure of the resulting stationary circular p–n junction.

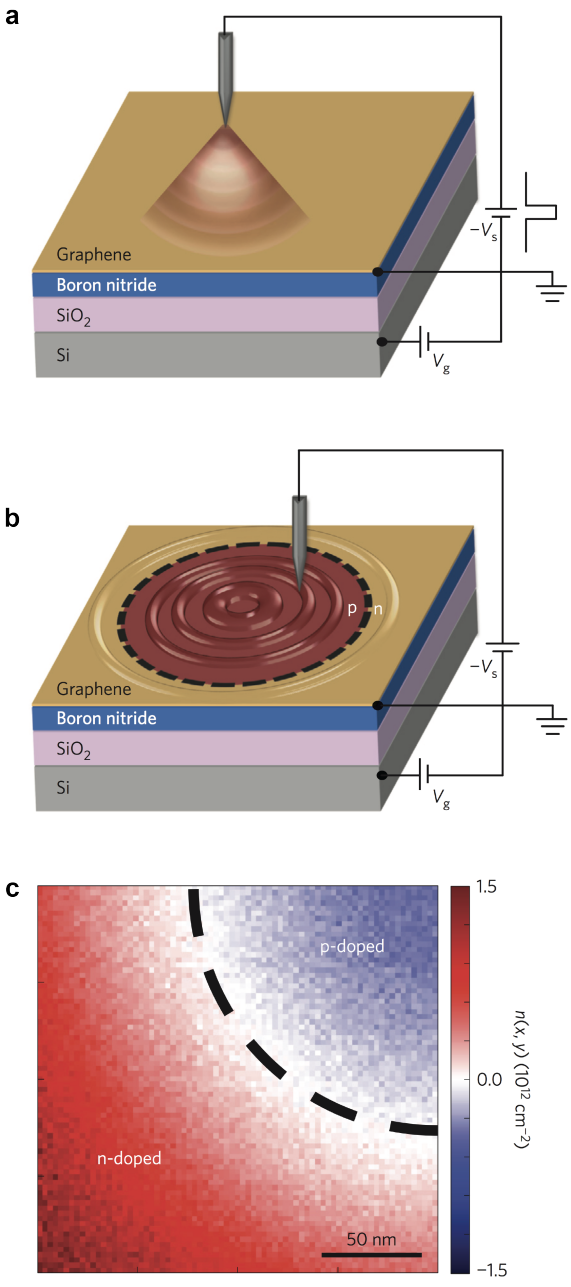

Figure 3.1: Creating and imaging a circular graphene p-n junction. (a) Schematic diagram showing the fabrication of a local embedded gate in a graphene/hBN heterostructure. A square voltage pulse is applied to the STM tip (held a few nanometers from the graphene surface) while the back-gate voltage V_g is fixed at a nonzero value. V_s is defined as the negative of the tip bias. This technique creates a circular p-n junction in the graphene in response to trapped space charge in the insulating hBN. (b) The STM tip spatially probes Dirac fermion wavefunctions in the presence of the p-n junction. (c) A representative experimental charge density map for one quadrant of a circular graphene p-n junction. A $\mathrm{d}I/\mathrm{d}V_s$ spectrum is measured at each pixel to determine the Dirac point energy $E_D(x, y)$, which is then converted to a local charge carrier density $n(x, y)$. The black dashed line marks the approximate location of the p-n junction boundary at V_g=40V.

To confirm that this procedure results in a circular p-n junction, we measured STM differential conductance ($\mathrm{d}I/\mathrm{d}V_s$)as a function of sample bias (V_s) on a grid of points

covering the graphene area near a tip pulse. The Dirac point energy, E_D, was identified at every pixel, allowing us to map the charge carrier density, n, through the relation $n(x,y) = (sgn(E_D){E_D}^2)/(\pi(\hbar v_F)^2)$, where $v_F = 1.1{\times}10^6$ m/s is the graphene Fermi velocity and $\hbar$ is the reduced Planck constant. Figure 3.1(c) shows the resulting $n(x,y)$ for a tip pulse centered in the top right corner (the carrier density n can be adjusted by changing V_g). The interior blue region exhibits positive charge density (p-type) whereas the red region outside has negative charge density (n-type).

To spatially map the local electronic properties of such circular p–n junctions, we examined a rectangular sector near a p–n junction, as indicated in Figure 3.2(a). Figure 3.2(b) shows a topographic image of the clean graphene surface in this region. A 2.8 nm moiré pattern (corresponding to a 5° rotation angle between graphene and hBN) is visible[47, 48] and the region is seen to be free of adsorbates. A $\mathrm{d}I/\mathrm{d}V_s$ map of the same region (Fig. 3.2(c)) reflects changes in the local density of states (LDOS) caused by the spatially varying charge density distribution. Since the p–n junction center is stationary, we are able to move the STM tip to different locations inside and outside the p–n junction to spatially resolve the resulting electronic states. Figure 3.2(dg) shows $\mathrm{d}^2I/\mathrm{d}V_s^2(V_g, V_s)$ plots at four different locations, as denoted in Fig. 3.2(c). We plot the derivative of $\mathrm{d}I/\mathrm{d}V_s$ with respect to V_s to accentuate the most salient features, which are quasi-periodic resonances that disperse to lower energies with increasing V_g. The energies of the observed resonances are seen to evolve as $\epsilon \propto \sqrt{|V_g - V_{CNP}|}$+constant, where V_{CNP} is the local charge neutrality point, as expected for the relativistic band structure of graphene. We see that the energy spacing between observed resonances ($\Delta\epsilon$) decreases as we move away from the p–n junction center until the resonances disappear outside. For example, $\Delta\epsilon$ is 29 ± 2mV at the center, 16 ± 2mV at 50 nm from the center, and 13±2mV at 100 nm from the center (for V_g =32V). A similar trend is also observed for p–n junctions that are n-doped in the center and p-doped outside.

We have imaged these electronic states both inside and outside of circular p–n junctions. The $\mathrm{d}I/\mathrm{d}V_s$ maps in Fig. 3.3(a,b) show eigenstate distributions mapped at two different energies within the same section of a circular p–n junction (similar to the boxed region of Figure 3.2(a), but with opposite heterojunction polarity). Circular quantum interference patterns resulting from confined Dirac fermions are clearly observed within the junction boundary, as well as scattering states exterior to the boundary. The junction boundary is demarcated by a dark band (low $\mathrm{d}I/\mathrm{d}V_s$) in the middle of each $\mathrm{d}I/\mathrm{d}V_s$ map (and further marked by a dashed line). Comparing the overall spatial locations of the nodes and anti-nodes, the two eigenstate distributions in Fig. 3.3(a,b) are clearly different (for example, one has a node at the origin, whereas the other exhibits a central anti-node). Fig. 3.4(a) shows a more complete mapping of the energy-dependent eigenstates (within a p–n junction of the same polarity as Fig. 3.2(a)) along a line extending from the center (left edge) to a point outside of the p–n junction (right edge) at a gate voltage of V_g = 32 V. The data are plotted as $\mathrm{d}^2I/\mathrm{d}V_s^2(r, V_s)$ (where r is the radial distance from the center) to accentuate the striking oscillatory features. The energy level structure and interior nodal patterns are clearly evident.

Our observations can be explained by considering the behavior of massless Dirac fermions

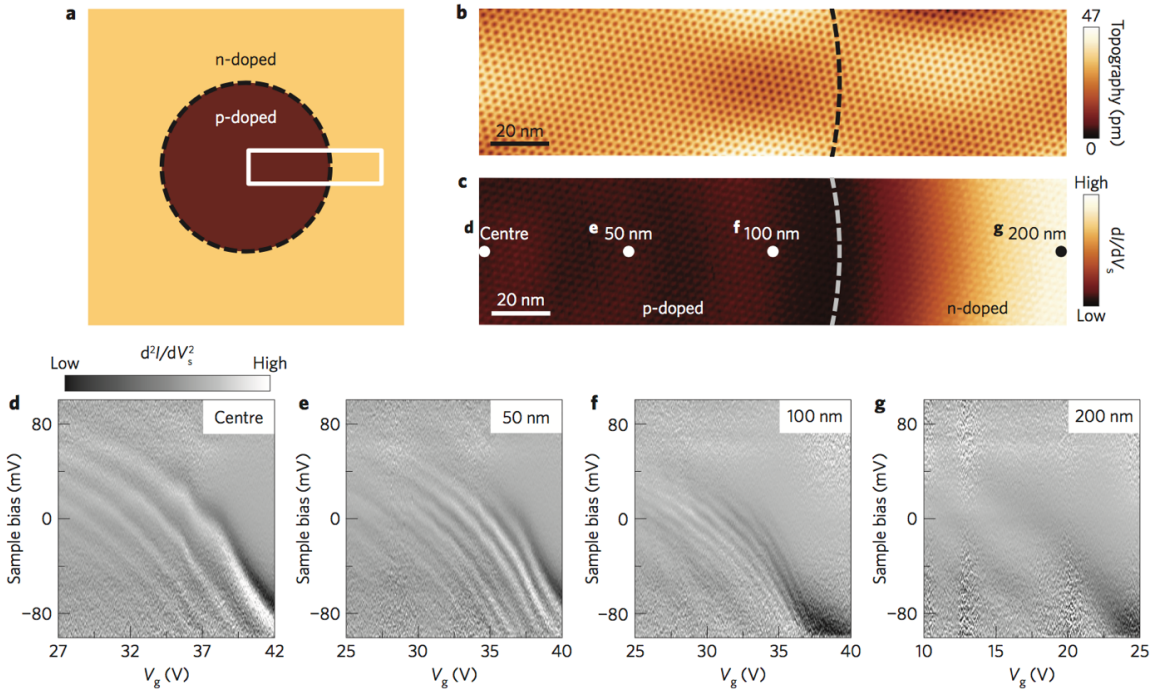

Figure 3.2: Gate-tunable electronic structure of a circular graphene p-n junction. (a) Schematic diagram of a circular p-n junction formed in graphene. The white rectangle indicates the measurement region. (b) STM topographic image of the region sketched in (a). (c) $\mathrm{d}I/\mathrm{d}V_s$ map of the same region as shown in (b). Dashed lines are placed near the p-n junction boundary in (b) and (c) to serve as guides to the eye. (V_s= 0.25 V, I = 0.5 nA, V_g = 30 V, $V_{a.c.}$=6 mV root-mean squared a.c. modulation added to V_s.) (dg) $\mathrm{d}^2I/\mathrm{d}V_s^2(V_g, V_s)$ plots measured at different distances from the center, as indicated in (c) (initial tunneling parameters: V_s= 0.1 V, I = 1.5 nA, 1 mV a.c. modulation). The grey scale bar in (d) also applies to (eg). The observed resonances vary in energy roughly according to the expected graphene dispersion $\varepsilon \propto \sqrt{|V_g - V_{CNP}|}$. The energy spacing between resonances is larger at the center(d) than is seen further out (e,f), and the resonances disappear altogether beyond the p-n junction boundary (g).

in response to a circular electrostatic potential. Due to Klein tunneling, a graphene p–n junction perfectly transmits quasiparticles at normal incidence to the boundary, but reflects them at larger angles of incidence[3, 27, 28]. In a potential well with circular symmetry, electrons with high angular momenta are obliquely incident on the barrier and are internally reflected, thus leading to particle confinement and the formation of quasi-bound quantum dot states[17, 36, 67–70]. As angular momentum is increased, electrons are repelled from the center of the potential by the centrifugal barrier, leading to an increase in the number of $\mathrm{d}I/\mathrm{d}V_s$ resonances that should be observable in spectroscopy measured away from the

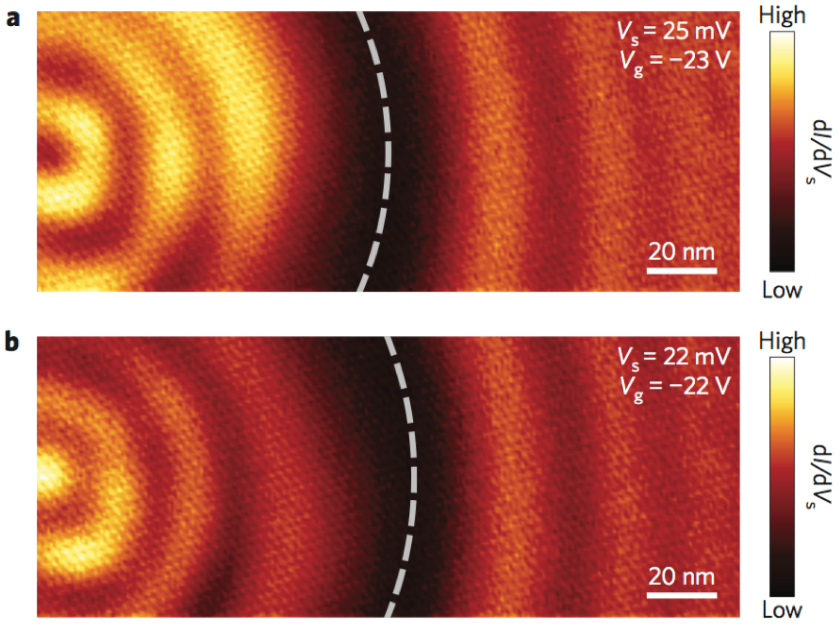

Figure 3.3: $\mathrm{d}I/\mathrm{d}V_s$ images of quantum interference throughout a circular graphene p-n junction. (a) $\mathrm{d}I/\mathrm{d}V_s$ map measured for a p-n junction sector similar to 3.1, but having opposite heterojunction polarity ($V_s = 25$ mV, $I = 0.5$ nA, $V_g = 23$ V, 1 mV a.c. modulation). (b) $\mathrm{d}I/\mathrm{d}V_s$ map at the same location as (a), but for a different energy, shows a different spatial pattern ($V_s = 22$ mV, $I = 0.4$ nA, $V_g = 22$ V, 1 mV a.c. modulation). The dark bands (low $\mathrm{d}I/\mathrm{d}V_s$) marked by the dashed lines in the middle of (a) and (b) represent the classical turning points of the potential.

center[71]. This is consistent with our observation that the apparent energy spacing between resonances ($\Delta\epsilon$) at the center (Fig. 3.2(d)) is approximately double the apparent energy spacing at a point 100 nm away from the center (Fig. 3.2(f)). Scattered quasiparticles (with nonzero angular momenta) external to the potential boundary contribute to Friedel-like oscillations that radiate outwards, as seen in Fig. 3.3. A circular graphene p–n junction with an n-doped interior thus acts as a quantum dot for electron-like carriers and a quantum antidot for hole-like carriers (as in Fig. 3.3), whereas the reverse is true for p–n junctions of opposite polarity (as in Figs 3.2and 3.4).

This qualitative picture can be confirmed by comparing the experimental results to a model based on the two-dimensional massless Dirac Hamiltonian,

$$\hat{H} = -i\hbar v_F \vec{\sigma} \cdot \bigtriangledown_r + U(\vec{r}), \tag{3.1}$$

where where $U(\vec{r})$ is a scalar potential and $\vec{\sigma} = (\sigma_x,\sigma_y)$ are the pseudospin Pauli matrices. Since we are interested in the low-energy eigenstates of the confinement potential, we use a parabolic model $U(\vec{r}) = \text{-}\kappa r^2$ (that is, the lowest order approximation). The curvature of the

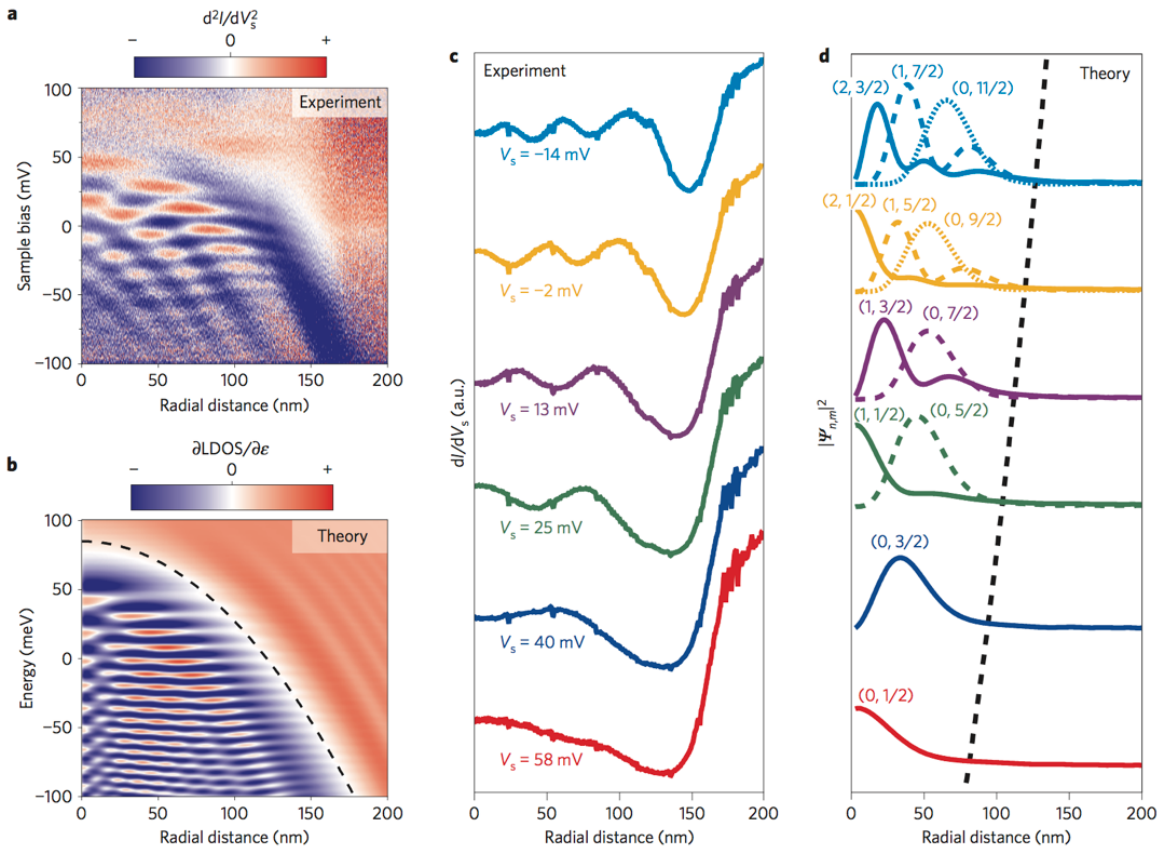

Figure 3.4: Spatially resolving energy levels inside a circular graphene p-n junction. (a) $\mathrm{d}^2I/\mathrm{d}V_s^2$ measured as a function of V_s and the radial distance r from the center of a circular p-n junction having the same polarity as Fig. 3.2. The measurement was performed at a fixed gate voltage (initial tunneling parameters: $V_g = 32$ V, $V_s = 0.1$ V, $I = 1.5$ nA, 1 mV a.c. modulation). (b) Theoretically simulated $\partial LDOS/\partial\varepsilon$ as a function of energy and radial distance for a potential $U(r) = -\kappa r^2$ (potential shown as dashed line). (c) Experimental $\mathrm{d}I/\mathrm{d}V_s$ radial line scans at different V_s values for fixed V_g=32V. (d) Radial dependence of the theoretical probability density $|\psi_{n,m}|^2$ for quantum dot eigenstates. Each curve is labeled by radial and azimuthal quantum numbers (n, m). Each set of theoretical curves has been vertically displaced by a quantity proportional to V_s for the correspondingly colored experimental curve in (c) to ensure that the black dashed line denotes the classical turning points.

potential, κ=6×10^{3}meV/nm^2, was extracted from measurements of the spatially dependent Dirac point energy (see Section 3.3). We solved the Dirac equation to obtain the eigenstates for Dirac fermions in this confinement potential.

Figure 3.4(b) shows the results of our calculations in a plot of ∂LDOS/$\partial\epsilon$, the energy derivative of the LDOS, which corresponds to the experimental quantity $\mathrm{d}^2I/\mathrm{d}V_s^2$. The

resulting eigenstate distribution (Fig. 3.4(b)) closely resembles the experimental eigenstate distribution (Fig 3.4(a)). Both have a characteristic parabolic envelope due to the confinement potential, as well as a complex set of interior nodal patterns. The characteristic energy spacing seen experimentally is in good agreement with the characteristic energy scale $\epsilon^*=(\hbar^2 {v_F}^2\kappa)^{1/3} \approx 15$ meV that arises from the theoretical model. Further insight into the nature of the observed resonances can be gained by directly comparing constant-energy experimental $\mathrm{d}I/\mathrm{d}V_s$ line-cuts (Fig. 3.4(c)) to the modulus square of the simulated quantum dot wavefunctions (Fig. 3.4(d)). Here it is useful to label the confined states by a radial quantum number n = 0, 1, 2,... and an azimuthal quantum number m = $\pm(1/2)$, $\pm(3/2)$,..., that is, $H\Psi_{n,m} = \epsilon_{n,m}\Psi_{n,m}$. To understand the experimentally observed behavior, we note two important properties of the eigenstates $\Psi_{n,m}$. First, although each probability distribution $|\Psi_{n,m}|^2$ features n+1 maxima, most of the weight is concentrated in the first maximum. The position of this maximum is pushed further from the center for larger values of $|m|$ (Fig. 3.4(d)). Second, for massless Dirac fermions confined by a quadratic potential, we observe a near-perfect energy alignment of the states $\Psi_{n,m}$, $\Psi_{n-1,m+2}$, ... at low quantum numbers, indicating an approximate degeneracy. This degeneracy explains why different resonances originating from different $\Psi_{n,m}$ states form the horizontal rows seen in Fig. 3.4(a,b) (which are not perfectly horizontal because the degeneracy is not perfect). Combining these two observations, we are able to attribute each experimental $\mathrm{d}I/\mathrm{d}V_s$ peak in Fig. 3.4(c) to a different $\Psi_{n,m}$ state, wherein each eigenstate contributes most of its spectral weight to a single energy and radial position.

In addition to providing insight into the spatial and spectral distribution of the $\Psi_{n,m}$ states, our simulations also explain other key aspects of the experimental data. In particular, the resonances in our simulation have finite widths, originating from Klein tunneling of confined states into the Dirac continuum. The widths of these resonances lie within the range 4meV to 10meV for both the experimental data and the theoretical simulation. Furthermore, our simulation also explains the striking observation that the apparent energy spacing for the resonances close to the center is nearly twice as large as the spacing away from the center (see Fig. 3.2(d)). This occurs because only the lowest angular momentum states, m=$\pm$1/2, have appreciable wavefunction density at the origin, whereas for all other m values the $\Psi_{n,m}$ states contribute predominantly to off-centered measurements.

3.2.1 Electronic Structure of a Quantum Dot with Opposite Polarity

Figures 3.2 and 3.4 contain STS measurements on a circular p-n junction that is p-doped on the inside and n-doped outside. In these structures, holes are confined to the quantum dot and electrons are scattered. Figures 3.5 and 3.6 show STS measurements obtained for a circular p-n junctions of opposite polarity created by an STM tip-pulse applied at a negative backgate voltage $\tilde{V}_g$ = -40V. Because the confinement potential polarity is flipped, the same confinement mechanism now traps electrons, forming quasibound electronic states inside the

quantum dot while scattering holes.

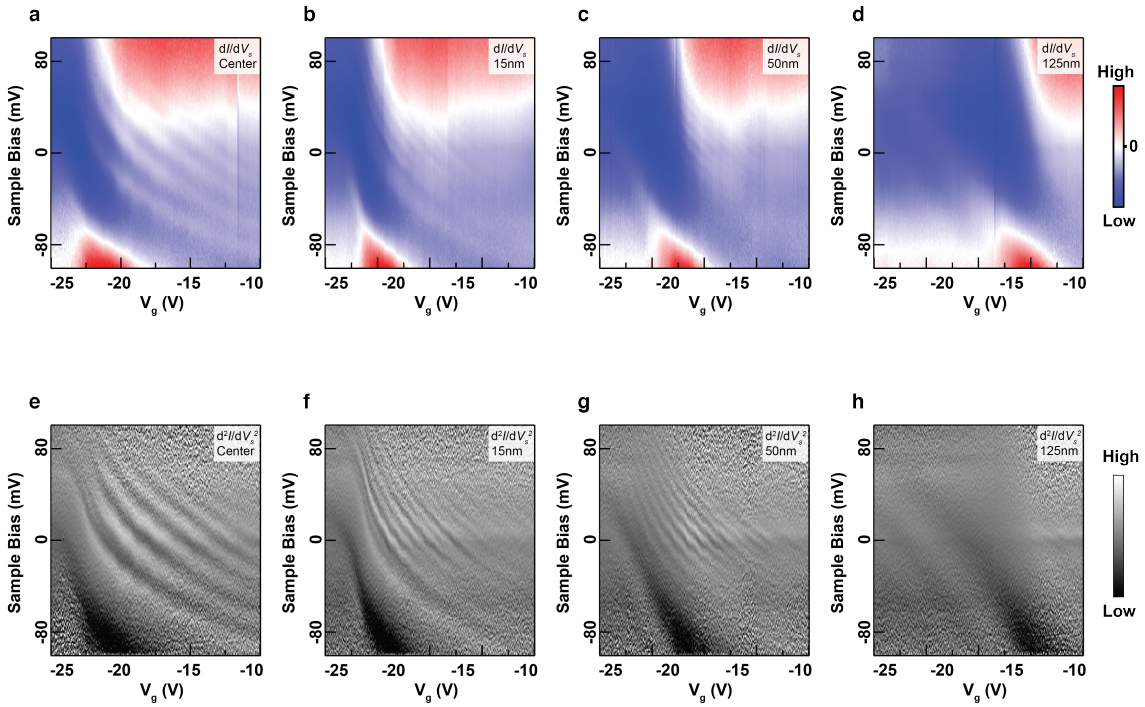

Figure 3.5: Gate-tunable STS measurements of a circular p-n junction with opposite polarity. (a-d) $\mathrm{d}I/\mathrm{d}V_s(V_s, V_g)$ for a p-n junction that is n-doped at the center and p-doped outside. (e-f) $\mathrm{d}^2I/\mathrm{d}V_s^2(V_s, V_g)$ obtained by numerically differentiating (a-d). Initial tunneling parameters for all $\mathrm{d}I/\mathrm{d}V_s$ spectra: V_s=-0.1V, I=1.5nA, $V_{a.c.}$=1mV.

In Figure 3.5(a-d), $\mathrm{d}I/\mathrm{d}V_s(V_s, V_g)$ was obtained at four different distances from the center of a quantum dot. Fig. 3.5(e-h) shows $\mathrm{d}^2I/\mathrm{d}V_s^2(V_s, V_g)$ obtained by numerically differentiating Fig. 3.5(a-d). The most salient oscillatory features correspond to quantum dot resonances whose energies vary as a function of backgate voltage like $\epsilon \propto -\sqrt{|V_g - V_{CNP}|}$+constant, where V_{CNP} is the local charge neutrality point. This behavior is consistent with that of an electronic state in graphene's linear band structure.

Figure 3.6(a) shows spatially resolved STS plotted as $\mathrm{d}I/\mathrm{d}V_s(V_s, r)$. Figure 3.6(b), which is analogous to Figure 3.4(a) is a numerically differentiated plot of Figure 3.6(a). Figure 3.6(b) has very similar features as Figure 3.4(a) except reflected across the horizontal axis, consistent with our expectation for a quantum dot with opposite polarity. There are, however, some differences between the two plots. In Figure 3.6(b), the internal nodal structure is not as prominent while the Friedel-like oscillations on the outside of the quantum dot are more visible. This might be because of the disruptive effect of the tip work function on the quantum dot confinement potential (see Section 3.3).

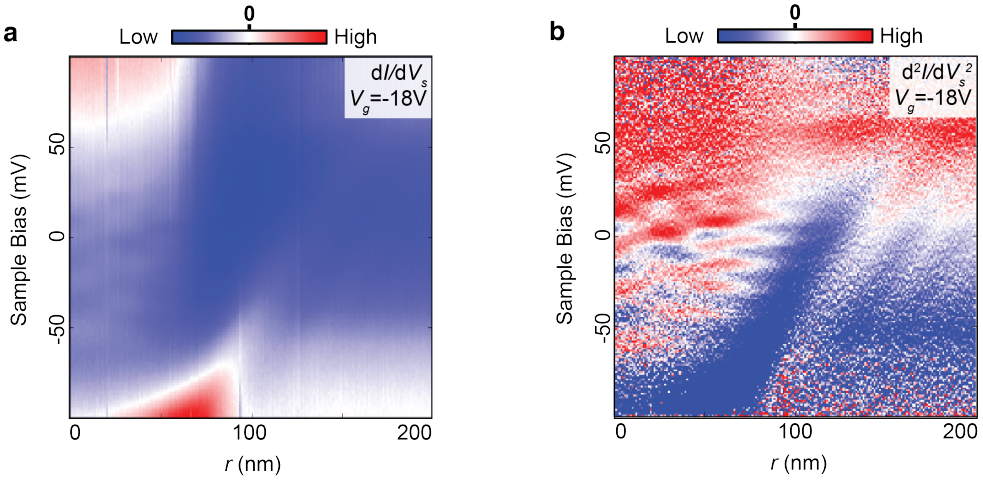

Figure 3.6: Spatially resolved energy level spectrum of p-n junction with opposite polarity. (a) $\mathrm{d}I/\mathrm{d}V_s(V_s, r)$ for a p-n junction that is n-doped at the center and p-doped outside. (b) $\mathrm{d}^2I/\mathrm{d}V_s^2(V_s, r)$ obtained by numerically differentiating (a). Initial tunneling parameters for all $\mathrm{d}I/\mathrm{d}V_s$ spectra: V_s=-0.1V, I=1.5nA, $V_{a.c.}$= 1mV.

3.3 Quantum Dot Confinement Potential

3.3.1 Estimating the Curvature of the Quadratic Potential

We modeled our p-n junction using the 2D massless Dirac Hamiltonian with a quadratic potential, $\hat{H} = -i\hbar v_F \vec{\sigma} \cdot \bigtriangledown_r + \kappa r^2$. We chose κ= $6{\times}10^{-3}$meV/nm^2, and the resulting theoretical simulation (Fig. 3.4(b)) is in good agreement with the experimental data (Fig. 3.4(a)). We estimated the value for κ through scanning tunneling spectroscopy (STS) measurements of the Dirac point, with the assumption that the potential varies slowly enough that the Thomas-Fermi approximation is valid. At each point r away from the center we performed a $\mathrm{d}I/\mathrm{d}V_s$ measurement at fixed V_g such that E_D is outside of the inelastic tunneling gap (to do this we needed to use a value of V_g that is different from the value V_g = 32 V used for the data presented in Fig. 3.4(a)). We then extracted E_D through a parabolic fit, converted E_D to charge carrier density through $n(r) = {E_D}^2(r)/\pi(\hbar v_F)^2$, and rigidly shifted the entire $n(r)$ curve by a uniform constant to match the data at V_g = 32 V (i.e. the gate voltage in Fig. 3.4(a)). The resulting shifted $n(r)$ is plotted in Fig. 3.7(a), and the equivalent E_D is plotted as the blue curve in Fig. 3.7(b). A similar procedure was used to construct the $n(x, y)$ plot in Fig. 3.1(c) (with the E_D measurement performed at V_g = 50 V, and then $n(x, y)$ shifted to match the gate voltage held during the tip pulse). Although the data in Figs 3.2 and 3.4(a) are obtained from the same p-n junction, the data in Fig. 3.3 is from a different but similarly prepared p-n junction.

The blue curve in Fig. 3.7(b) is an approximate representation of the potential felt by Dirac quasiparticles in the p-n junction of Figs 3.2 and 3.4. We extract κ by fitting the blue

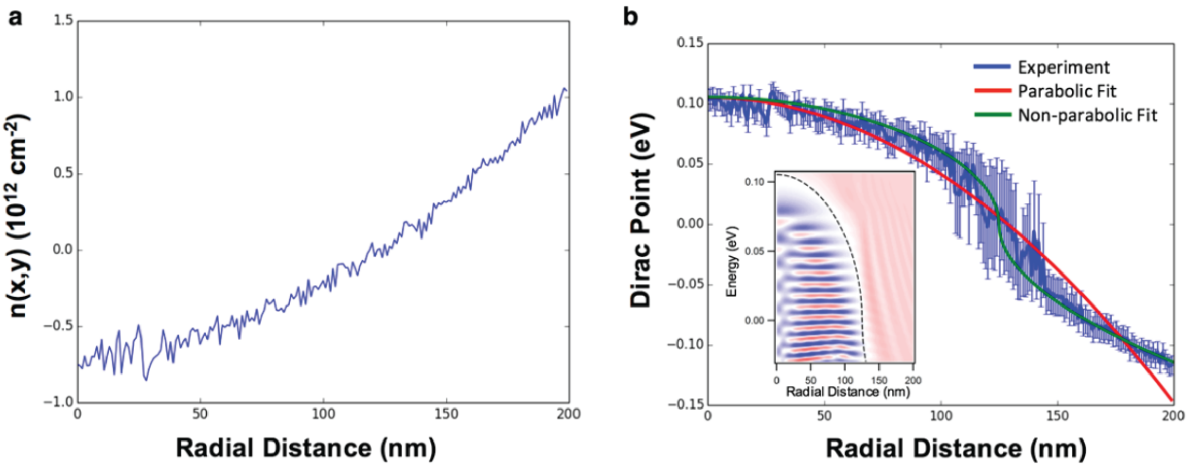

Figure 3.7: Circular electrostatic potential. (a) Charge carrier density for the p-n junction in Fig. 3.5 and Fig. 3.4. (b) Dirac point energy (blue curve) corresponds to (a). The Dirac point energy is fit with a quadratic polynomial with curvature $\kappa = 0.006$ meV/nm^2 (red curve). This value of κ is used to generate the theoretical simulation in Fig. 3.4b. The green curve is a shifted power law fit to the experimental blue curve. The inset is ∂ LDOS/$\partial\epsilon$ calculated for the non-parabolic potential represented by the green curve (which is also the dashed line in the inset).

curve in Fig. 3.7(b) with an even quadratic polynomial (red curve). This procedure results in $E_D(r) = (-6.33 \times 10^{-6}\text{eV/nm})r^2 + (1.05 \times 10^{-1}$ eV), yielding $\kappa = 6 \pm 1 \times 10^{-3}$ meV/nm^2 (corresponding to characteristic energy $\epsilon^* = (\hbar^2 {v_F}^2 \kappa)^{1/3} \approx 15$ meV and characteristic length $r^* = (\hbar v_F/\kappa)^{(1/3)} \approx 50$ nm).

Although the potential in Fig. 3.7(b) (blue curve) deviates from the parabolic fit (red curve), this does not appear to significantly affect the agreement between the experimental and theoretical eigenstate distributions in Figs 3.4(a,b). In order to understand how deviations from a parabolic potential affect our results, we simulated ∂LDOS/$\partial\epsilon$ for a non-parabolic potential $U(r)$ whose carrier density is given by a generic shifted power law function:

$$n(r) = n_\infty - \frac{n_0}{(1 + (r/d)^2)^\gamma}. \tag{3.2}$$

Here $n_\infty = 6 \times 10^{12}$ cm^{-2}, $n_0 = 6.9 \times 10^{12}$ cm^{-2}, and $d = 400$ nm are phenomenological parameters determined by fitting to the experimental potential. For simplicity, we chose $\gamma = \frac{3}{2}$ (which happens to be the power law for the perfect screening of charge spatially separated from graphene (insert citation here)). In the Thomas-Fermi approximation, the potential is given by

$$U(r) = sgn(n(r))\hbar v_F \sqrt{\pi |n(r)|}. \tag{3.3}$$

The above equations for $U(r)$ and $n(r)$ fit the experimental potential quite nicely over the entire spatial range of the measurement (see green curve in Fig. 3.7(b) for fit). The resulting

∂LDOS/$\partial\epsilon$ calculated for this potential (inset in Fig. 3.7(b)) is qualitatively and quantitatively similar to ∂LDOS/$\partial\epsilon$ calculated for the parabolic potential (Fig. 3.4). Thus, the simple parabolic potential model is sufficient to explain our experimental results.

3.3.2 Simulation of Quantum Dot Potential

In Figure 3.4 of Section 3.2, comparison of experimental data to theoretical simulation allowed identification of observed nodes with specific quantum numbers. In simulating the Dirac Hamiltonian, we used the two-dimensional harmonic oscillator, the simplest and most commonly used approximation for a potential well. However, we showed in Section 3.3 that our experimentally inferred quantum dot potential deviates from the harmonic oscillator potential at large radial distance r. We then concluded that the quantum dot electronic structure is robust enough to remain unaffected by the curvature of the confinement potential ny computing the solution to the Dirac equation for another potential that better fits our experiment:

$$n(r) = n_\infty - \frac{n_0}{(1 + (r/d)^2)^\gamma}. \tag{3.4}$$

This potential is physically equivalent to a potential generated by a 1.1 $\times 10^4$ electrons positioned at a point 400 nm below the graphene. However, this is physically unrealistic. The thickness of hBN substrate supporting the graphene is less than 200nm, so it is impossible in the experiment to have a point charge so far away from the surface. Furthermore, it is unlikely that so many electrons are concentrated in a small spatial volume. Hence, this potential clearly does not accurately represent the actual charge distribution.

A natural question arises: what is the charge distribution within the hBN that produces the quantum dot potential observed in the experiment? Unfortunately, we do not have the ability to detect charged defects more than a few layers away from the surface using STM [50] so that direct experimental mapping of charge distribution is impossible. And depending on the parameters of the STM-tip doping process, the charge distribution may vary. In this section, we take a step toward understanding the actual charge distribution by studying a simulation of the Poisson equation for randomly distributed charges within a cylindrical volume of hBN, which induces a confinement potential qualitatively similar to our experiment.

Figure 3.8(a) is a schematic describing the parameters used in our simulation. Point charges are randomly distributed (by a computer program) inside a cylindrical region below the graphene defined by radius ρ and height h. To compute the potential, we use the method of images assuming perfect screening by graphene [72]. The charge density produced by a point charge then becomes:

$$n(r) = n_\infty - \frac{d}{\pi(d^2 + r^2)^{3/2}}, \tag{3.5}$$

where $n(r)$ is the surface charge density at radial distance r from the point charge located d below the graphene and n_∞ is the global charge density induced by the backgate. We then

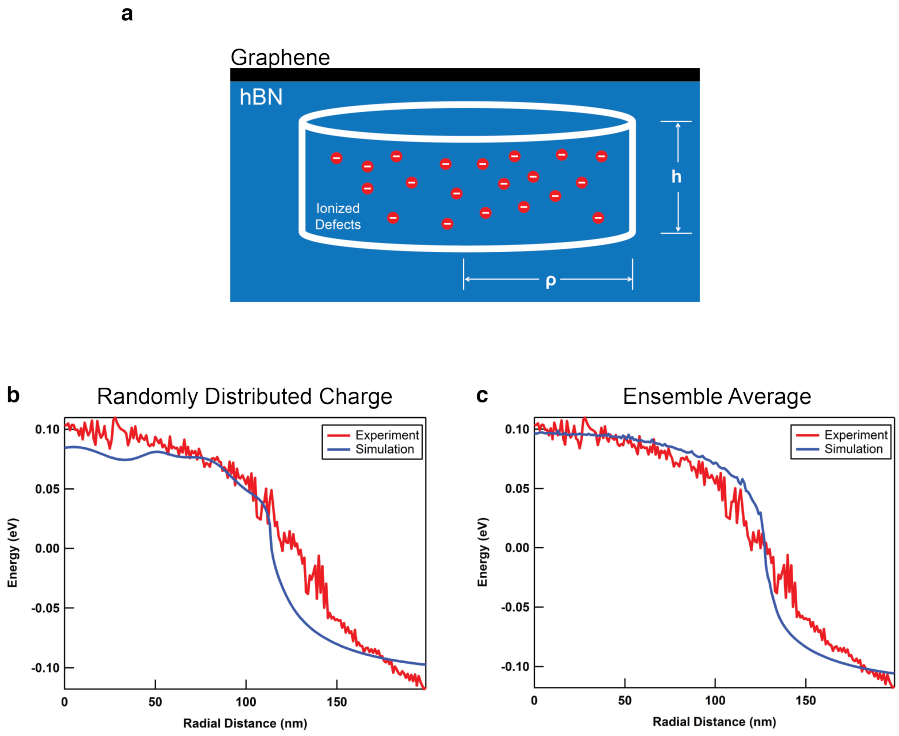

Figure 3.8: Theoretical simulation of potential induced in graphene by a randomly scattered point charges in hBN. (a) Diagram showing charged defects in hBN randomly distributed within a cylindrical region of radius ρ and height h. (b) Comparison of theoretically simulated curve (225 point charges randomly distributed within a cylindrical region of radius ρ=133 nm and height h=100nm). (c) Ensemble average of 10,000 potentials like (b) generated by randomly distributed point charges.

use Thomas-Fermi approximation and compute the electrochemical potential from charge density:

$$U(r) = sgn[n(r)]\hbar v_F \sqrt{\pi |n(r)|}. \tag{3.6}$$

The blue curve in Figure 3.8(b) shows the potential profile for 225 point charges distributed within a cylindrical region of $\rho = 133$ nm and $h = 100$ nm. The blue curve resembles the red curve, which is the experimentally observed quantum dot potential. A notable qualitative difference between the theoretical simulation and the experiment is that the theoretically simulated curve is not monotonic, or 'bumpy,' near the center. This difference may arise from the fact that the actual charge distribution will not be random due to Coulomb repulsion of electrons, which would prevent spatial clustering of charges and result in a more uniform charge distribution than our randomly distributed point charges. Also, the assumption of perfect screening will not be valid for point charges positioned very close to the graphene surface, but this is not accounted for in our simple simulation. Figure 3.8(c) shows an ensemble average of 10,000 potentials induced by randomly distributed

charges such as the one shown in Figure 3.8(b). Mathematically, this type of ensemble average will converge to the potential of a uniformly charged cylinder. The blue curve in Figure 3.8(c) is now monotonic and more closely resembles the experiment. In the actual experiment, electrostatic fields arise from discrete point charges (See Section 2.2), so the ensemble average does not represent an accurate physical picture but makes it plausible that the confinement potential in our experiment is caused by some local distribution of substrate charges. Furthermore, we can make quantitative comparison of our theoretical simulation to the experiment by examining defect densities. The cylindrical region in our theoretical model has charge density $\rho = 10^{16}$ cm^{-3}. This number is consistent with defect density observed in our STM measurements ($\mathrm{d}I/\mathrm{d}V_s$ maps show defect density $\sigma = 10^{10}\mathrm{cm}^{-2}$, which corresponds to volume density $\rho = 10^{17}\mathrm{cm}^{-3}$ assuming that hBN defects up to 5 layers from the surface are detectable via STS). A secondary ion mass spectrometry experiment reports defect density $\rho = 10^{18}\mathrm{cm}^{-3}$ [41].

3.4 The STM Tip as a Floating Top Gate

We have thus far limited our discussion of electrostatic gating on graphene to the embedded substrate gates fabricated by applying voltage pulse to an STM tip. However, another source of electrostatic gating in our experiment is the STM tip, which acts as a floating top gate on the graphene[53]. In this section, we discuss the competing effects of these two gates and provide justification for why we can safely disregard the effect of the STM tip in certain circumstances.

Our STM tips were fabricated by etching a plantinum iridium wire and calibrated by spectroscopic detection of the Au(111) Shockley surface state. Due to the work function difference between the graphene and the STM tip, the graphene tends to be locally p-doped in a small region below the STM tip [17, 53]. In conjunction with the back gate, this local top gating by the STM tip can produce quasibound quantum dot states [17]. Figure 3.9(a) shows $\mathrm{d}I/\mathrm{d}V_s(V_s, V_g)$ plot measured on pristine graphene without any embedded gate and Figure 3.9(d) is a numerically differentiated plot of Figure 3.9(a). Resonances that vary in energy as a function of the backgate like $\varepsilon \propto \sqrt{|V_g - V_{CNP}|}$ is observed, indicating the presence of bound hole states.

Because our STM tip tends to be negatively charged [53], when the embedded gate is also negative, the STM tip gating increases the strength of the confinement potential. On the other hand, when the embedded gate is positive, then the STM tip gating opposes and interferes with the confinement potential generated by the embedded gate. In this section, we examine the latter case to explore the relative strengths of each type of gate.

On the same location of the graphene with the same STM tip that was used to obtain Figure 3.9(a,d), we created a positive local embedded gate by applying a voltage pulse to the STM tip while holding the backgate at $\tilde{V}_g = -20V$. Figure 3.9(b,e) shows $\mathrm{d}I/\mathrm{d}V_s(V_s, V_g)$ and $\mathrm{d}^2I/\mathrm{d}V_s^2(V_s, V_g)$ at the center of the STM tip pulse. Compared to Figure 3.9(a,d), resonances on the hole side of the Dirac point have become fainter while new resonances appear on the

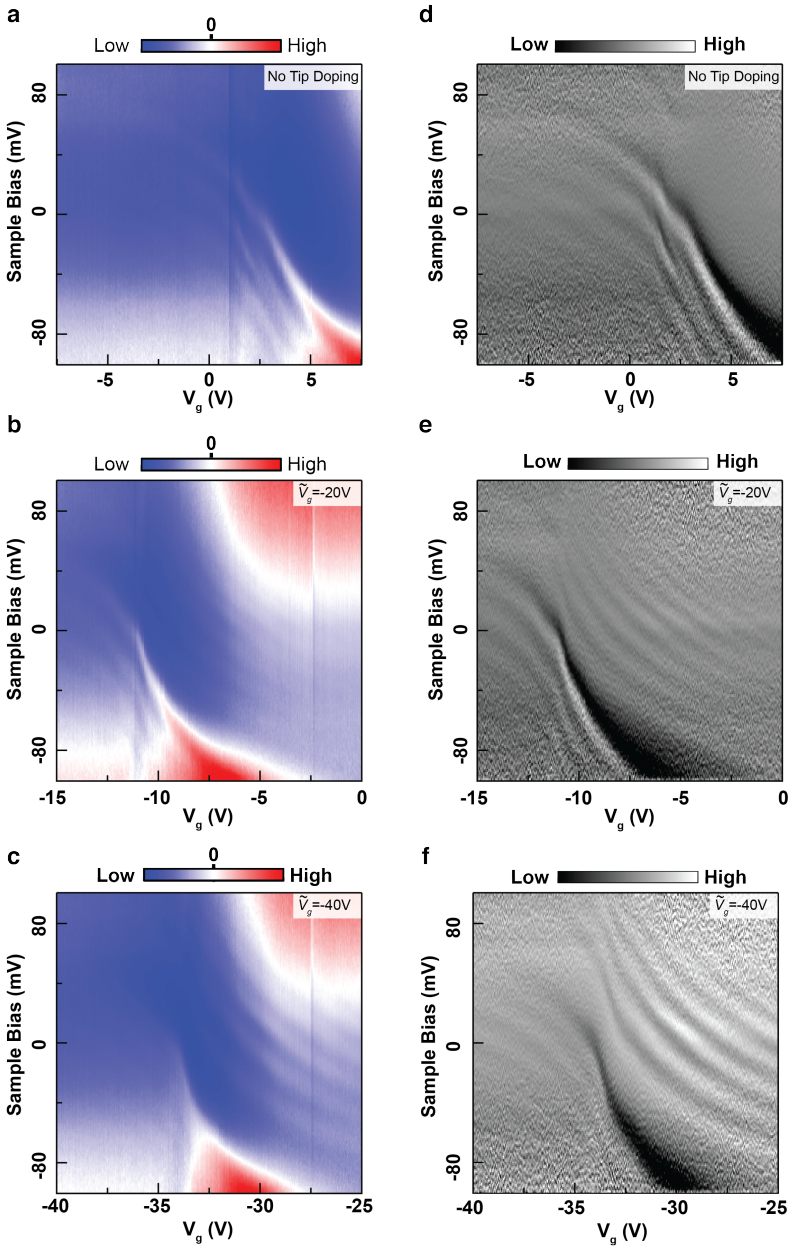

Figure 3.9: Effect of tip gating on quantum dot confinement potential. (a) $\mathrm{d}I/\mathrm{d}V_s(V_s, V_g)$ plot of graphene without any tip doping. (b-c) $\mathrm{d}I/\mathrm{d}V_s(V_s, V_g)$ measured after the graphene was locally n-doped with an STM tip pulse at $\tilde{V}_g$ =-20V for (b) and $\tilde{V}_g$ =-40V for (c). For both (b) and (c), tip pulses were applied at h_{lift}=1.68nm, V_s=5V, and Δt=1 min. (d-f) $\mathrm{d}^2I/\mathrm{d}V_s^2(V_g, V_s)$ plots generated by numerical differentiation of (a-c). Initial tunneling parameters for all $\mathrm{d}I/\mathrm{d}V_s$ spectra: V_s=-0.1V, I=1.5nA, $V_{a.c.}$ = 1mV.

electron side of the Dirac point that vary as a function of V_g like $\varepsilon \propto -\sqrt{|V_g - V_{CNP}|}$. This emergence of new electronic resonances indicates confined quantum dot electronic states induced by the embedded gate. We can further understand the interplay of the STM tip gate and the embedded gate by changing the tip doping parameter $\tilde{V}_g$.

Figure 3.9(c,f) shows the $\mathrm{d}I/\mathrm{d}V_s(V_s, V_g)$ and $\mathrm{d}^2I/\mathrm{d}V_s^2(V_s, V_g)$ plots obtained on the location of the graphene with the same STM tip, but after erasing the previously fabricated embedded gate and creating a new embedded gate with an STM tip pulse at $\tilde{V}_g = -40V$. This would create a stronger embedded gate than the one created with $\tilde{V}_g = -20V$. Compared

to Figure 3.9(b,e), the electronic resonances have become more prominent while confined hole states have become barely visible. Thus, we can conclude that it is possible to make the embedded gate the dominant contributor to the electrostatic potential over the STM tip gate.

Chapter 4

Coupled Quantum Dots in Monolayer Graphene

In this chapter, we present our STM investigation of coupled graphene quantum dots. By tuning the tunnel barrier height and the separation distance between quantum dots, we demonstrate control over inter-dot coupling strength. Spatially resolved STS on coupled quantum dot systems provide insight into the transition from weak coupling to strong coupling between graphene quantum dots.

In Section 4.2, we fabricate two quantum dots separated by 400 nm and present distance-dependent $\mathrm{d}I/\mathrm{d}V_s$ spectroscopy and $\mathrm{d}I/\mathrm{d}V_s$ maps at various backgate voltages. Our experimental data suggest that in this regime, the two quantum dots act as independent artificial nuclei that interact with each other via Klein tunneling.

In Section 4.3, we fabricate two quantum dots separated by 300 nm and present distance-dependent $\mathrm{d}I/\mathrm{d}V_s$ spectroscopy and $\mathrm{d}I/\mathrm{d}V_s$ maps at various backgate voltages. Our spectroscopic measurements indicate that in this regime, the wavefunctions of two quantum dots begin to merge, representing the transition from weakly coupled to strongly coupled quantum double dots.

In Section 4.4, we fabricate two quantum dots separated by 200 nm and present distance-dependent $\mathrm{d}I/\mathrm{d}V_s$ spectroscopy and $\mathrm{d}I/\mathrm{d}V_s$ maps at various backgate voltages. In this regime, the two quantum dots are strongly coupled, producing new features in $\mathrm{d}I/\mathrm{d}V_s$ spectra and maps.

In Section 4.5, we fabricate arrays of four quantum dots and visualize their electronic structure. Our results open the door to an exciting direction for future studies and applications of graphene quantum dot systems.

4.1 Introduction

Quantum double dot systems make possible rich new physics and applications unavailable to single quantum dots such as accurate lifetime measurements[73], Pauli blockade phe-

nomenon[74], and quantum computing[75]. In graphene, however, coupled quantum dot systems defined by p-n junctions remain largely unexplored. And unlike semiconductor quantum dots, interactions between graphene quantum dots are governed by the physics of Klein tunneling, which should produce novel properties. In this chapter, we take a step towards understanding systems of coupled quantum dots in graphene by fabricating multiple quantum dots and spatially mapping the resulting distribution of Dirac fermions. Spatially resolved STS provides information about inter-dot tunnel coupling in quantum double dots and indicates transition from weak bonding to strong bonding[73]. By adjusting inter-dot distance and backgate voltage, we demonstrate the ability to tune the interaction between graphene quantum dots.

4.2 Quantum Double Dots with Weak Coupling

We applied voltage pulses to an STM tip at two locations separated by a distance of 400 nm ($\tilde{V_g}$ =-40V, h_{lift}=1.8nm, V_s=5V, Δt=1 minute). We then obtained $\mathrm{d}I/\mathrm{d}V_s$ spectra at various locations along a line connecting the locations of the two STM tip voltage pulses. Figs 4.1d-i show these spectra plotted as $\mathrm{d}^2I/\mathrm{d}V_s^2(d, V_s)$ for nine different values of V_g. The features in $\mathrm{d}I/\mathrm{d}V_s$ spectra evolve gradually as V_g is varied. These plots are approximately symmetric about the center (d =200 nm), as is expected from our symmetric measurement scheme. The middle region around d =200nm shows oscillatory features begin to appear at V_g = -5V and grow in size and complexity as V_g is decreased. Around V_g=-20V, however, they begin to fade until only faint oscillations are visible at V_g=-22V. The middle region is always enveloped by dark lines on both left and right. At V_g=-5V, there are no conspicuous features near d =0nm and d =400nm. As V_g is decreased, oscillatory features appear (between V_g=-6.5V and V_g=-20V), until they also become largely undetectable at V_g=-22V.

Figure 4.2 shows 400nm by 400nm $\mathrm{d}I/\mathrm{d}V_s$ maps obtained on a region of graphene where two voltage pulses were applied 400 nm apart from each other, as depicted in the measurement scheme in Fig. 4.1c (Figure 4.2 was prepared in a similar way as Figure 4.1 but on a different region of graphene with a different STM tip). Circular interference patterns appear on the upper right and lower left. As V_g is increased, the number of nodes within the circular structures increases. There are also interference patterns between the two circular structures. For lower value of V_g (-12V and -10V), these appear as extensions of the circular structures and do not interact much with each other. But for higher values of V_g (-7V and -5V), they begin to overlap and evolve into checker-like interference patterns.

We applied two voltage pulses separated by 400 nm with parameters $\tilde{V_g}$=40V, d_{lift}=1.9nm, V_s=5V, and Δt=1 min. Then $\mathrm{d}I/\mathrm{d}V_s$ spectra were obtained along an axis going through the positions of two voltage pulses, as schematically represented in Fig. 4.3c. $\mathrm{d}^2I/\mathrm{d}V_s^2(d, V_s)$ plots are shown in Figs 4.3d-f for three values of V_g. Two complex nodal patterns appear in $\mathrm{d}^2I/\mathrm{d}V_s^2(d, V_s)$ and, as V_g is increased, the nodal patterns shift down in V_s and the energy spacing between nodes becomes larger.

$\mathrm{d}I/\mathrm{d}V_s$ maps were obtained at various values of V_s and V_g on a region of graphene where

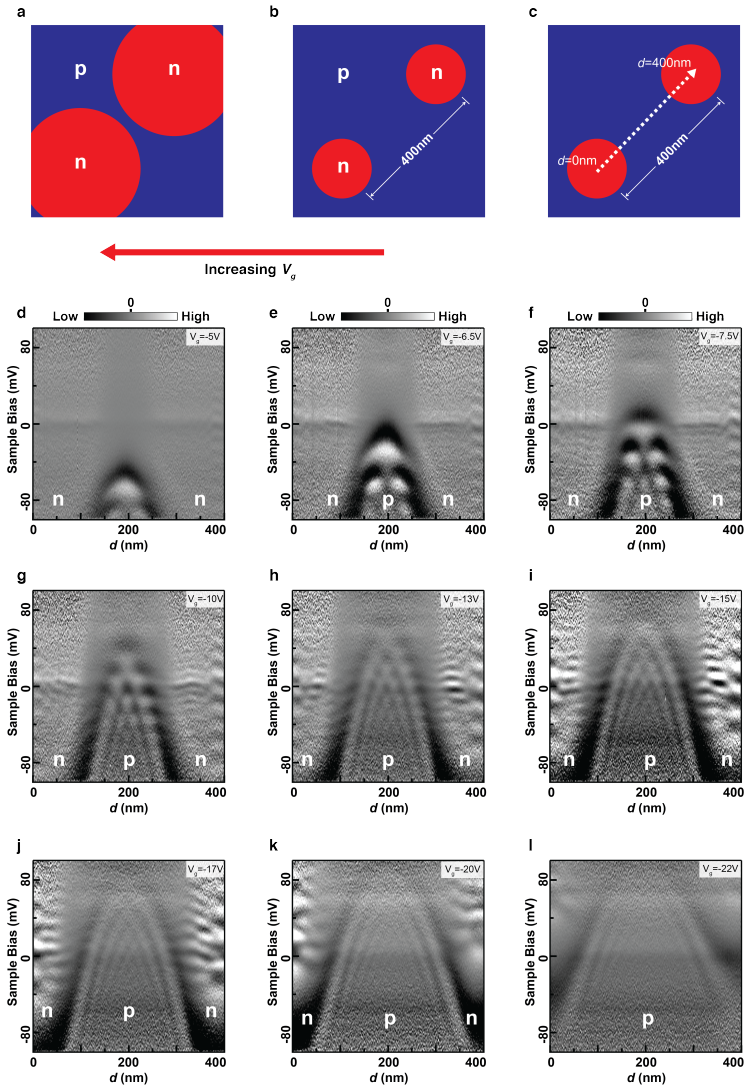

Figure 4.1: Electronic Structure of Electron Quantum Dots in Graphene Separated by 400 nm. (a-c) Schematic indicating locations of the quantum dots. The two quantum dots were fabricated by locally n-doping graphene with an STM tip pulse at $\tilde{V_g}$ =-40V, h_{lift}=1.8nm, V_s=5V, Δt=1 minute. Distance d is defined as shown in (c), where d=0 denotes the center of one quantum dot and d=400 nm is the center of the other quantum dot. As V_g increases, the quantum dot becomes larger. d-l, $\mathrm{d}^2I/\mathrm{d}V_s^2(d, V_s)$ at various backgate voltages V_g. Initial tunneling parameters for all $\mathrm{d}I/\mathrm{d}V_s$ spectra: V_s=-0.1V, I=1.5nA, $V_{a.c.}$=1mV.

two voltage pulses were performed 400 nm apart from each other while the backgate was sustained at $\tilde{V_g}$=40V. Same values of $\tilde{V_g}$ and separation distance were used in Fig. 4.3 as in Fig. 4.4, but the procedure was performed on a different region of graphene with a different STM tip. The interference patterns appear very similar to the $\mathrm{d}I/\mathrm{d}V_s$ maps in Fig. 4.2.

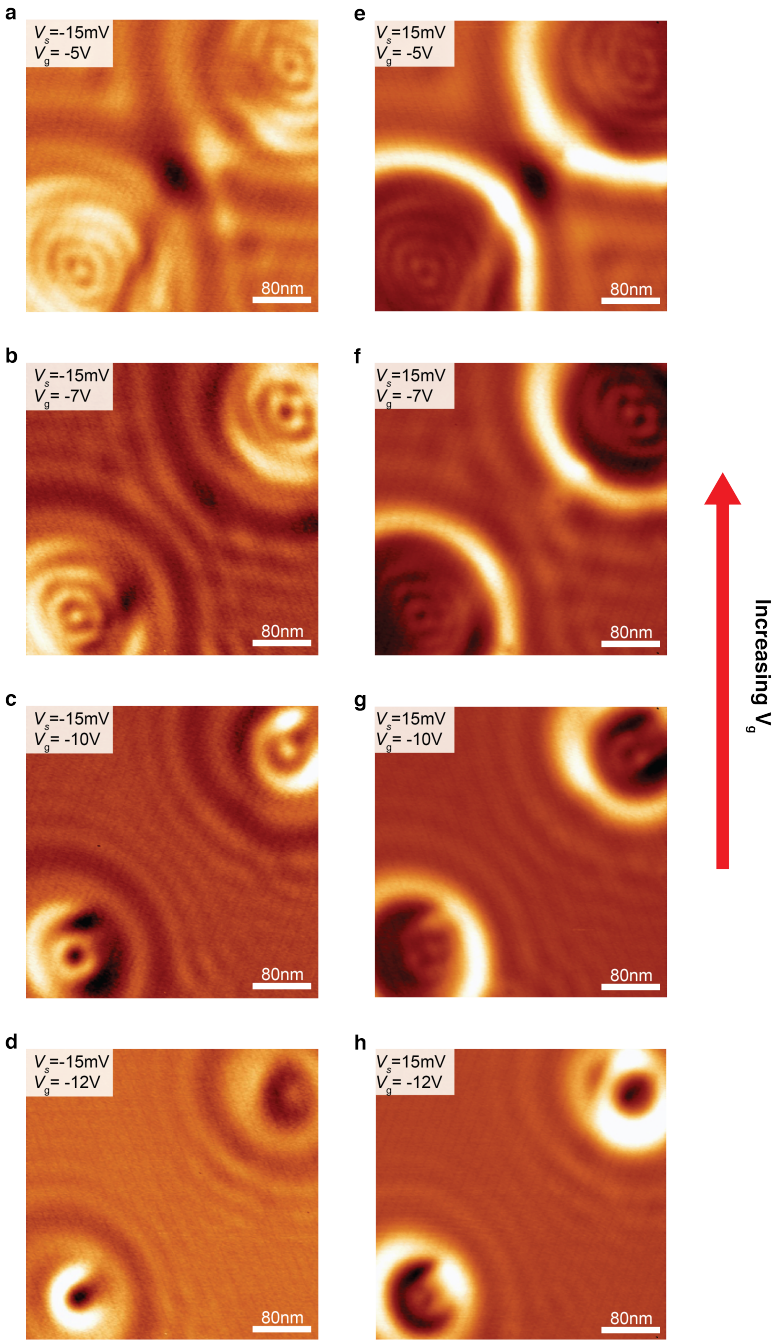

Figure 4.2: Interference Patterns of Electron Quantum Dots in Graphene Separated by 400 nm. (a-d) dI/dV_s maps acquired at various backgate voltages for sample bias V_s=-15mV. The two quantum dots were fabricated with STM tip pulses at $\tilde{V}_g$ =-40V, h_{lift}=1.9nm, V_s=5V, Δt=1 minute. (e-h) dI/dV_s maps acquired at various backgate voltages for sample bias V_s=15mV. As V_g increases, the quantum dot size increases. Tunneling parameters for all dI/dV_s maps: I=50 pA, $V_{a.c.}$=2 mV.

There are two circular patterns that expand in size and number of internal nodes as V_g is decreased. The wave patterns outside of the circular structures are decoupled for large values of V_g (18V, 21V), but they interact and form checker patterns for small values of V_g (13V, 15V).

We now provide interpretation of our spectroscopic measurements on graphene where

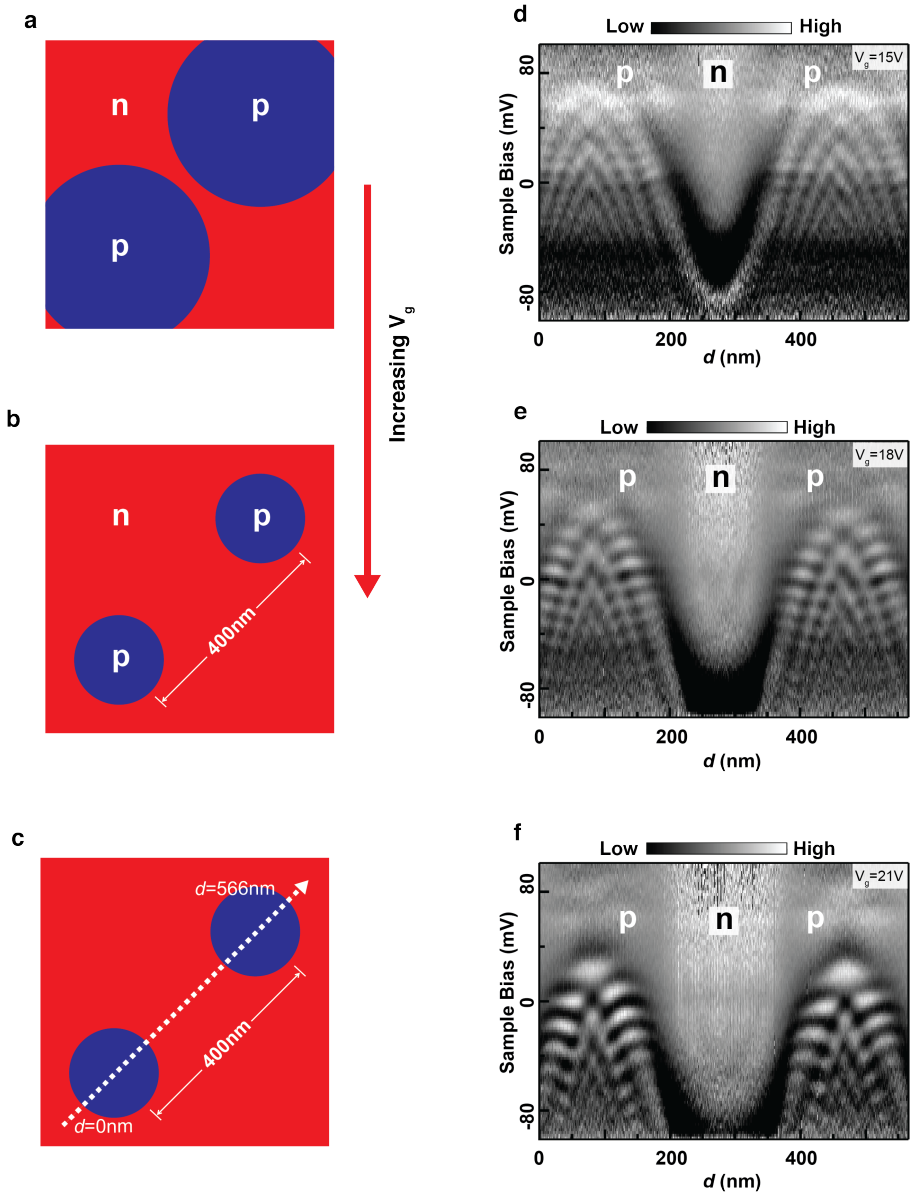

Figure 4.3: Electronic structure of Hole Quantum Dots in Graphene Separated by 400 nm. (a-c) Schematic indicating the location of the quantum dots. The two quantum dots were fabricated by locally p-doping graphene with an STM tip pulse at $\tilde{V_g}$ =40V , d_{lift}=1.9nm, V_s=5V, Δt=1 min. As V_g increases, the quantum dots become smaller. Distance d is defined as shown in (c). (d-f) $\mathrm{d}^2I/\mathrm{d}V_s^2(d, V_s)$ at various backgate voltages V_g. Initial tunneling parameters for all $\mathrm{d}I/\mathrm{d}V_s$ spectra: V_s=-0.1V, I=1.0nA, $V_{a.c.}$=2mV.

two STM tip voltage pulses were applied 400 nm away from each other. Comparison of these data with our experimental observations for single, circular p-n junctions explored in

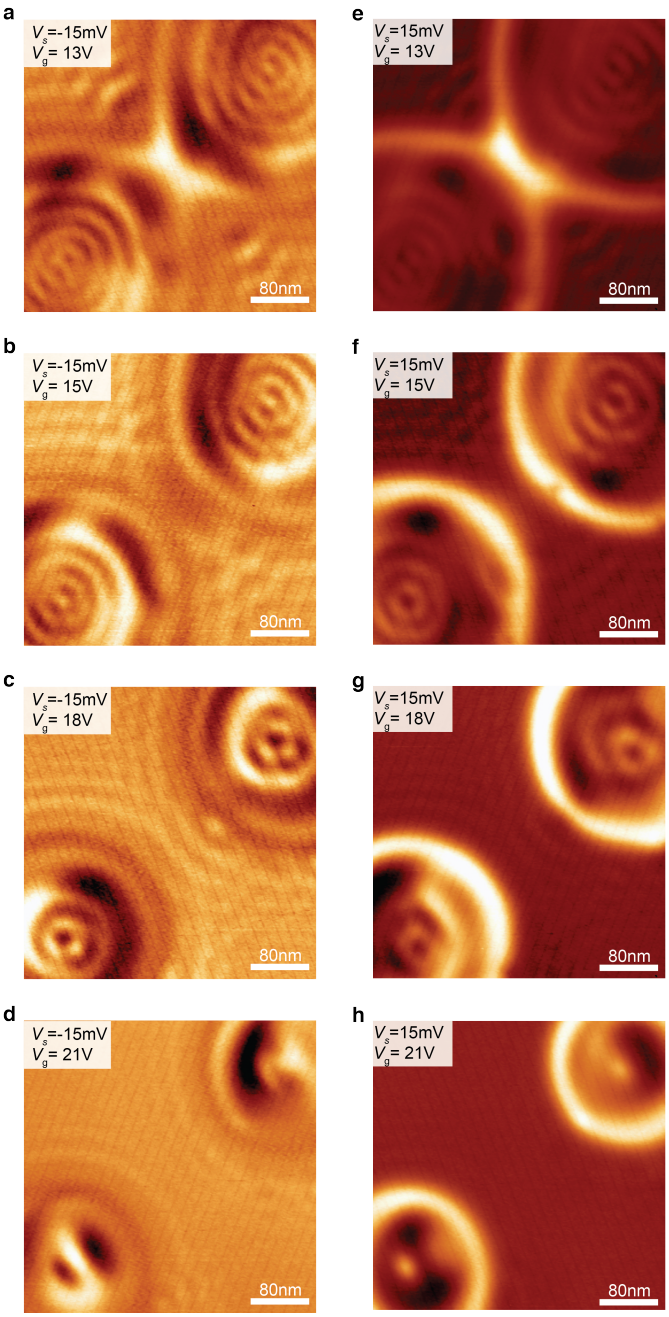

Figure 4.4: Interference Patterns of Hole Quantum Dots in Graphene Separated by 400 nm. (a-d) $\mathrm{d}I/\mathrm{d}V_s$ maps acquired at various backgate voltages for sample bias V_s=-15mV. The two quantum dots were fabricated with STM tip pulses at $\tilde{V}_g$ =40V, h_{lift}=1.9nm, V_s =5V, Δt=1 minute. (e-h) $\mathrm{d}I/\mathrm{d}V_s$ maps acquired at various backgate voltages for sample bias V_g=15mV. As V_g increases, the quantum dot size decreases. Tunneling parameters for all $\mathrm{d}I/\mathrm{d}V_s$ maps: I=50 pA, $V_{a.c.}$= 2mV.

Chapter 3 suggests that these systems consist of two separate quantum dots interacting with each other via Klein tunneling.

First, our spectroscopic measurements indicate that the internal electronic structures of these circular p-n junctions remain largely unaffected by the presence of another dot 400 nm away. This is evident in $\mathrm{d}^2I/\mathrm{d}V_s^2(d, V_s)$ plots (Figs 4.1 and 4.3), where the nodal structure at two pulse locations are similar to those observed for single quantum dots in Chapter 3. As

indicated in the plots, the dark envelopes represent the Dirac point that separates p-doped regions from n-doped regions. N-doped (p-doped) region in Fig. 4.1 (Fig. 4.3) represents the inside of an electron (hole) quantum dot and the n-doped (n-doped) region represents the region between the quantum dots. Our interpretation is further supported by $\mathrm{d}I/\mathrm{d}V_s$ maps (Figs 4.2 and 4.4), where the circular symmetry of these internal interference patterns remain largely intact despite the presence of the other quantum dot.

Second, our experimental data suggest the possibility of inter-dot interaction via Klein tunneling. In Fig. 4.1, Friedel-like oscillations are observed in the inter-dot region for V_g =20V and 22V. These can be interpreted as scattering states discussed in Section 3.2. Below V_g =17V, however, Friedel-like oscillations begin to interfere with each other, forming intricate and well-defined nodal patterns. This indicates that at these values of V_g, each quantum dot falls within the spatial extent of the other quantum dot's scattering states. At this point, the two quantum dots may begin to interact via these inter-dot states within the tunnel barrier whose properties are determined by Klein tunneling-related physics. Interestingly, these inter-dot states are not visible in $\mathrm{d}^2I/\mathrm{d}V_s^2(d, V_s)$ plots of p-doped quantum double dots (Fig. 4.3). In p-doped quantum dots, the Friedel oscillations always appear suppressed, which may be an effect of the STM tip work function (See Chapter 3). In $\mathrm{d}I/\mathrm{d}V_s$ maps (Fig. 4.4), however, both polarities exhibit oscillatory interference patterns in the inter-dot regions.

4.3 Quantum Double Dots with Intermediate Coupling

We used our STM tip voltage pulse technique at two positions on graphene 300 nm apart from each other while holding the backgate at $\tilde{V}_g$=-40V. Then we measured $\mathrm{d}I/\mathrm{d}V_s$ along an axis going through the two tip pulse positions according to the measurement scheme in Fig. 4.7c, then we plotted them as $\mathrm{d}^2I/\mathrm{d}V_s^2(d, V_s)$ in Figs 4.7d-l for nine different values of V_g. The voltage pulses were performed at d=0 nm and d= 300 nm. An nodal structures at these positions appear faintly at V_g = -5V, and as V_g is decreased, these structures become more prominent until they become undetectable around V_g = -22V. Interference patterns appear in the region between the tip pulse positions as well in this range of V_g.

$\mathrm{d}I/\mathrm{d}V_s$ maps were obtained on a region of graphene where tip pulses were applied 300 nm apart from each other with $\tilde{V}_g$=-40V, as shown in Fig. 4.6. For lower values of V_g (-5V and -3V), the two circular structures appear more or less separated from each other. For higher values of V_g (-1V and 1V), however, the two circular structures begin to merge. In these maps, there is a bright Cassini oval-shaped band enveloping the two circular structures.

STM voltage tip pulses were applied twice at positions 300 nm apart from each other while the backgate was held at $\tilde{V}_g$=-40V. Afterwards, $\mathrm{d}I/\mathrm{d}V_s$ spectra were measured at various positions as sketched in Fig. 4.7c. Figs. 4.7d-i are $\mathrm{d}^2I/\mathrm{d}V_s^2(d, V_s)$ plots obtained at six different values of V_g. Two nodal structures appear at the locations of voltage pulses.

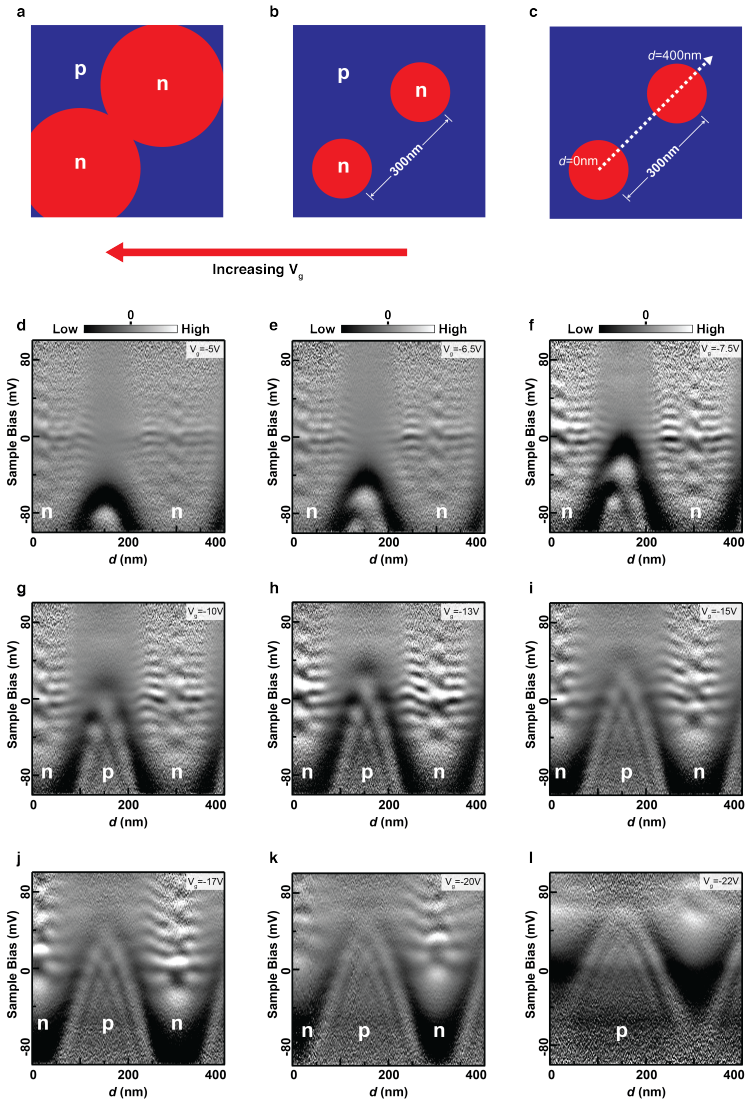

Figure 4.5: Electronic structure of Electron Quantum Dots in Graphene Separated by 300 nm. (a-c) Schematic indicating the location of the quantum dots. The two quantum dots were fabricated by locally n-doping graphene with STM tip pulses at $\tilde{V_g}$ =-40V, h_{lift}=1.9nm, V_s=5V, Δt=1 min. Distance d is defined as shown in (c), where d=0 nm is at the center of one quantum dot and the other quantum dot is located at d=300nm. (d-l) $\mathrm{d}^2I/\mathrm{d}V_s^2(d, V_s)$ at various backgate voltages V_g. Initial tunneling parameters for all $\mathrm{d}I/\mathrm{d}V_s$ spectra: V_s=-0.1V, I=1.0nA, $V_{a.c.}$= 2mV.

And at low values of V_g, the two structures appear to merge and interact with each other.

Similar procedure was performed on a different graphene area (two voltage pulses 300 nm apart from each other at $\tilde{V_g}$=-40V) and 400 nm by 400 nm $\mathrm{d}I/\mathrm{d}V_s$ maps were obtained, as shown in Fig. 4.8. At a high value of V_g (17V), two circular structures appear to be sepa-

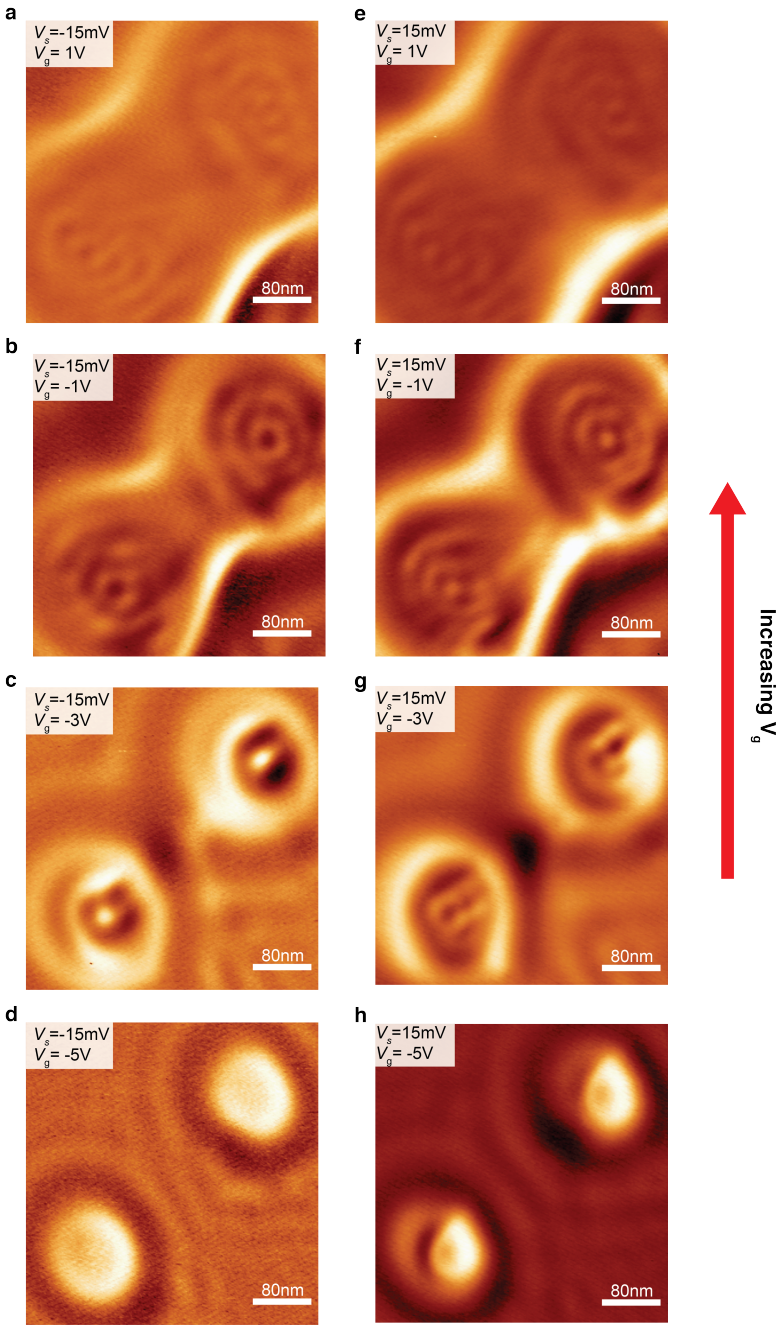

Figure 4.6: Interference Patterns of Electron Quantum Dots in Graphene Separated by 300 nm. (a-d) $\mathrm{d}I/\mathrm{d}V_s$ maps acquired at various backgate voltages for sample bias V_s=-15mV. The two quantum dots were fabricated with STM tip pulses at $\tilde{V}_g$ =-40V, h_{lift}=1.9nm, V_s=5V, Δt=1 min. e-h, $\mathrm{d}I/\mathrm{d}V_s$ maps acquired at various backgate voltages for sample bias Vs=15mV. As V_g increases, the quantum dot size increases. Tunneling parameters for all $\mathrm{d}I/\mathrm{d}V_s maps$: $I = 1.0nA, V_{a.c.} = 2mV$.

rate, though interference patterns emanating from these structures overlap to form checker patterns. At lower values of V_g, the two circular structures are merged together and enveloped by Cassini oval-shaped bands. At lower values of V_g, the internal structure of the two structures gradually lose their circular symmetry.

Our experimental data on graphene where two pulses separated by 300 nm can be understood as two interacting p-doped (n-doped) quantum dots whose wavefunctions begin to

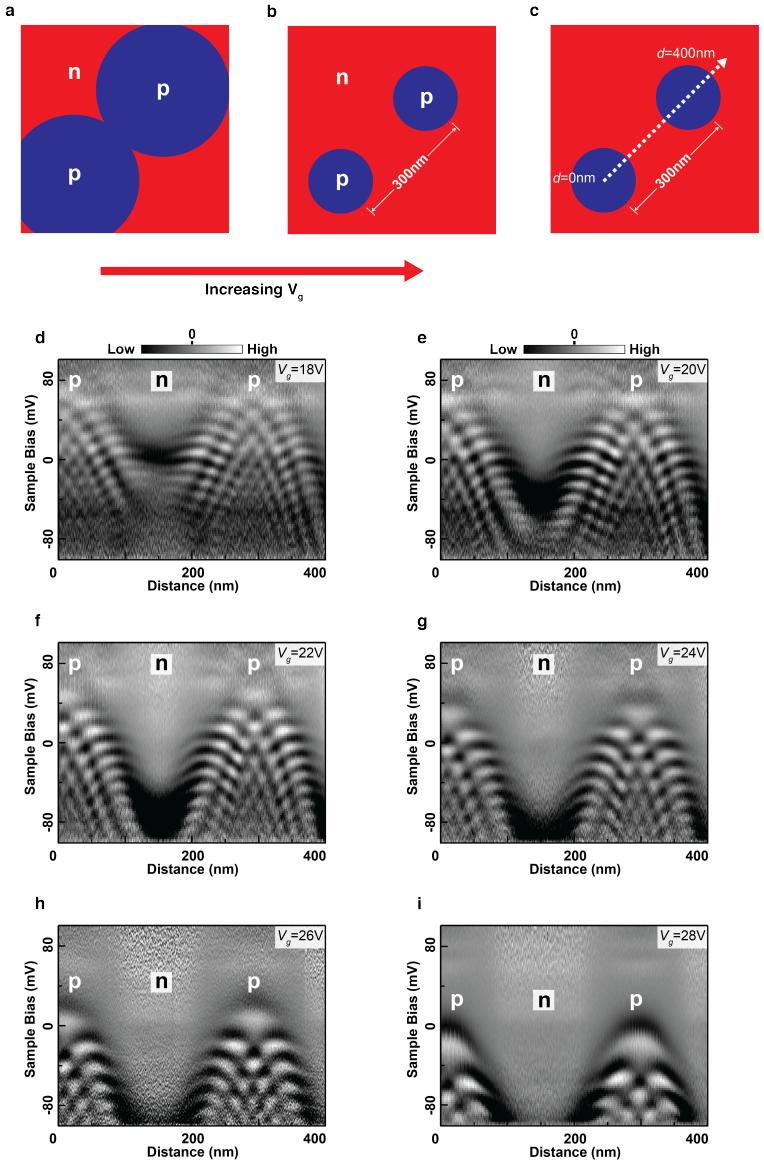

Figure 4.7: Electronic structure of Hole Quantum Dots in Graphene Separated by 300 nm. (a-c) Schematic indicating the location of the quantum dots. The two quantum dots were fabricated by locally p-doping graphene with STM tip pulses at $\tilde{V_g}$ =40V, h_{lift}=1.9nm, V_s=5V, Δt=1 min. Distance d is defined as shown in (c), where d=0 nm is at the center of one quantum dot and the other quantum dot is located at d=300nm. (d-l) $\mathrm{d}^2I/\mathrm{d}V_s^2(d, V_s)$ at various backgate voltages V_g. Initial tunneling parameters for all $\mathrm{d}I/\mathrm{d}V_s$ spectra: V_s=-0.1V, I=1nA, $V_{a.c.}$= 2mV.

overlap and merge at lower (higher) values of the backgate voltage. At large (small) values of V_g in Figs 4.8e,j and Figs 4.7f-i (Figs 4.6c-d, g-h, and Figs 4.5h-l) the data look similar

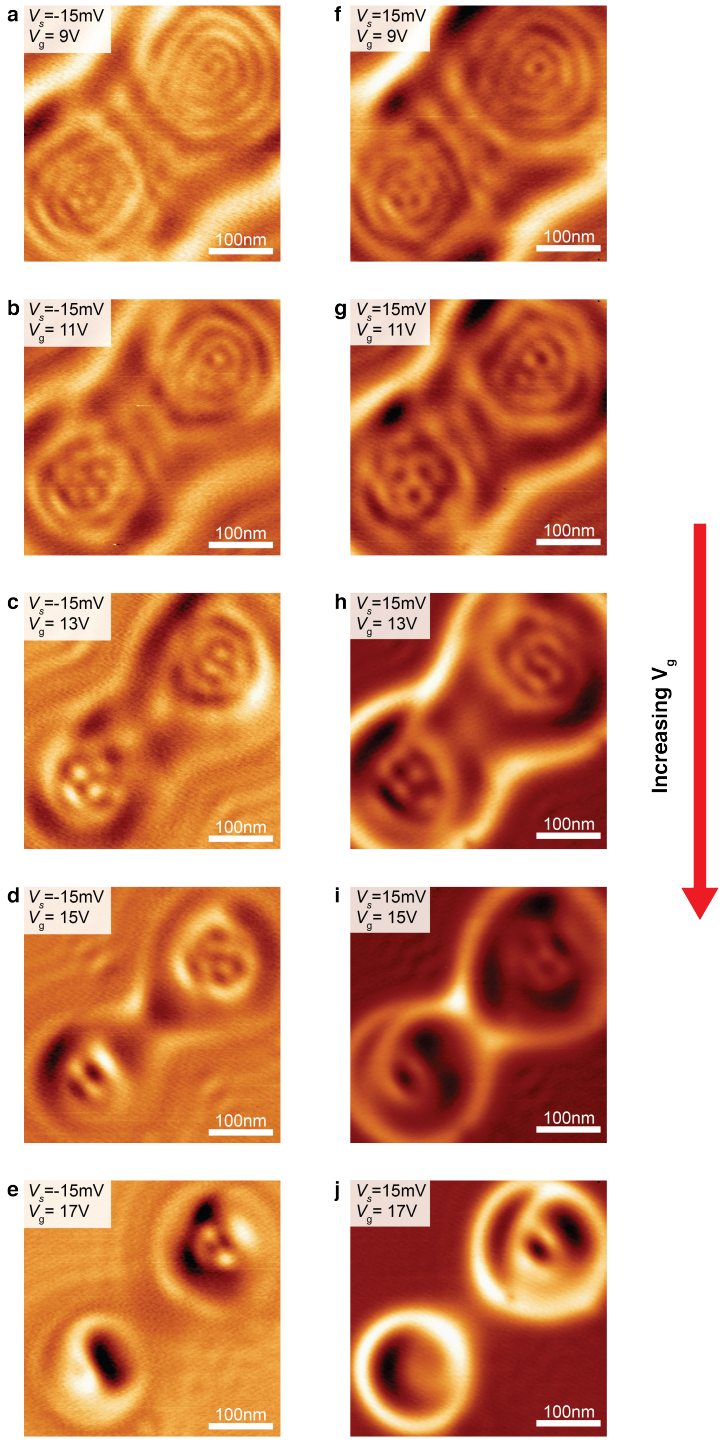

Figure 4.8: Interference Patterns of Hole Quantum Dots in Graphene Separated by 300 nm. (a-d) $\mathrm{d}I/\mathrm{d}V_s$ maps acquired at various backgate voltages for sample bias V_s=-15mV. The two quantum dots were fabricated with STM tip pulses at $\tilde{V}_g$ =40V, h_{lift}=1.9nm, V_s=5V, Δt=1 min. (e-h) $\mathrm{d}I/\mathrm{d}V_s$ maps acquired at various backgate voltages for sample bias V_s=15mV. As V_g increases, the quantum dot size decreases. Tunneling parameters for all $\mathrm{d}I/\mathrm{d}V_s$ maps: I=50 pA, $V_{a.c.}$= 2mV.

to that of two distinct, interacting quantum dots like those in Section 4.2. As the backgate is lowered (raised), however, the inter-dot tunnel barrier is gradually reduced, turning into a small dip (bump) in $\mathrm{d}^2I/\mathrm{d}V_s^2(d, V_s)$ plots and disappearing in $\mathrm{d}I/\mathrm{d}V_s$ maps. When this

occurs, the wavefunctions from two quantum dots begin to have significant overlaps. As the gate is lowered (raised), the wavefunction overlap becomes increasingly more significant and the interference patterns in each pulse location gradually lose their circular symmetry, as evident in Fig. 4.8 (Fig. 4.6). Here, the confined states are distinguished from scattering states by a bright band that separates nodal internal interference patterns with Cassini oval-shaped outside oscillations, which can be interpreted as Friedel-like external oscillations. The fact that the wavefunctions begin to form one combined internal structure suggests that a transition from weakly coupled quantum double dots to strongly coupled quantum double dots is occurring in this regime.

4.4 Quantum Double Dots with Strong Coupling

STM tip voltage pulses were applied with $\tilde{V}_g$=-40V at two locations separated by 200 nm, as shown in Fig. 4.9b. Afterwards, $\mathrm{d}I/\mathrm{d}V_s$ spectra were performed at various distance along an axis starting from one of the pulse locations and passing through the other pulse position. These spectra are plotted as $\mathrm{d}^2I/\mathrm{d}V_s^2(d, V_s)$ for six values of V_g as shown in Figs 4.9c-h. For large values of V_g (-25V and -27V), there are two wells separated by a small bump. For larger values of V_g, the internal structure becomes more visible. There are fading parallel lines to the right of the envelope that encloses the nodal structure.

$\mathrm{d}I/\mathrm{d}V_s$ maps were obtained on a region that was pulsed with $\tilde{V}_g$=-40V at two locations separated by 200 nm, as shown in Fig. 4.10. The locations of the dots within the scan window is sketched in Fig. 4.9b. The maps show complex interference patterns inside Cassini oval-shaped regions. Outside, there are concentric, fading waves radiating away from these envelopes. Although the internal interference pattern may appear somewhat random, they consistently show two foci as well as straight vertical features in the middle.

We performed two STM tip voltage pulses with $\tilde{V}_g$=40V separated by 200 nm. We then obtained $\mathrm{d}I/\mathrm{d}V_s$ spectra along an axis passing through both pulse locations for various V_g. The results are plotted as $\mathrm{d}^2I/\mathrm{d}V_s^2(d, V_s)$ in Fig. 4.11d-k. For large values of V_g (30V and 32V), the interference patterns near pulse locations resemble the patterns for single quantum dots (with round lobes). For smaller values of V_g (18V to 26V), however, the internal structure evolves into patterns that appear more like parallel lines with kinks as opposed to a nodal structure.

The same voltage pulse procedure was performed on another area of graphene (two pulses with $\tilde{V}_g$=40V separated by 200 nm) and $\mathrm{d}I/\mathrm{d}V_s$ maps were obtained, as shown in Fig. 4.12. Similar to the $\mathrm{d}I/\mathrm{d}V_s$ maps in Fig. 4.10, there is an internal structure that shows nodal interference patterns and outside structure consisting of concentric Cassini ovals. Furthermore, the internal structure clearly display two foci as well as vertical lines in the middle, as was observe in Fig. 4.10.

Our spectroscopic observations on graphene with two STM tip voltage pulses separated by 200 nm may be understood as a system of strongly coupled quantum dots. As before, the dark envelopes in $\mathrm{d}^2I/\mathrm{d}V_s^2(d, V_s)$ plots (Figs 4.9 and 4.11) are Dirac points that separate

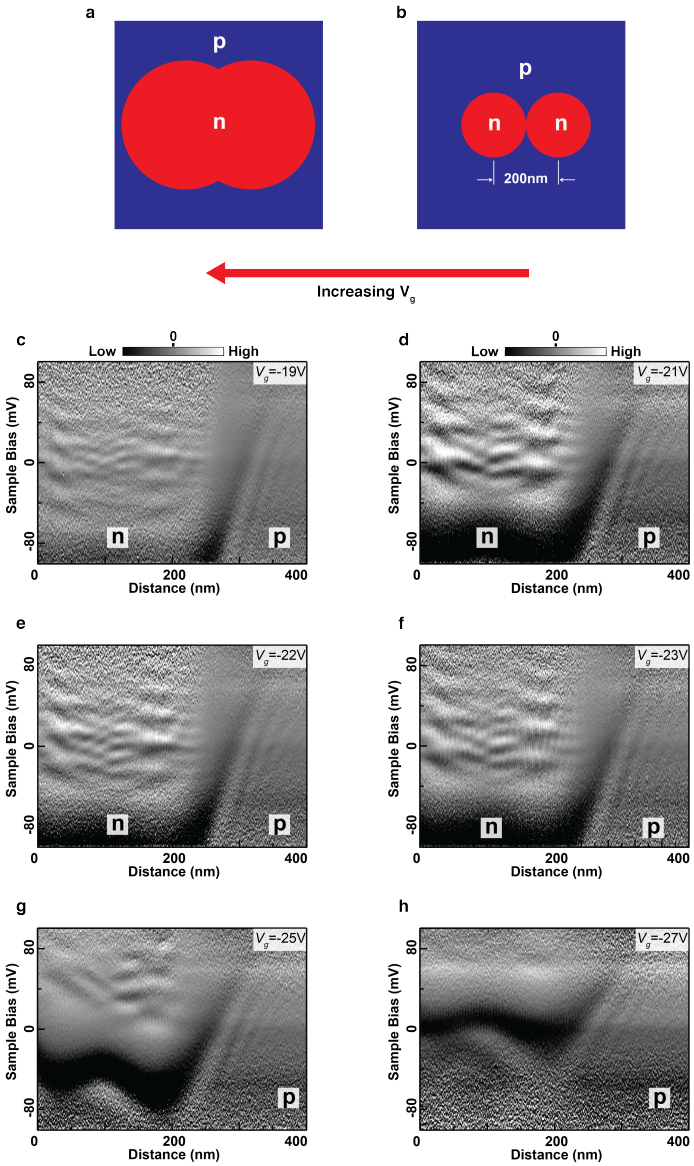

Figure 4.9: Electronic structure of Electron Quantum Dots in Graphene Separated by 200 nm. (a-c) Schematic indicating the location of the quantum dots. The two quantum dots were fabricated by locally n-doping graphene with STM tip pulses at $\tilde{V_g}$ =-40V, h_{lift}=1.8nm, V_s=5V, Δt=1 min. Distance d is defined as shown in (c), where d=0 nm is at the center of one quantum dot and the other quantum dot is located at d=200nm. (d-l) $\mathrm{d}^2I/\mathrm{d}V_s^2(d, V_s)$ at various backgate voltages V_g. Initial tunneling parameters for all $\mathrm{d}I/\mathrm{d}V_s$ spectra: V_s =-0.1V, I=1.5nA, $V_{a.c.}$= 1mV.

n-doped and p-doped regions of the graphene. These plots reveal that there is still a small tunnel barrier between the two dots (as bumps in Fig. 4.9 and dips in Fig. 4.11). Hence,

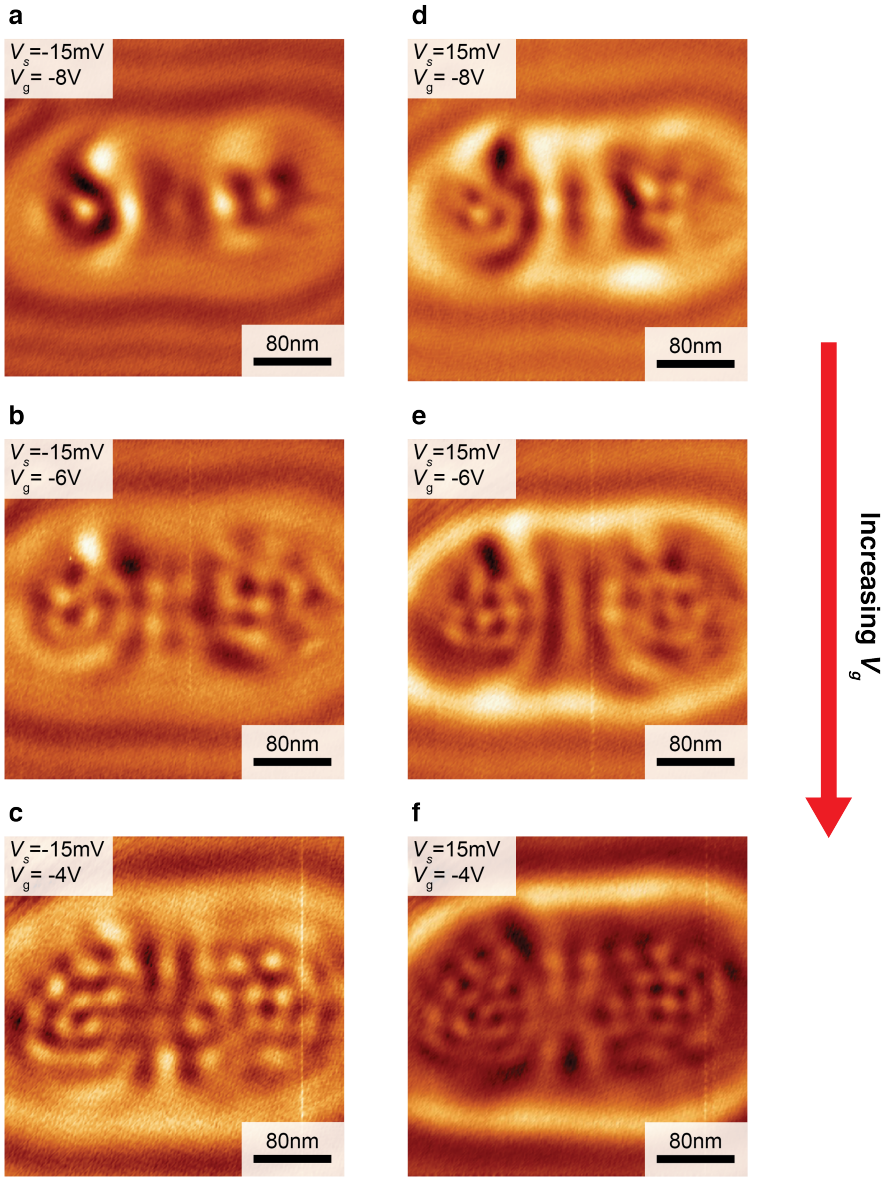

Figure 4.10: Interference Patterns of Electron Quantum Dots in Graphene Separated by 200 nm. (a-c) $\mathrm{d}I/\mathrm{d}V_s$ maps of electron quantum dots at various backgate voltages for sample bias V_s=-15mV. The two quantum dots were fabricated with STM tip pulses at $\tilde{V_g}$ =-40V, h_{lift}=2.0nm, V_s=5V, Δt=1 min . (d-f) $\mathrm{d}I/\mathrm{d}V_s$ maps acquired at various backgate voltages for sample bias V_s =15mV. As V_g increases, the quantum dot size increases. Tunneling parameters for all $\mathrm{d}I/\mathrm{d}V_s$ maps: I=50pA, $V_{a.c.}$ = 2mV.

these systems may be viewed as strongly coupled quantum double dots rather than a single quantum dot. Further theoretical investigation is necessary in order to understand the new features in $\mathrm{d}^2I/\mathrm{d}V_s^2(d, V_s)$ and $\mathrm{d}I/\mathrm{d}V_s$ maps that did not occur in previous spectroscopic

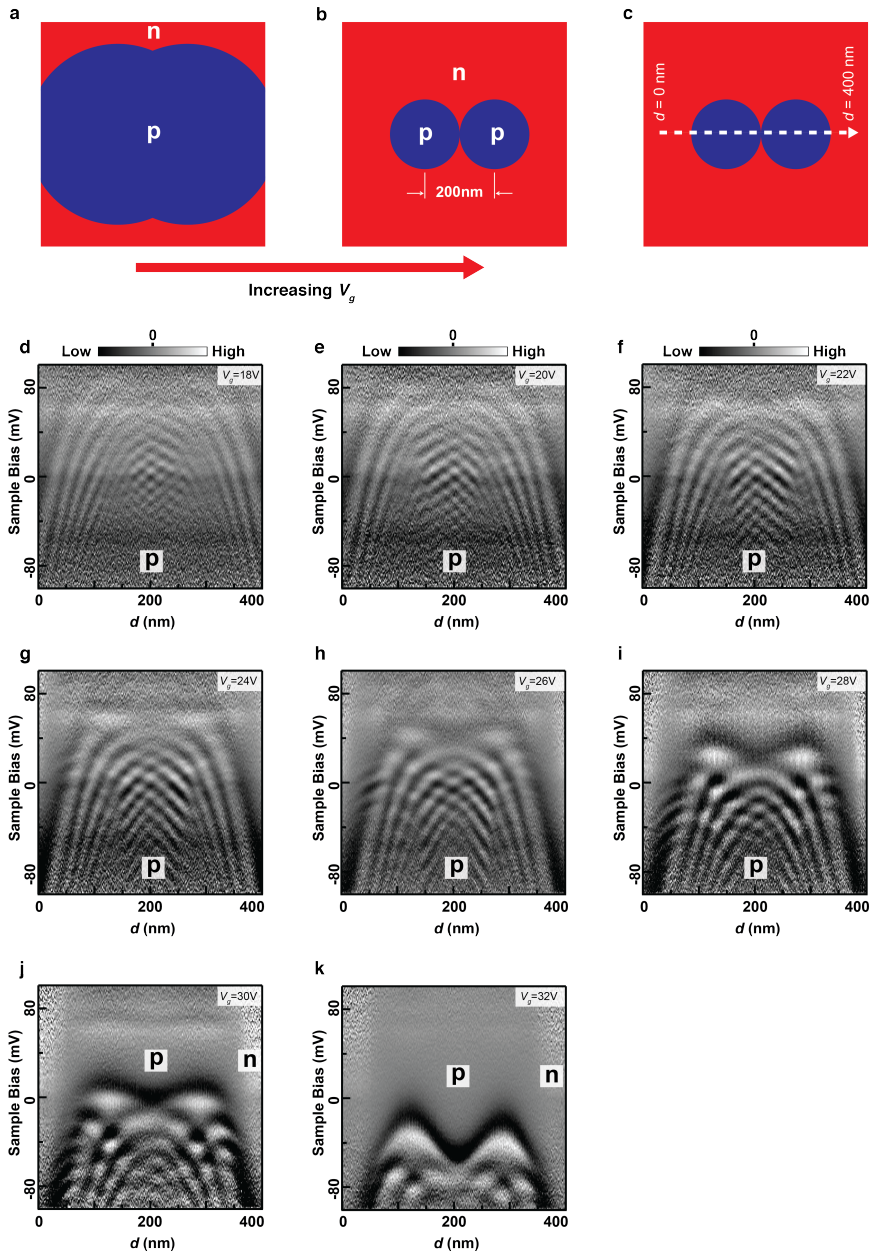

Figure 4.11: Electronic structure of Hole Quantum Dots in Graphene Separated by 200 nm. (a-c) Schematic indicating the location of the quantum dots. The two quantum dots were fabricated by locally p-doping graphene with STM tip pulses at $\tilde{V_g}$ =40V, h_{lift}=2.0nm, V_s=5V, Δt=1 min. Distance d is defined as shown in (c). (d-l) $\mathrm{d}^2I/\mathrm{d}V_s^2(d, V_s)$ at various backgate voltages V_g. Initial tunneling parameters for all $\mathrm{d}I/\mathrm{d}V_s$ spectra: V_s=-0.1V, I=1nA, $V_{a.c.}$= 1mV.

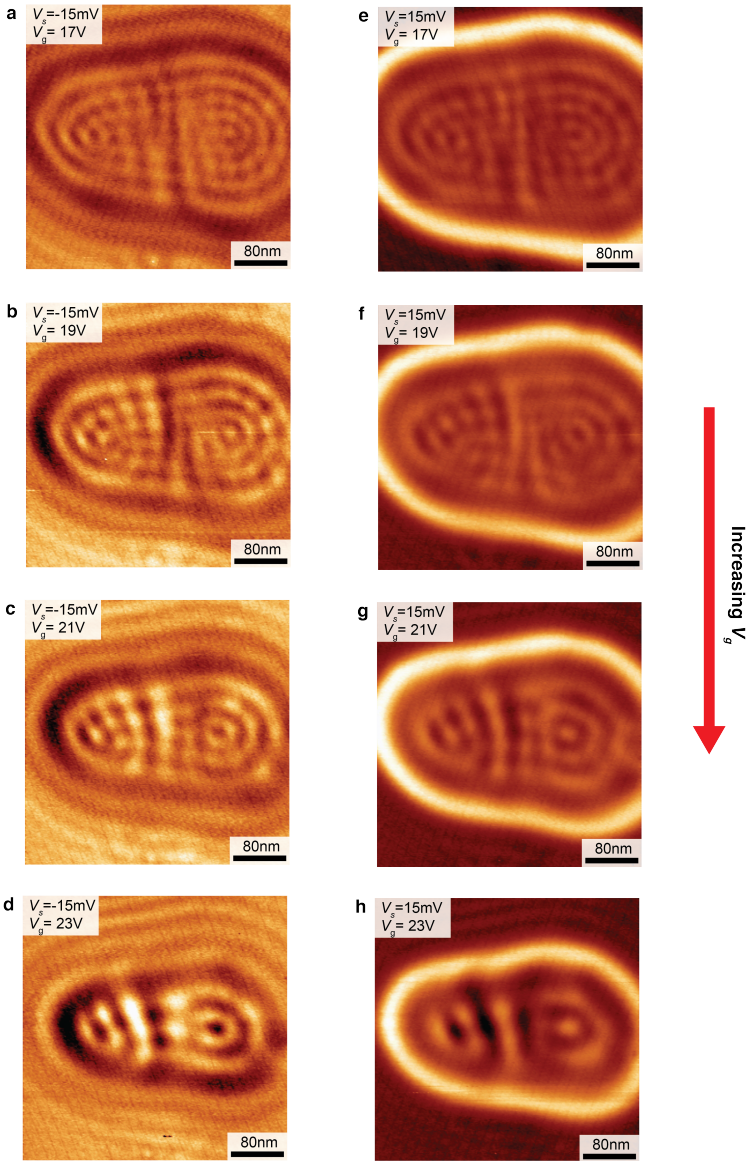

Figure 4.12: Interference Patterns of Hole Quantum Dots in Graphene Separated by 200 nm. (a-c) $\mathrm{d}I/\mathrm{d}V_s$ maps of electron quantum dots at various backgate voltages for sample bias V_s=-15mV. The two quantum dots were fabricated with STM tip pulses at $\tilde{V}_g$ =40V, h_{lift}=1.9nm, V_s=5V, Δt=1 min. (d-f) $\mathrm{d}I/\mathrm{d}V_s$ maps acquired at various backgate voltages for sample bias V_s=15mV. As V_g increases, the quantum dot size increases. Tunneling parameters for all $\mathrm{d}I/\mathrm{d}V_s$ maps: I=50pA, $V_{a.c.}$= 2mV.

measurements.

4.5 Quantum Dot Array

As shown in Fig. 4.13a, four STM tip voltage pulses were applied in an array. $\mathrm{d}I/\mathrm{d}V_s$ maps at various V_s and V_g are shown in Figs 4.13b-i. For V_g=-4V in Fig. 4.13b and f, there are four structures with approximately circular interference patterns. As V_g is lowered, the interference pattern inside circular structures become simplified and more nodes appear between the four circles.

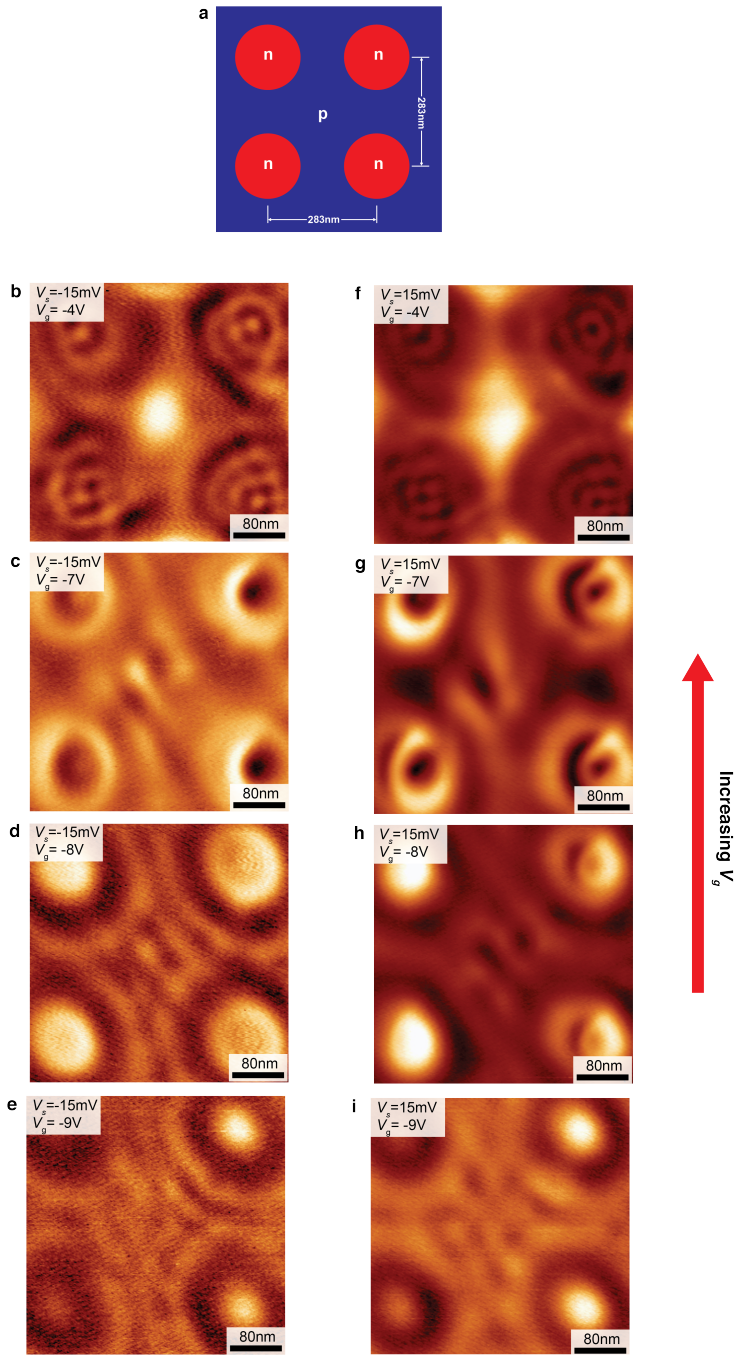

Figure 4.13: Quantum Interference in an Array of Electron Quantum Dots. (a) Schematic of an array of circular p-n junctions created by four STM tip pulses at $\tilde{V_g}$ =-40V, h_{lift}=1.9nm, V_s=5V, Δt=1 min. (b-e) dI/dV_s maps of the array of quantum dots at various backgate voltages for sample bias V_s=-15mV. (f-i) dI/dV_s maps acquired at various backgate voltages for sample bias V_s=15mV. As V_g increases, the quantum dot size increases. Tunneling parameters for all dI/dV_s maps: I=50 pA, $V_{a.c.}$= 2mV.

Fig. 4.14 shows a region of graphene where an array of four pulses were applied. dI/dV_s at various V_s and V_g are shown in Figs 4.14b-i. dI/dV_s maps at V_g=9V reveal interference patterns with four focal points around the locations of the voltage pulses. As V_g increases, circular interference patterns around pulse locations become more prominent in dI/dV_s maps. At V_g=18V, the circular peaks around pulse locations appear to be distinct and well separated

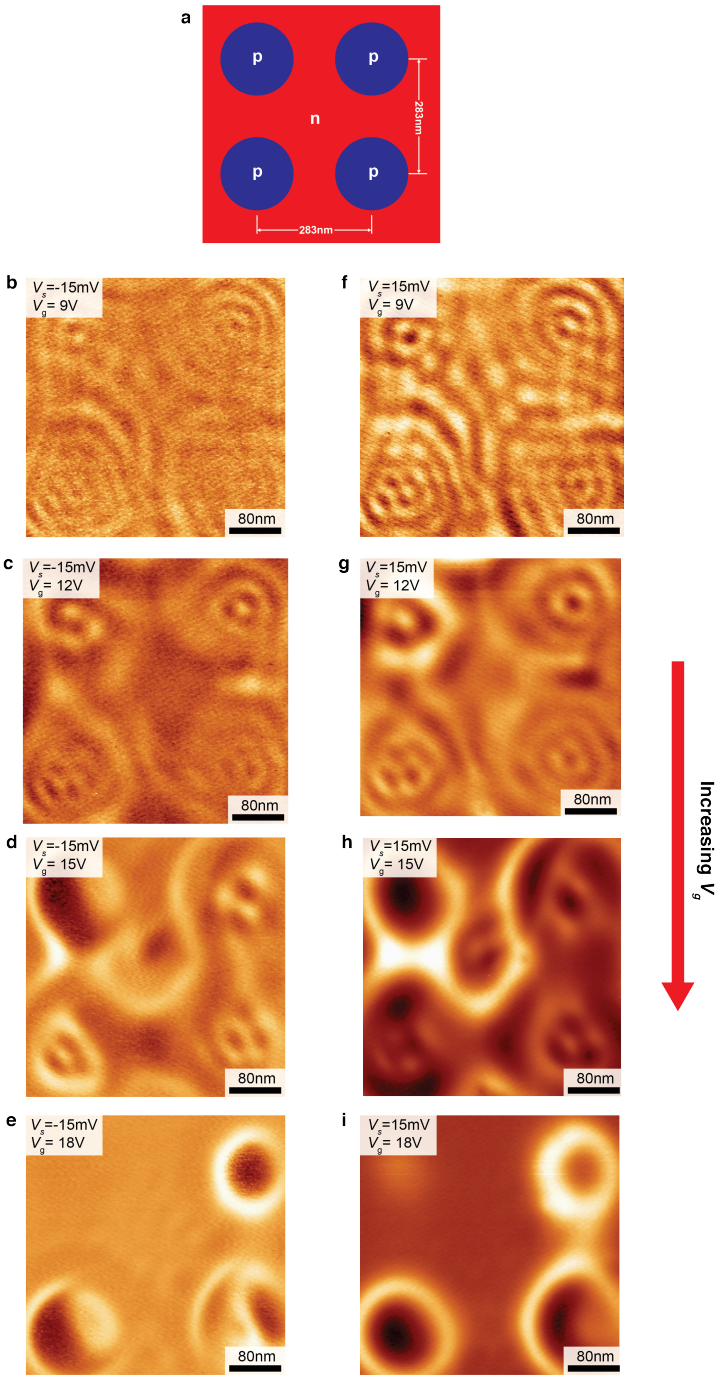

Figure 4.14: Quantum Interference in an Array of Hole Quantum Dots. a. Schematic of an array of circular p-n junctions created by four STM tip pulses at $\tilde{V}_g$ =40V, h_{lift}=1.9nm, V_s=5V, Δt=1 min. (b-e) dI/dV_s maps of the array of quantum dots at various backgate voltages for sample bias V_s=-15mV. (f-i) dI/dV_s maps acquired at various backgate voltages for sample bias V_s=15mV. As V_g increases, the quantum dot size decreases. Tunneling parameters for all dI/dV_s maps: I=50 pA, $V_{a.c.}$= 2mV.

from each other.

These experimental data show that it is possible to create more complex systems of multiple quantum dots by engineering local embedded gates via STM tip voltage pulse procedure. This provides a platform for exploring many other physical phenomena, such as the creation of massless Dirac fermions with anisotropic group velocity in the presence of

periodic potentials[76].

Chapter 5

Quantum Dots with Non-Circular Geometry

In this chapter, we report on the use of STM to fabricate and characterize non-circular p-n junctions in monolayer graphene. By examining elliptical and stadium-shaped graphene p-n junctions, we probe the role of Klein tunneling in charge carrier confinement and explore the possibility of quantum chaos.

In Section 5.2, we fabricate non-circular, ellipse-like graphene p-n junctions by performing STM tip voltage pulses at two locations separated by 100 nm. The electronic structure of these structures are spatially mapped by STS.

In Section 5.3, we create stadium-shaped graphene p-n junctions by applying STM tip voltage pulses at three colinear positions with 100 nm separation between adjacent pulses. The resulting electronic structure is characterized by spatially resolved STS.

5.1 Introduction

About two and a half decades ago, Crommie *et al.* demonstrated nanoscale confinement of electrons on metal surface by STM manipulation of adatoms to form a circular 'quantum corral'[71]. This pioneering work was followed by other interesting experiments, such as the observation of quantum mirages in elliptical corrals [77] and the study of electron waves in stadium-shaped quantum corrals[78]. In particular, stadium-shaped electron resonators have long attracted much theoretical [79–81] and experimental [4, 82–84] investigation because of their potential to exhibit quantum chaos. Having examined circular p-n junctions in previous chapters, we now follow the the path of quantum corral research and investigate elliptical and stadium-shaped graphene p-n junctions. In this chapter, we present our preliminary experimental results on these structures, which provide additional insight into the anisotropic behavior of Klein tunneling.

5.2 Elliptical Graphene P-N Junctions

We performed STM tip voltage pulse procedure sequentially at two different locations separated by a distance of 100 nm while holding the backgate at $\tilde{V}_g$=-40V with tip-pulse parameters h_{lift} =1.8nm, V_s=5V, and Δt=1 min. We then measured $\mathrm{d}I/\mathrm{d}V_s$ spectra at various distances along an axis passing through the two pulse locations, as depicted in Fig. 5.1c. The results are plotted as $\mathrm{d}^2I/\mathrm{d}V_s^2(d, V_s)$ for various V_g in Figs 5.1d-i. There is a dark U-shaped feature that divides the interference patterns into two groups. Inside the U-shaped envelope, a nodal structure is present. Outside, fainter lines appear parallel to the dark U-shaped structure.

Similar to Fig. 5.1, STM tip voltage pulses were applied 100 nm apart but while holding the backgate at $\tilde{V}_g$=40V. The resulting structure was probed by distance-dependent $\mathrm{d}I/\mathrm{d}V_s$ spectroscopy and plotted in Figs 5.2d-i as $\mathrm{d}^2I/\mathrm{d}V_s^2(d, V_s)$. Intricate nodal patterns appear in these plots under dome-like shapes. As V_g is increased, the interference pattern shifts down in V_s until it disappears at V_g = 39V.

Our spectroscopic measurements on graphene with two STM tip voltage pulses separated by 100 nm provide information on the electronic structure of ellipse-like graphene p-n junction. Unlike coupled quantum double dots discussed in Chapter 4, the confinement potential (which shows up as dark envelopes in $\mathrm{d}^2I/\mathrm{d}V_s^2(d, V_s)$ plots) for these structures do not have tunnel barriers between them. Hence, these structures may be appropriately considered single quantum dots. $\mathrm{d}^2I/\mathrm{d}V_s^2(d, V_s)$ plots in Figs 5.1 and 5.2 show features similar to those observed in circular p-n junctions, such as an internal nodal pattern denoting confined eigenstates and external Friedel-like oscillations. A notable difference in these ellipse-like structures is that distance-dependent $\mathrm{d}I/\mathrm{d}V_s$ spectra look extremely different for p-doped structures (Fig. 5.2) than for the n-doped structures (Fig. 5.1). Further investigation is required to understand the origin of this difference.

5.3 Stadium Graphene P-N Junctions

STM tip voltage pulses were applied sequentially at three colinear positions with 100 nm separation between adjacent pulse locations. The tip-pulse parameters were $\tilde{V}_g$ =40V, h_{lift}=2nm, V_s=5V, and Δt=1 min. As sketched in Fig. 5.3c, $\mathrm{d}I/\mathrm{d}V_s$ spectra were measured along an axis passing through through the pulse locations. Figs. 5.3d-i show $\mathrm{d}^2I/\mathrm{d}V_s^2(d, V_s)$ plots for various V_g. A nodal pattern appears inside a dome-like structure in each $\mathrm{d}^2I/\mathrm{d}V_s^2(d, V_s)$ plot. Notably, there are sharp kinks in the interference structure at the middle of the interference patterns.

$\mathrm{d}I/\mathrm{d}V_s$ maps were obtained on an area graphene where three colinear STM tip voltage pulses were applied (same configuration as in Fig. 5.3 but on a different region of graphene and with a different STM tip), as shown in Fig. 5.4. Each map shows that there are nodal interference patterns with two foci inside a stadium-like boundary. Notably, there are vertical lines (both bright and dark) near the middle of the stadium structure that appear more

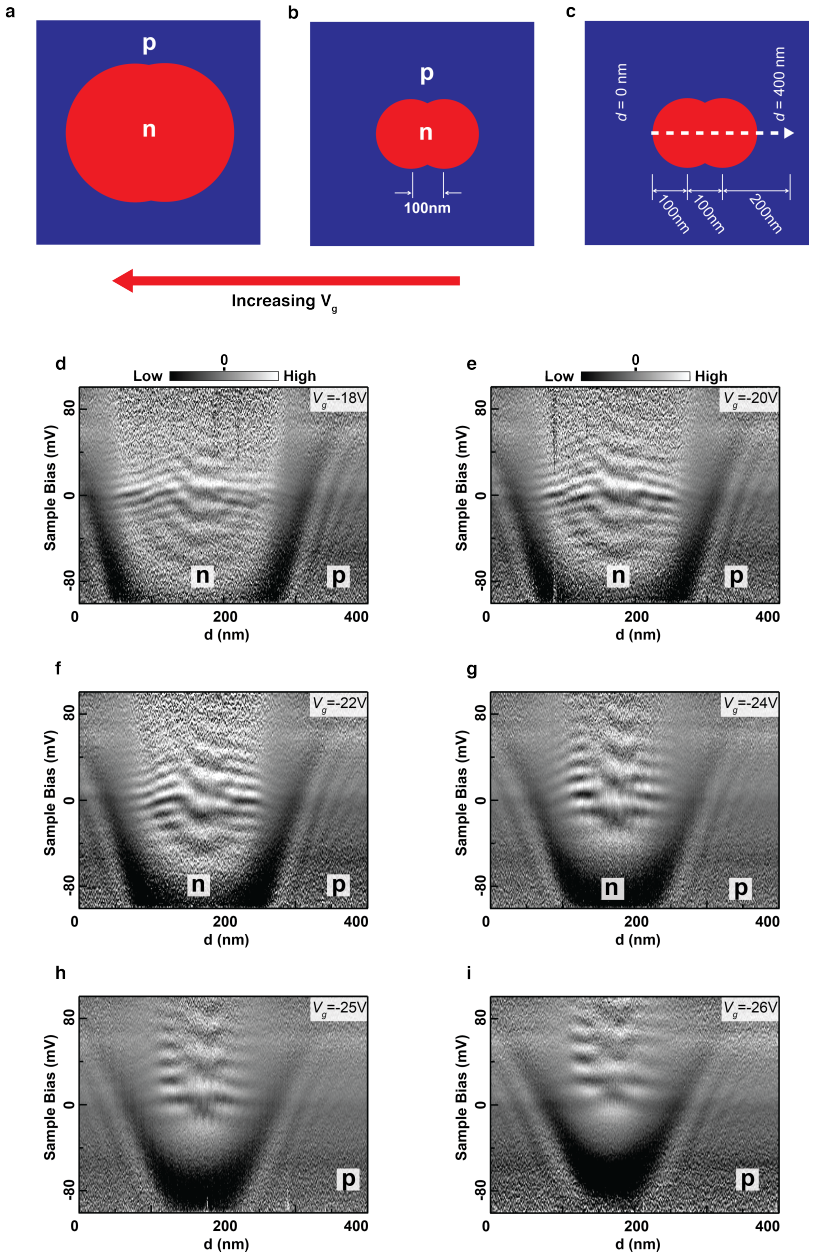

Figure 5.1: Electronic Structure of an Electron Quantum Dot in Graphene with Elliptical Geometry. (a-c) Schematic indicating the location of STM tip pulses. The two quantum dots were fabricated by locally n-doping graphene with two STM tip pulses separated by 100 nm at $\tilde{V_g}$ =-40V, h_{lift} =1.8nm, V_s=5V, Δt=1 min. Distance d is defined as shown in (c). (d-i) $\mathrm{d}^2I/\mathrm{d}V_s^2(d, V_s)$ at various backgate voltages V_g. Initial tunneling parameters for all $\mathrm{d}I/\mathrm{d}V_s$ spectra: V_s=-0.1V, I=1.5nA, $V_{a.c.}$ = 1mV.

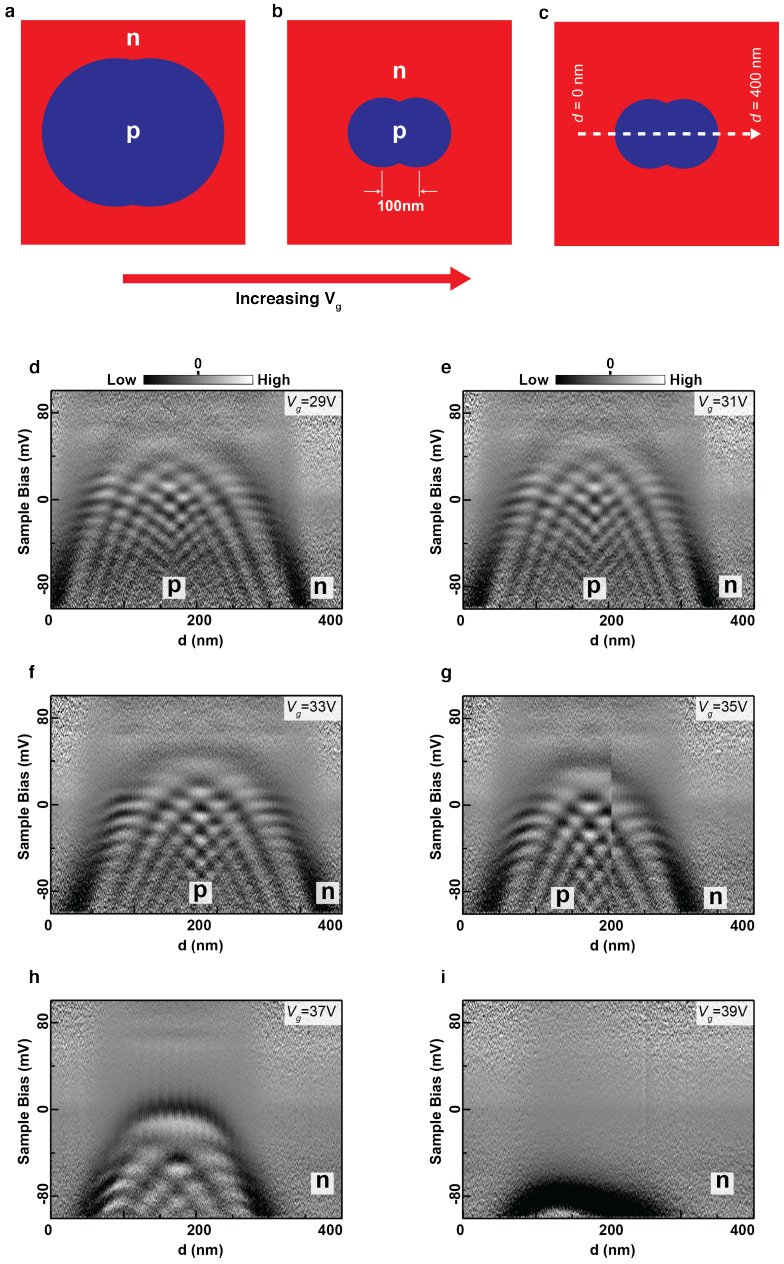

Figure 5.2: Electronic Structure of a Hole Quantum Dot in Graphene with Elliptical Geometry. (a-c) Schematic indicating the location of STM tip pulses. The two quantum dots were fabricated by locally p-doping graphene with two STM tip pulses separated by 100 nm at $\tilde{V_g}$ =40V, h_{lift}=2nm, V_s=5V, Δt=1 min. Distance d is defined as shown in (c). (d-i) $\mathrm{d}^2I/\mathrm{d}V_s^2(d, V_s)$ at various backgate voltages V_g. Initial tunneling parameters for all $\mathrm{d}I/\mathrm{d}V_s$ spectra: V_s=-0.1V, I=1nA, $V_{a.c.}$= 1mV.

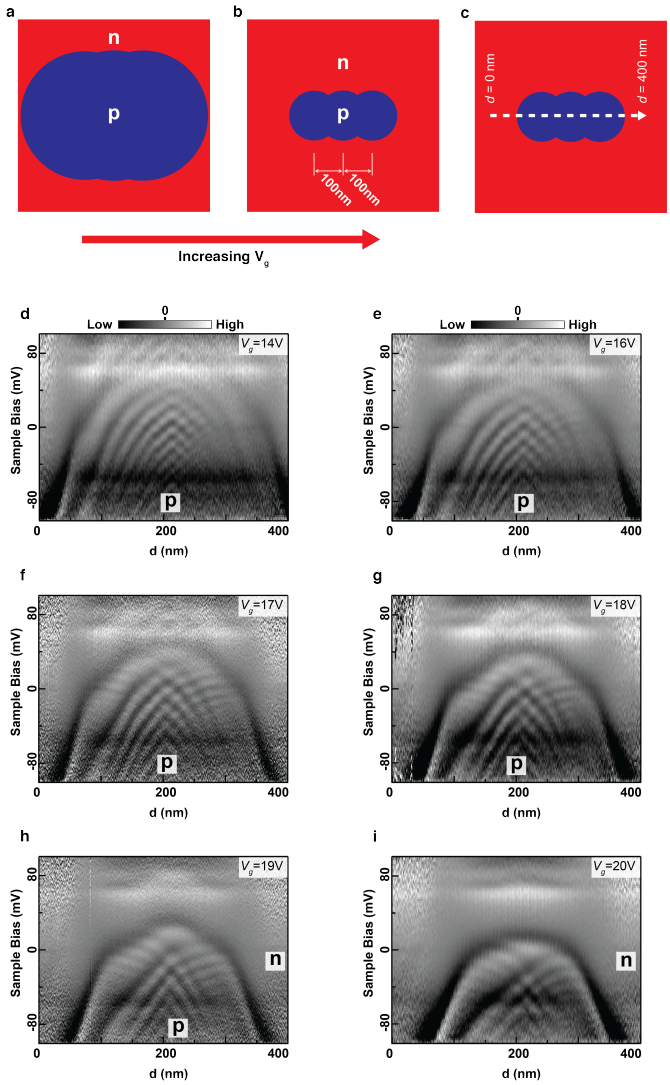

Figure 5.3: Electronic Structure of a Hole Quantum Dot in Graphene with Stadium Geometry. (a-c) Schematic indicating the location of STM tip pulses and geometry of resulting p-n junction cavity. A hole quantum dot was fabricated by locally p-doping graphene with three colinear STM tip pulses separated by 100 nm at $\tilde{V_g}$ =40V, h_{lift}=2nm, V_s=5V, Δt=1 min. Distance d is defined as shown in (c), where the three STM pulses were applied at d=100 nm, 200nm, and 300 nm. (d-i) $\mathrm{d}^2I/\mathrm{d}V_s^2(d, V_s)$ at various backgate voltages V_g. Initial tunneling parameters for all $\mathrm{d}I/\mathrm{d}V_s$ spectra: V_s =-0.1V, I=1nA, $V_{a.c.}$= 2mV.

prominently than others in each $\mathrm{d}I/\mathrm{d}V_s$ map. As V_g is increased, the size of the stadium-like cavity decreases and the number of nodes decreases.

Quantum confinement within resonators that have non-integrable, classically chaotic orbits produces quantum scars[4, 79–84]. In graphene, signatures of quantum chaos were

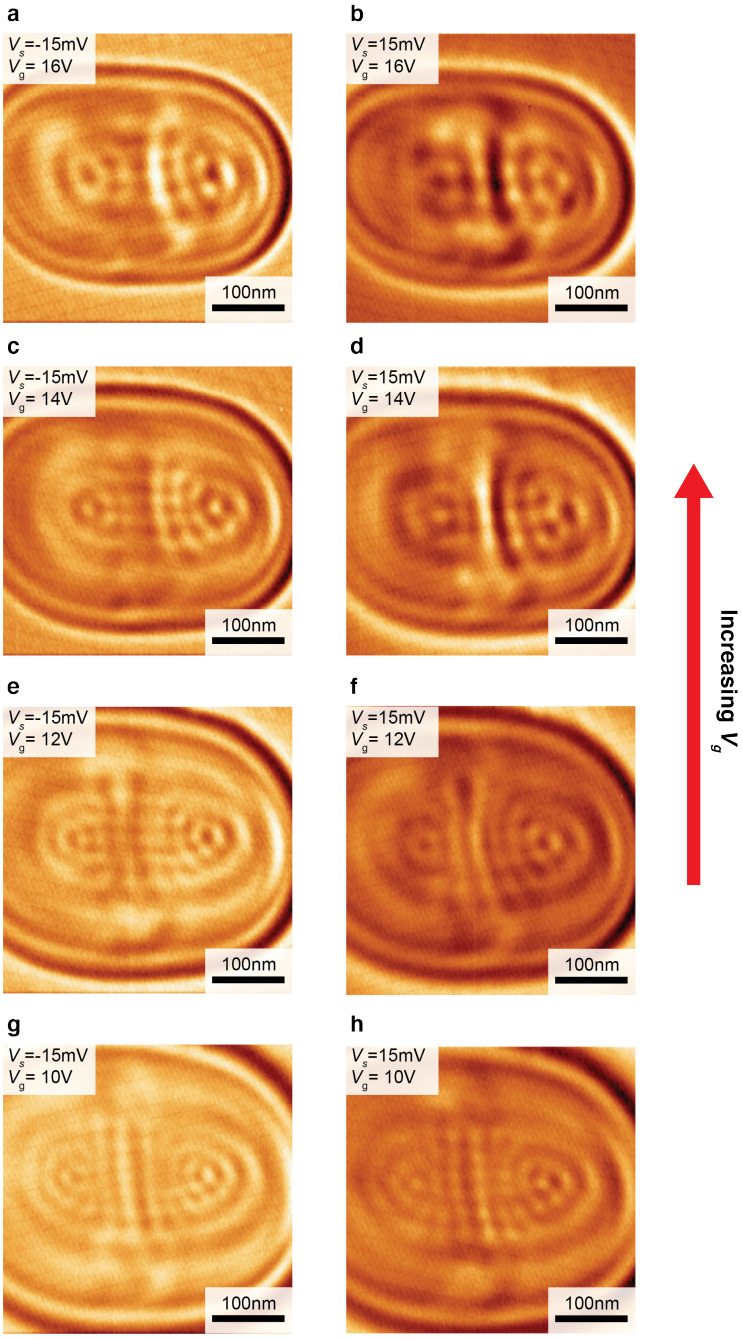

Figure 5.4: Graphene quantum dot with stadium geometry. (a-h) $\mathrm{d}I/\mathrm{d}V_s$ maps on a quantum dot that was fabricated with three co-linear STM tip pulses separated by 100 nm at $\tilde{V}_g$ =40V, h_{lift}=2.3nm, V_s=5V, Δt=1 min. Tunneling parameters for all $\mathrm{d}I/\mathrm{d}V_s$ maps: I=50 pA, $V_{a.c.}$= 2mV.

detected in transport measurements[4], but direct visualization of scarred wavefunctions has not yet been achieved.

$\mathrm{d}^2I/\mathrm{d}V_s^2(d, V_s)$ plots in Fig. 5.3 and $\mathrm{d}I/\mathrm{d}V_s$ maps in Fig. 5.4 provide preliminary experimental attempts towards imaging scarred Dirac fermion wavefunctions. However, there is no obvious similarity between these interference patterns and those predicted for scarred Schrodinger electrons predicted in Ref [79]. In the case of stadium-shaped quantum corrals,

the confinement potential was too 'leaky' to observe effects of quantum chaos[78]. In the case of stadium-shaped graphene p-n junctions, further theoretical and experimental investigations are required to determine whether Klein tunneling allows enough reflectance to produce scarred wavefunctions.

We now provide a qualitative explanation for a commonly appearing feature in Fig. 5.4. Within the stadium-shaped structures shown in these $\mathrm{d}I/\mathrm{d}V_s$ maps, there are bright or dark vertical lines that appear prominently. This may be understood as a consequence of the anisotropic transmission coefficient. Due to Klein tunneling, there is minimal reflection at low angles of incidence on the straight parts of the stadium-shaped p-n junction. This should produce weak confinement of quasiparticles in the vertical direction, which would reduce nodes, or horizontal lines, in the middle of the stadium structure and produce the vertical lines shown in our $\mathrm{d}I/\mathrm{d}V_s$ maps.

Chapter 6

Bilayer Graphene Quantum Dots

In this chapter we report on our STM fabrication and characterization of bilayer graphene quantum dots. We first demonstrate that the technique we used for patterning embedded gates in monolayer graphene/hBN heterostructures in previous chapters can be extended to bilayer graphene/hBN heterostructures. By detecting Coulomb oscillations in differential conductance spectroscopy, we demonstrate a gate-tunable evolution of locally gated bilayer graphene from classical dots to quantum dots. Spatially resolved scanning tunneling spectroscopy of quantum double dots in bilayer graphene reveal important information about the charge carrier confinement mechanism in bilayer graphene quantum dots.

In Section 6.2, we demonstrate that the technique for engineering local embedded gates for graphene/hBN heterostructures described in Chapter 2 is robust and can be effectively applied to bilayer graphene/hBN heterostructures. Using STS, we detect shifts in the local charge neutrality point of the bilayer graphene and confirm that our fabricated hBN gates locally dope the overlaid bilayer graphene.

In Section 6.3, we perform scanning tunneling spectroscopy on locally gated bilayer graphene in order to explore its electronic structure and discover sharp, gate-tunable peaks in $\mathrm{d}I/\mathrm{d}V_s$ spectra. Spatially resolved STS on these structures reveals concentric rings whose spatial and energy density is determined by the applied backgate. We provide a qualitative explanation of our experimental observations by modeling our system as an asymmetric double-barrier quantum well. In this framework, the peaks observed in our spectroscopic measurements are Coulomb staircase resonances.

In Section 6.4, we fabricate and investigate bilayer graphene circular p-n junctions whose polarity is opposite of the quantum dots discussed in Section 6.3 (Here, n-doped quantum dots are explored as opposed to p-doped quantum dots). Due to the difference in polarity, more complicated Coulomb staircase structures are observed in our spatially resolved STS measurements. This provides additional insight into the confinement mechanism of these bilayer graphene quantum dots.

In Section 6.5, we provide evidence for four-fold degeneracy in quantum dot energy levels due to spin and valley symmetries.

In Section 6.6, we fabricate coupled quantum dots separated by 200 nm and provide STS

characterization of their electronic structures. Complex Coulomb oscillations are observed in spatially resolved $\mathrm{d}I/\mathrm{d}V_s$ spectra and $\mathrm{d}I/\mathrm{d}V_s$ maps, which provide further information on the electronic structure of bilayer graphene quantum dots.

In Section 6.7, we present preliminary experimental results on fabricating steeper confinement potentials in bilayer graphene by adjusting STM tip voltage pulse parameters. Bilayer graphene quantum dots created by this method suggest a unique electronic structure, inviting future experimental and theoretical investigations.

6.1 Introduction

Bilayer graphene's charge carriers are massive Dirac fermions with distinct properties in the vicinity of p-n junctions[2, 3]. As was the case for massless Dirac fermions in monolayer graphene, several unique phenomena are predicted for bilayer graphene p-n junctions, such as anti-Klein tunneling[3], common-path interference and Zener tunneling[85], and electron cloaked states[21]. Previously, transport experiments reported macroscopic characterization of p-n junction-related phenomena in bilayer graphene[22, 86]. However, microscopic characterization of p-n junctions in bilayer graphene is still largely lacking. In this chapter, we present our local, spatial characterization of circular p-n junctions in bilayer graphene using STM.

6.2 Local Doping of Bilayer Graphene using STM

As depicted in Fig. 6.1a, our experimental setup consists of a Bernal stacked bilayer graphene/ hexagonal boron nitride (hBN) heterostructure placed on SiO_2/silicon wafer. The circuit is identical to Figure 2.1 in Section 2.2. The bilayer graphene is electrically grounded and the STM tip has a bias voltage $-V_s$, while a backgate voltage V_g is applied to the heavily doped silicon. To create an embedded gate, the STM tip is placed a few nanometers above the bilayer graphene and a voltage pulse is applied while the backgate is held at some $\tilde{V}_g$. Here we use $\tilde{V}_g$ to denote the backgate voltage sustained while an STM tip voltage-pulse is applied above the bilayer graphene/hBN heterostructure. This backgate voltage is different from the backgate voltage applied during a spectroscopic measurement, which is denoted by V_g. The end result of this process is a buildup of space charge within the hBN and below the location of the STM tip voltage pulse, which acts as a local embedded gate below the bilayer graphene flake, as shown in the inset of Fig. 6.1a.

To observe the effect of STM tip-voltage pulse on the electronic structure of bilayer graphene, $\mathrm{d}I/\mathrm{d}V_s$ spectra were measured at $V_g = 0$V on the location of the tip pulse after the tip pulse procedure was performed at various values of $\tilde{V}_g$, as shown in Fig. 6.1b. Each spectrum displays a gap-like feature at $V_s = 0$V, which comes from phonon-assisted inelastic tunneling, as was observed previous scanning tunneling spectroscopy (STS) studies on graphene [49, 87]. Additionally, there is a smaller dip in the spectra corresponding to the

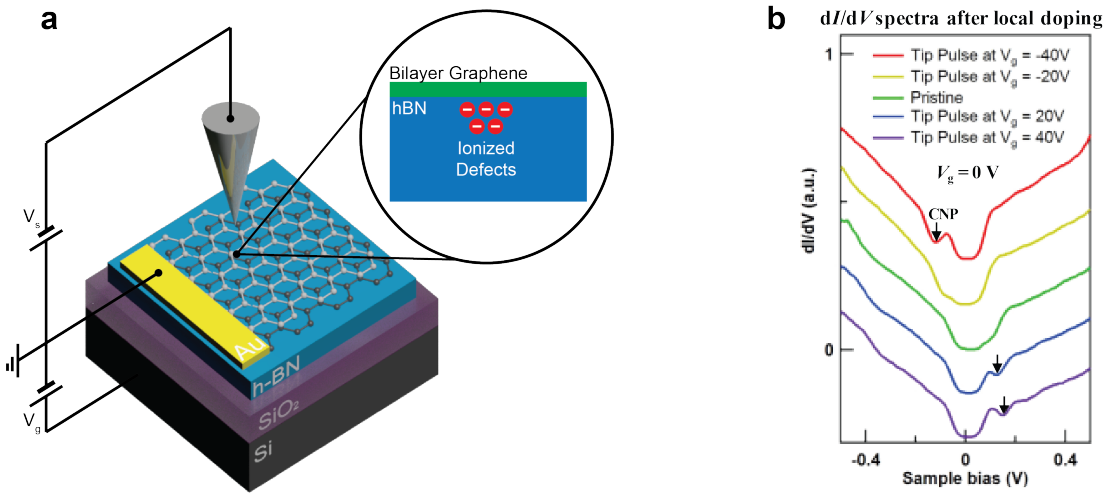

Figure 6.1: Local doping of bilayer graphene. (a) Schematic for using a scanning tunneling microscope (STM) to locally dope a Bernal stacked bilayer graphene/hexagonal boron nitride (hBN) heterostructure placed on silicon dioxide/silicon wafer. A voltage pulse is applied to an STM tip positioned a few nanometers above the graphene surface while the silicon backgate sustains a voltage $\tilde{V}_g$. Inset: STM tip voltage pulse ionizes defects within the hBN, resulting in a buildup of space charge that acts as a local embedded gate on the graphene. (b) $\mathrm{d}I/\mathrm{d}V_s$ spectra showing shifts in the graphene's charge neutrality point (CNP) due to local doping. Each $\mathrm{d}I/\mathrm{d}V_s$ curve was obtained with the backgate held at $V_g = 0$V. The gap-like feature occurring at V_s=0V in every $\mathrm{d}I/\mathrm{d}V_s$ spectrum is a phonon-induced pseudogap characteristic of STS on graphene. Initial tunneling parameters: V_s= 0.5 V, I=0.5nA, $V_{a.c.}$=5mV.

charge neutrality point (CNP) of the bilayer graphene. This feature is indicated by black arrows in Fig. 6.1b. When the CNP is above (below) $V_s = 0$V, the Fermi level of bilayer graphene is below (above) the CNP, meaning that the bilayer graphene is locally p-doped (n-doped). A clear trend in Fig. 6.1b is that a positive (negative) $\tilde{V}_g$ results in the shifting of the CNP to the right (left) with the magnitude of shift determined by the value of $\tilde{V}_g$. These observations are consistent with previous experiments where the same tip-pulse procedure was used for monolayer graphene/hBN heterostructures, where positive (negative) backgate voltages $\tilde{V}_g$ produced negative (positive) embedded gates that p-doped (n-doped) the monolayer graphene [18, 66]. Furthermore this doping can be removed by applying a tip pulse at $\tilde{V}_g$=0V, which restores the bilayer graphene to its pristine condition (represented by the green curve in Fig. 6.1b).

6.3 Charging Resonances in Scanning Tunneling Spectroscopy of Bilayer Graphene Quantum Dots

In order to investigate the electronic structure of the tip voltage-pulsed bilayer graphene, we performed a tip pulse at $\tilde{V_g}$=40V and then measured $\mathrm{d}I/\mathrm{d}V_s$ spectra at the same location of the tip pulse for a range of backgate voltages V_g. These data are shown in Fig. 6.2a, where $\mathrm{d}I/\mathrm{d}V_s$ is plotted as a function of V_s and V_g. A dark horizontal band appears around V_s=0V, which is the phonon-induced pseudogap present in all of our $\mathrm{d}I/\mathrm{d}V_s$ spectra on bilayer graphene. Another prominent feature in this plot is a set of bright lines, which are local maxima in $\mathrm{d}I/\mathrm{d}V_s$ spectra that shift in energy as a function of V_g. Four such lines of similar widths appear near the middle of the plot, as well as numerous lines of smaller widths on the left. To highlight these features, we took a numerical derivative of Fig. 6.2a to obtain $\mathrm{d}^2I/\mathrm{d}V_s^2(V_s, V_g)$, (see Fig. 6.2b). In this plot the local maxima can be seen more clearly along with the phonon-related feature appearing as red and blue horizontal lines around V_s=0V. Furthermore, Fig. 6.2c shows $\mathrm{d}I/\mathrm{d}V_s$ spectra corresponding to line cuts at several values of V_g marked by colored dashed lines in Fig. 6.2a. Sharp peaks appear in $\mathrm{d}I/\mathrm{d}V_s$ spectra when V_g is approximately between V_g = 46V and V_g = 52V, but are absent when V_g is greater or smaller than those values.

We can further explore the electronic structure of locally doped bilayer graphene by using spatially resolved STS. Fig. 6.3a and b show $\mathrm{d}I/\mathrm{d}V_s$ maps with two different V_g on the same area of bilayer graphene that was locally p-doped (the STM tip pulse procedure was used here with $\tilde{V_g}$=40V as in Fig. 6.2 but on a different location of the sample). Multiple bright circular rings appear in both $\mathrm{d}I/\mathrm{d}V_s$ maps. As the backgate is lowered from V_g = 44V to V_g = 42V, the number of rings and the spatial density of resonances both increase. Since the local doping has approximate circular symmetry, we arbitrarily selected an axis passing through the center and measured $\mathrm{d}I/\mathrm{d}V_s$ at various distances from the center. Figs 6.3c and 6.3d show $\mathrm{d}^2I/\mathrm{d}V_s^2(V_s, x)$ plots obtained on the same region and V_g as Figs 6.3a and 6.3b, respectively. As was observed in Fig. 6.2b, red and blue horizontal lines appear near V_s=0V. Additionally, there are multiple resonances in $\mathrm{d}I/\mathrm{d}V_s$ spectra that shift up together in energy as function of $|x|$, forming parabola-like patterns in the $\mathrm{d}^2I/\mathrm{d}V_s^2(V_s, x)$ plots. As V_g is decreased from Fig. 6.3c to 6.3d, the number of resonances increases while the energy spacing between the resonances decreases.

Our experimental data can be understood by modelling our system as a double-barrier quantum well [88]. Due to the unique behavior of massive Dirac fermions in the presence of an electrostatic potential, circular p-n junctions in bilayer graphene can form quantum dots with unique energy spectra and confinement strengths [36, 37]. Figs 6.2 d-g illustrates how a negative local embedded gate in our experiment can produce circular p-n junctions of variable diameter. When V_g is sufficiently high, the graphene is completely n-doped, as shown in Fig. 6.2d. As V_g is decreased, however, the graphene becomes less n-doped until the gated region of graphene turns p-doped. Because our local embedded gate is approximately circular, this results in a circular p-n junction, as shown in Fig. 6.2e. As

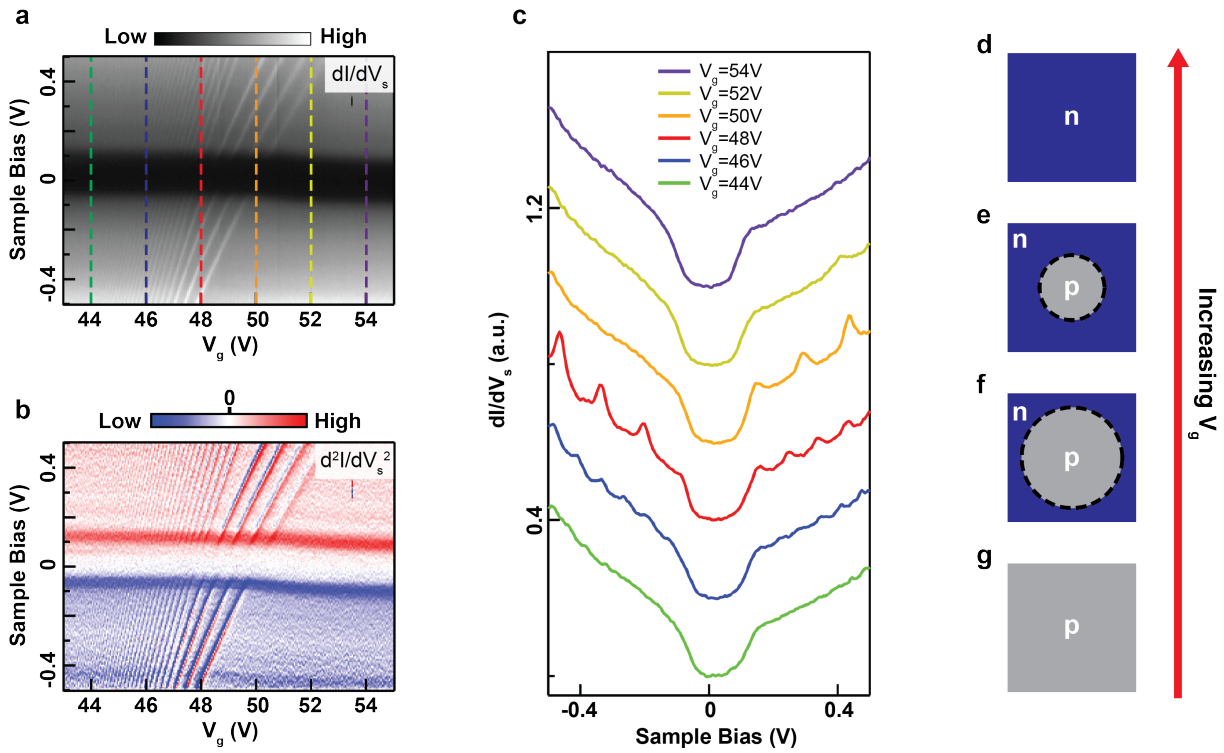

Figure 6.2: Scanning tunneling spectroscopy (STS) of locally gated bilayer graphene. (a) $\mathrm{d}I/\mathrm{d}V_s(V_s, V_g)$ plot consisting of $\mathrm{d}I/\mathrm{d}V_s$ spectra measured at the location of bilayer graphene where an STM tip voltage pulse was applied with $\tilde{V}_g$=40V. The bright lines forming a fan-like structure are peaks in $\mathrm{d}I/\mathrm{d}V_s$ spectra that shift in energy as a function of V_g. (b) $\mathrm{d}^2I/\mathrm{d}V_s^2(V_s, V_g)$ produced by numerically differentiating (a) in order to accentuate the resonances in $\mathrm{d}I/\mathrm{d}V_s$. (c) $\mathrm{d}I/\mathrm{d}V_s$ spectra corresponding to line cuts at several values of V_g indicated by colored dashed lines in (a). Each spectrum is offset for clarity. (d-g) Schematics illustrating how the backgate can be used to tune a circular p-n junction in bilayer graphene. (g) is a depiction of locally p-doped bilayer graphene. Increasing V_g n-dopes the graphene globally and gradually reduces the area that is p-doped, as shown in (f) and (e). For sufficiently large values of V_g, the graphene will be completely n-doped, as shown in (d). Initial tunneling parameters for all $\mathrm{d}I/\mathrm{d}V_s$ spectra: V_s= 0.5 V, I=0.5nA, $V_{a.c.}$=5mV.

V_g is decreased further, the p-doped region continues to expand (Fig. 6.2f) and eventually becomes completely p-doped. Backgate dependence of the diameter is further elucidated by

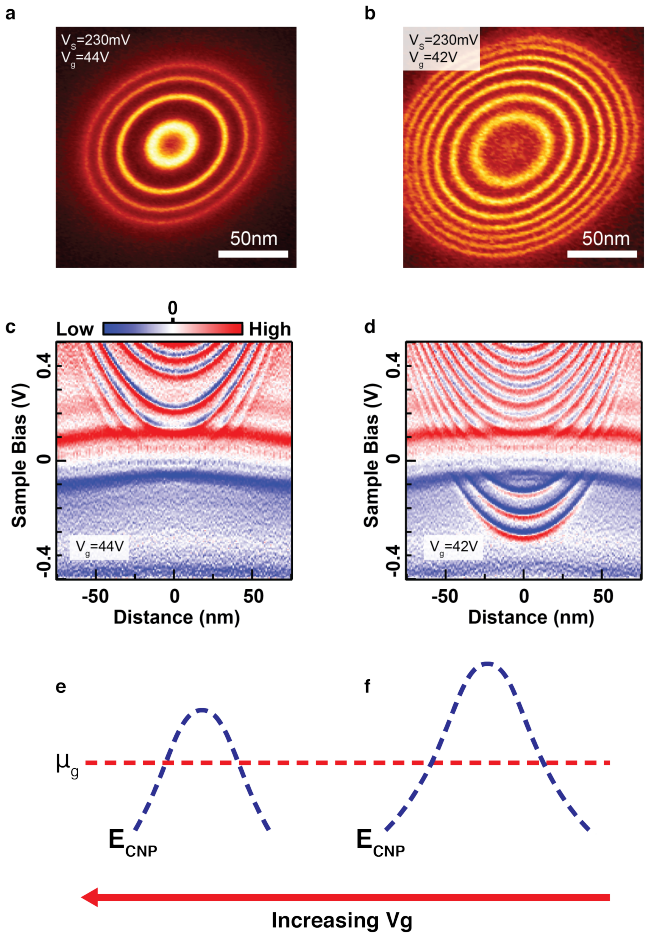

Figure 6.3: Spatially resolved STS of locally gated bilayer graphene. (a-b) $\mathrm{d}I/\mathrm{d}V_s$ maps on locally gated bilayer graphene at two different backgate voltages. (c-d) $\mathrm{d}^2I/\mathrm{d}V_s^2(V_s, x)$ measured on the same region of graphene as (a-b), where x indicates the distance on an axis going through the center of the circular p-n junction. Initial tunneling parameters for $\mathrm{d}I/\mathrm{d}V_s$ spectra: V_s= 0.5 V, I=0.5n, $V_{a.c.}$=5mV. (e-f) The chemical potential profile of a locally p-doped bilayer graphene. The charge neutrality point of graphene E_{CNP} is locally raised relative to the Fermi level of graphene μ_g, as depicted in (e). The bilayer graphene is p-doped (n-doped) when E_{CNP} lies above (below) μ_g. Lowering V_g raises E_{CNP} relative to the Fermi level, expanding the area of graphene that is p-doped.

Figs 6.3 e-f. Lowering V_g raises the CNP relative to the Fermi level, expanding the area of the graphene that is locally p-doped. Hence, a double-barrier quantum well is created when the STM tip is in tunneling position above a circular p-n junction [89], as represented in the

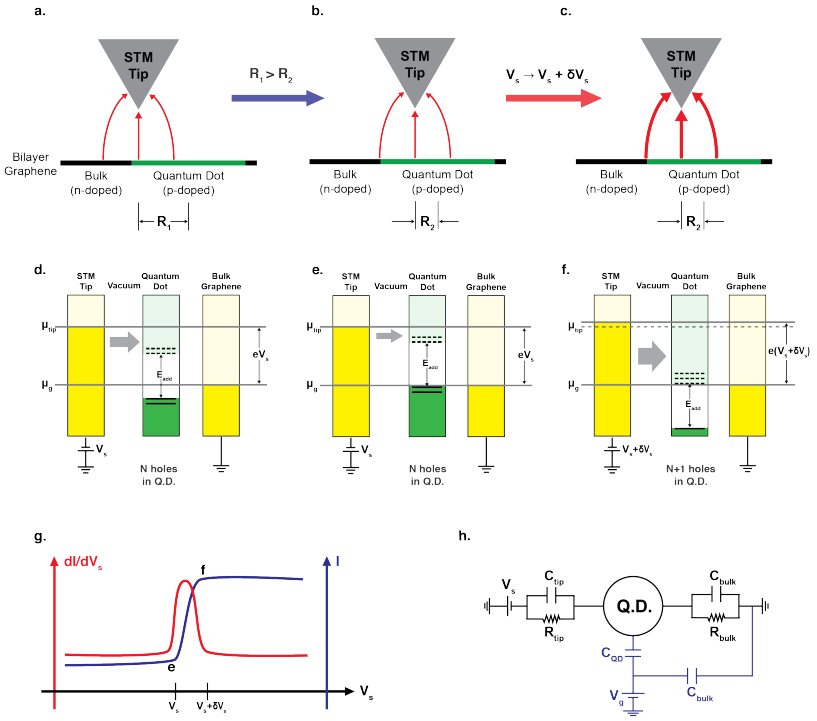

Figure 6.4: Single electron charging in a bilayer graphene quantum dot. (a-c) Schematics illustrating how the STM tip can be used to control and detect the charge state of a bilayer graphene quantum dot. In (a), the STM tip is in tunneling position at a lateral distance R_1 from the center of the quantum dot (QD). From (a) to (b), the STM tip approaches the QD ($R_1 > R_2$) while the sample bias V_s remains fixed. Then from (b) to (c), the lateral distance is held constant but a higher sample bias $V_s + \delta V_s$ is applied to the STM tip. (d-f) Energy alignments between the STM tip, the QD, and the bilayer graphene at tip positions and sample biases corresponding to (a-c). When the STM tip is in tunneling position, electron tunnels from the STM tip to the graphene via quantum dot states within a bias window of size eV_s ($e > 0$). E_C is the charging gap between unoccupied levels (represented by dashed lines) and occupied levels (represented by solid lines). From (d) to (e), the STM tip approaches the quantum dot, increasing the gating efficiency of the tip on the QD and raising its energy levels. In (f), the sample bias is increased, further shifting QD energy levels and ionizing the QD. This causes the charging energy gap E_add to fall below the bias window, resulting in a sudden increase in the number of quantum dot states in the bias window available for tunneling. (g) is a graph showing how the jump in tunneling conductance from (e) to (f) produces a peak in a $\mathrm{d}I/\mathrm{d}V_s$ spectrum. (h) A circuit diagram of the system when the STM tip is tunneling through the QD. The tip (bulk bilayer graphene) is coupled to the QD with capacitance C_{tip} (C_{bulk}) and tunneling resistance R_{tip} (R_{bulk}). The silicon backgate is coupled to the QD (C_{QD}) and the bulk bilayer graphene (C_{bulk}), but V_g is kept constant during each $\mathrm{d}I/\mathrm{d}V_s$ spectrum.

circuit diagram in Fig. 6.4h.

Using this framework, we provide an explanation for the resonances observed in our $\mathrm{d}I/\mathrm{d}V_s$ spectra and maps. In Fig. 6.4a, the STM tip is positioned on a quantum dot at some distance R_1 from the center of the QD with positive sample bias V_s. The resulting alignment of electrochemical potentials is depicted in Fig. 6.4d, where unoccupied QD eigenstates (dashed lines) are separated from occupied QD eigenstates (solid lines) by an addition energy E_{add}[90]. When the lateral distance between the STM tip and the QD is decreased from R_1 to R_2, as shown in Fig. 6.4b, the QD energy levels are raised due an increased gating efficiency, i.e. greater C_{tip} [53]. From Fig. 6.4b to Fig. 6.4c, the STM bias voltage is increased slightly from V_s to $V_s+\delta V_s$ while the lateral position is fixed, which further lifts the QD potential [53]. When a shift in QD levels causes the highest occupied QD level to cross the electrochemical potential of the bilayer graphene μ_g, as shown in Fig. 6.4f an electron tunnels out of the QD and the addition energy E_{add} flips below the newly emptied QD level, so that E_{add} now lies below the bias window. Since tunneling rate is determined by the number of empty QD states available within the bias window, this produces a sudden jump in the current and a peak in the $\mathrm{d}I/\mathrm{d}V_s$ spectrum, as shown in Fig. 6.4g. These sharp resonances occur in $\mathrm{d}I/\mathrm{d}V_s$ spectra and maps each time a change in the bias voltage V_s or the lateral distance R produces a shift of E_{add} in the QD potential, causing an occupied QD level to cross μ_g. These are Coulomb oscillations and the phenomenon of successive charging is known as the Coulomb staircase [88, 90, 91].

These Coulomb resonances provide information about the electronic structure of bilayer graphene quantum dots. The energy spacing between charging peaks in $\mathrm{d}I/\mathrm{d}V_s$ spectra is determined by $E_{add} = \Delta E + E_C$, where ΔE is the single particle orbital splitting and $E_C = e^2/C$ is the charging energy required to add an electron to a quantum dot that has total capacitance C[90]. Both ΔE and E_C should increase when the QD diameter is decreased, which is consistent with the trend observed in Figs 6.3 where the energy spacing between Coulomb peaks in $\mathrm{d}I/\mathrm{d}V_s$ spectra is smaller for the larger circular p-n junction. Furthermore, $\mathrm{d}I/\mathrm{d}V_s$ spectra in Fig. 6.3c show equal energy spacing except between the fourth and the fifth charging resonances, where the energy spacing is larger than the rest. This suggests that there is four-fold degeneracy in QD energy levels due to spin and valley symmetries, so that ΔE makes non-zero contribution only when an electron added to an empty QD orbital. For the larger dot in Figs 6.3d, however, Coulomb peaks are equally spaced, implying that ΔE does not make significant contribution to the additional energy E_{add}. This suggests that when the circular p-n junction size is increased, locally gated bilayer graphene acts as a classical dot where single particle orbital spacing is not important. Hence the backgate allows a tunable evolution of locally gated bilayer graphene from quantum dots to classical dots.

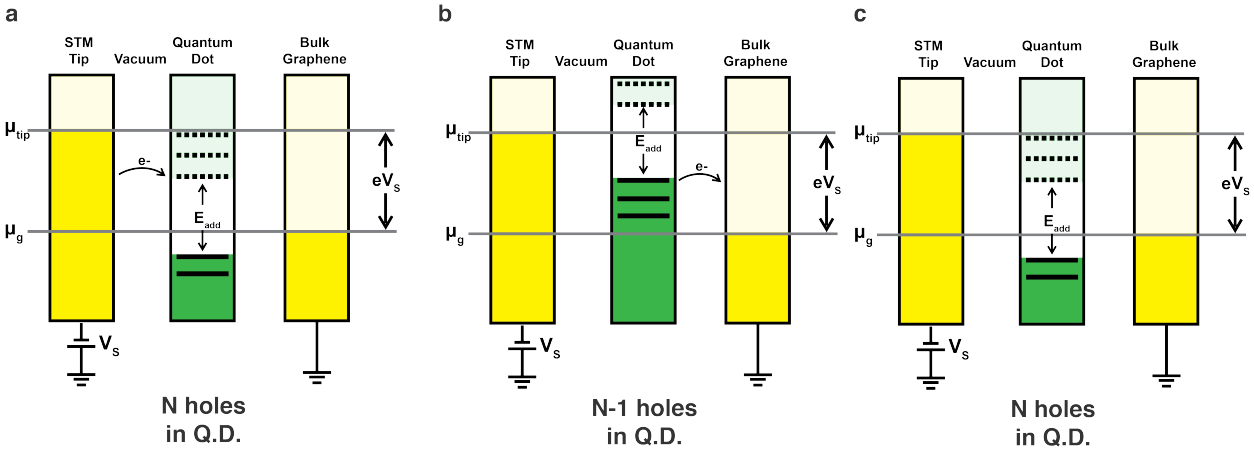

Figure 6.5: Electrochemical potential landscape as an electron tunnels through a quantum dot (QD). In (a), the STM tip is in tunneling position on a quantum dot with sample bias V_s , which creates a bias window of eV_s. The empty, discrete states of the QD are available for electrons from the STM tip to tunnel into. There is an addition gap of E_{add} between the highest occupied level and the lowest unoccupied level of the QD. When an electron from the STM tip tunnels into one of the states in the QD, the chemical potential of the QD is moved up, as shown in (b). The location of the addition gap flips above the newly occupied QD state. Electrons from the QD can now tunnel in bulk graphene, which brings the QD chemical potential back to the original configuration, as shown in (c).

6.3.1 Single Electron Tunneling through a Bilayer Graphene Quantum Dot

While describing the model for single electron charging in the previous section, we claimed that the tunneling conductance is determined by the number of available QD states within the bias window. The underlying assumption here is that the tunneling resistance between the STM tip and the quantum dot is much larger than the resistance between the quantum dot and the bulk graphene, i.e. $R_{tip} \gg R_{bulk}$). This asymmetry in tunneling resistance results in a Coulomb staircase behavior where the magnitude of the tunneling current is determined by the number of QD states within the bias window in the configurations shown in Fig. 6.4d-f [88].

When an electron tunnels into the QD from the STM tip, the electrochemical potential landscape is temporarily altered. Figure 6.5a-c shows how the electrochemical potential landscape changes as an electron tunnels from the STM tip to the quantum dot, then to the bulk graphene. In Figure 6.5a, there are empty QD states available for an electron from the STM tip to tunnel into. When an electron tunnels into an empty QD state, as shown in Figure 6.5b, the electrochemical potential of the QD is shifted up to where that state was. Then the electron tunnels out of the quantum dot into the bulk graphene, at which point the potential alignments go back to the original state, as shown in Figure 6.5c. When

$R_{tip} \gg R_{bulk}$, there is relatively very little time spent in the intermediate configuration, which is why the tunneling conductance is unaffected by the intermediate potential landscape.

6.4 Electron Quantum Dots in Bilayer Graphene

In Section 6.3, we examined a circular p-n junction in bilayer graphene created by a negative local embedded gate. The confined states for such circular p-n junctions are hole states. Due to the electron-hole symmetry in bilayer graphene [2], circular p-n junctions of the opposite polarity should produce confined electronic states. In this section, we investigate electron quantum dots in bilayer graphene by fabricating positive local embedded gates. We find evidence that electronic states are confined within n-doped circular p-n junctions. Furthermore, we obtain greater insight into the competition between STM tip-induced confinement potential and the embedded gate-induced electric fields.

To confine electronic states in bilayer graphene p-n junctions, we created a positive local embedded gate by applying an STM tip voltage pulse at $\tilde{V}_g = -80V$. Then we obtained spatially resolved STS through an arbitrary axis going through the center of the pulsed region, as shown in the measurement scheme sketched in Fig. 6.6. $\mathrm{d}I/\mathrm{d}V_s$ spectra were measured and plotted as $\mathrm{d}^2I/\mathrm{d}V_s^2(d, V_s)$ for various V_g as shown in Fig. 6.6b-g. Several interesting features and trends are observed in these data. First, there are red and blue lines near $V_s = 0$V arising from phonon-assisted inelastic tunneling [49, 87]. There are also prominent peaks that increase as a function of distance $|d|$ from the center of the circular p-n junction. Additionally, there is a set of resonances that disperse in the opposite direction as a function of $|d|$, which were not observed in STS of hole quantum dots in Section 6.3. Furthermore, two trends appear as the backgate is decreased: (1) the energy spacing between charging resonances decreases and (2) the resonances shift up in energy (V_s).

$\mathrm{d}I/\mathrm{d}V_s$ maps on these n-doped circular p-n junctions were obtained, as shown in Fig. 6.7. Approximately circular rings can be observed, but unlike in Fig. 6.3, the rings appear to be organized into two groups, as may be expected from Fig. 6.6.

Most of the features and trends in Fig. 6.6 and 6.6 can be explained by the model used in Section 6.3. As V_g is increased, the graphene becomes more n-doped, which expands the size of the internally n-doped circular p-n junction. As the quantum dot size increases, the addition energy $E_{add} = \Delta E + E_C$ should decrease, which is consistent with the trend observed in the experiment. Furthermore, increasing the gate should shift down the electrochemical potential of the quantum dot, requiring higher sample bias V_s to ionize the same states. Hence, as the gate increases from Fig. 6.6b to Fig. 6.6g, the charging resonances appear to move up in energy.

Based on the data on hole quantum dots in Section 6.3, we would naively expect all the charging peaks to move down in energy as a function of distance $|d|$. Indeed there is a quartet of peaks that decrease in V_s as a function $|d|$. Additionally, however, there are numerous, less prominent charging peaks in Fig. 6.6 that increase in V_s as a function of $|d|$.

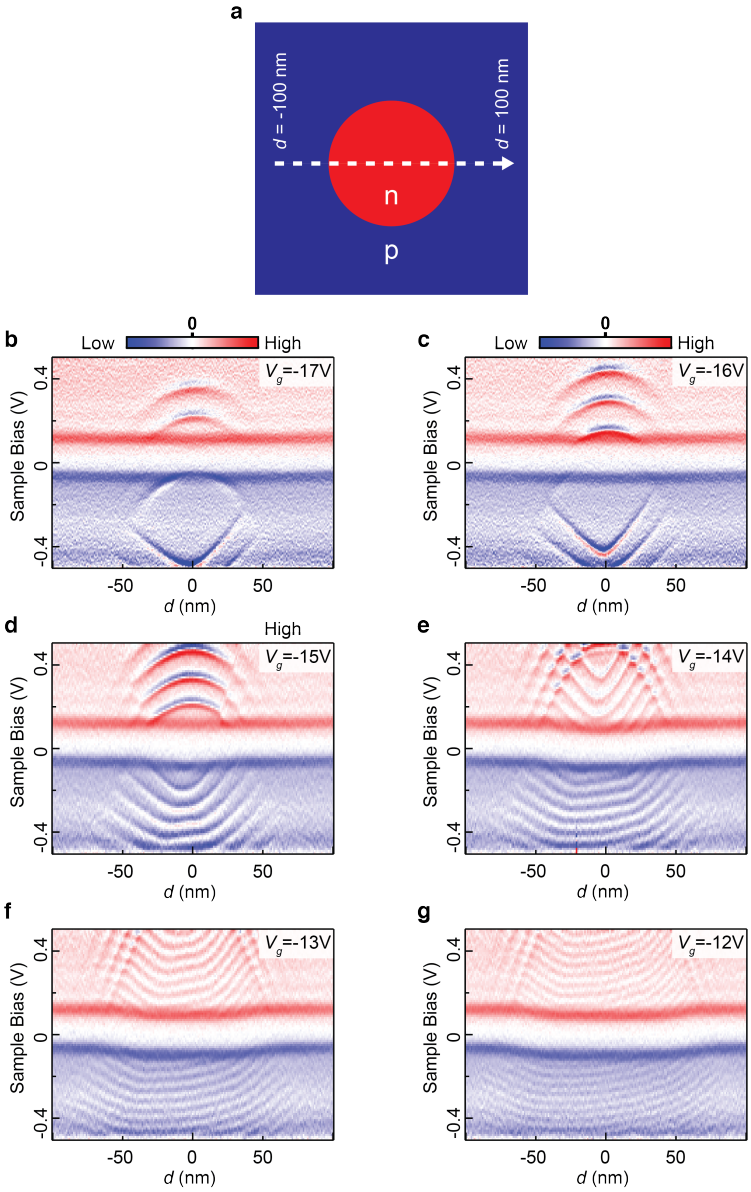

Figure 6.6: Charging resonance spectroscopy of locally n-doped in bilayer graphene (a) Schematic for spectroscopic measurement on a locally n-doped region of bilayer graphene. Distance d is defined as the radial distance from the STM tip pulse, as shown in (a). STM tip pulse was performed at $\tilde{V_g}$ =-80V, h_{lift}=1.9nm, V_s=5V, and Δt=3 min. (b-g) $\mathrm{d}^2I/\mathrm{d}V_s^2(d, V_s)$ at various backgate voltages V_g. Initial tunneling parameters for all $\mathrm{d}I/\mathrm{d}V_s$ spectra: V_s =-0.5V, I=0.5nA, $V_{a.c.}$= 5mV.

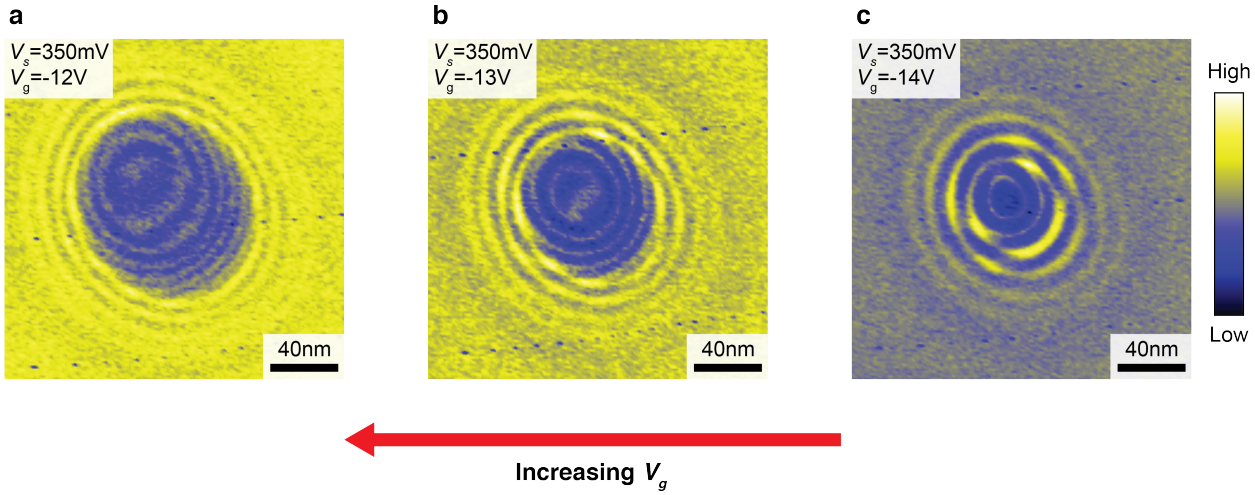

Figure 6.7: Charging rings of electron quantum dots in bilayer graphene (a-c) $\mathrm{d}I/\mathrm{d}V_s$ maps showing charging rings around electron quantum dots in bilayer graphene. The quantum dot was fabricated with an STM tip pulse at $\tilde{V}_g$ =-80V, h_{lift}=1.9nm, V_s=5V, Δt=3 min. As V_g increases, the quantum dot size also increases. Tunneling parameters for $\mathrm{d}I/\mathrm{d}V_s$ maps: I= 130pA, $V_{a.c.}$=5mV.

While further modeling is necessary to fully understand this complicated behavior of charging resonances, a consistent picture can be formulated by assuming that there are two quantum dots in this system: a p-doped quantum dot induced by the STM tip acting as a negative top gate and an n-doped quantum dot induced by the positive bottom gate. The STM tip usually acts as a negative gate due to its work function difference with the graphene [53]. Then the STM tip can potentially create a circular p-n junction with p-doped internal cavity within a region of the graphene that is n-doped by a wider, positive local embedded gate, which results in a circular p-n-p junction for a range of V_g. In this picture, the STM tip acts to create a p-doped quantum dot and the positive embedded gate acts to change the charge state of the tip-induced quantum dot. This is consistent with the observation that the quartet of charging resonances in Fig. 6.6 decrease in V_s as $|d|$ increases, which is expected when a positive gate is acting to charge or discharge a quantum dot. Furthermore, the bottom set of charging resonances have the opposite distance dependence, which is expected for a quantum dot that is ionized by a negative gate. Again, this is consistent with the picture that the bottom set of resonances arise when a negatively charged STM tip ionizes an n-doped quantum dot induced by the positive embedded gate.

This picture suggests an alternative explanation of the results discussed in Section 6.3. In Figure 6.4, we explained the charging resonances by assuming that the STM tip acts to ionize the quantum dot induced by a local embedded gate. However, the same phenomenology is expected if the roles of the STM tip and the embedded gate are reversed. There was not a good way to disambiguate between the two perspectives in Section 6.3, but the results of this section suggests the possibility that the STM tip produces a stronger confinement

potential than the embedded gates. In this picture, the prominent peaks in Figs 6.2 and 6.3 arise from ionization of an STM tip-induced quantum dot, while the weaker resonances observed in Fig. 6.2 may be due to ionization of an embedded gate-induced quantum dot. The physically accurate model may be a mixture of these two perspectives.

6.5 Four-Fold Degeneracy in Bilayer Graphene Quantum Dots

The data in Figure 6.3c of Section 6.3 suggests that there is four-fold degeneracy in these bilayer graphene quantum dot orbitals. In this section, we provide a more clear experimental evidence of four-fold symmetry.

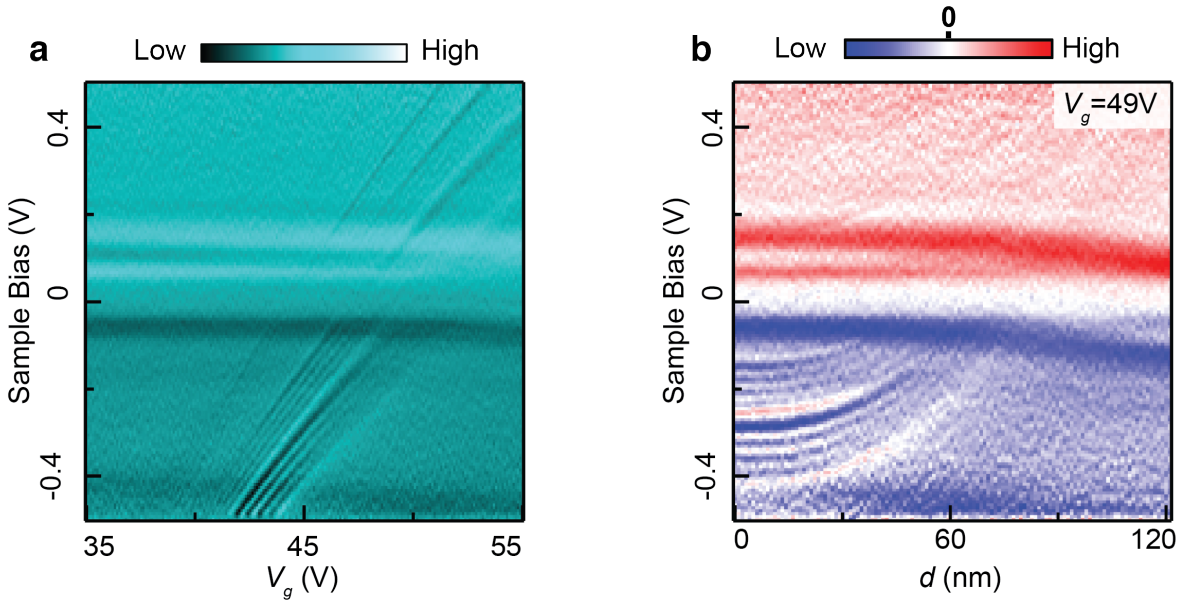

Figure 6.8: Quartets of charging resonances in a bilayer graphene quantum dot. (a) $\mathrm{d}^2I/\mathrm{d}V_s^2(V_g, V_s)$ obtained at the center of a locally gated bilayer graphene. The bilayer graphene was locally p-doped by an STM tip pulse at $\tilde{V}_g$ =60V, h_{lift}=1.8nm, V_s=5V, and Δt=1 min. Charging resonances appear in quartets. (b) $\mathrm{d}^2I/\mathrm{d}V_s^2(d, V_s)$ on the same quantum dot, where d is the radial distance from the center of the quantum dot (i.e. the location of the STM tip pulse). Initial tunneling parameters for all $\mathrm{d}I/\mathrm{d}V_s$ spectra: V_s =-0.5V, I=0.5nA, $V_{a.c.}$= 5mV.

Figure 6.8a shows $\mathrm{d}^2I/\mathrm{d}V_s^2(V_g, V_s)$ obtained after an STM tip voltage pulse was applied at $\tilde{V}_g$ = 60V. This creates a negative embedded gate, which confines hole states in a circular p-n junction. As was observed in Fig. 6.2, there is a band around V_s=0V corresponding to the phonon pseudogap. However, the charge neutrality point is more visible here (bright line above the phonon feature) than in Fig. 6.2. Also, there are up to five quadruplets of charging

resonances in this plot. In Fig. 6.2, only the first quadruplet appeared to be grouped together while the rest of the resonances were clumped together without clear fourfold grouping (suggesting that ΔE made negligible contribution to E_{add}). Figure 6.8b is a $\mathrm{d}^2I/\mathrm{d}V_s^2(d, V_s)$ plot on the same circular p-n junction obtained at $V_g = 49$V that confirms that the resonances are grouped into quartets. Compared to Fig. 6.3, there are few differences: the resonances are not as prominent, the resonances do not appear above the phonon gap, the quartet grouping is more evident, and the charge neutrality point is visible above the phonon gap for small d.

The differences between $\mathrm{d}I/\mathrm{d}V_s$ spectra obtained for the quantum dot in Figure 6.8 and for those in Fig. 6.3 or Fig. 6.2 may be because of the STM tip. A different STM tip was used for this data set. Although our STM tips are always calibrated with the same procedure, they are never exactly the same. Another possible factor contributing to the difference may be the shape of the confinement potential. Here $\tilde{V}_g = 60$V was used, while $\tilde{V}_g = 40$V was used in Fig. 6.3 or Fig. 6.2.

6.6 Coupled Quantum Dots in Bilayer Graphene

6.6.1 P-Doped Quantum Dots

As shown in Figure 4.11b, we performed STM tip voltage pulses with $\tilde{V}_g = 80$V at two locations separated by 200 nm. The charge density landscape should resemble the sketches in Figure 4.11a-c. When V_g is large, there are two p-doped regions centered around the positions of the tip voltage pulses and separated from each other, as shown in Fig. 4.11c. When V_g is lower, the p-doped regions will merge, as shown in Fig. 4.11a.

In order to explore the resulting electronic structure of these p-n junctions, we measured $\mathrm{d}I/\mathrm{d}V_s$ spectra through an axis passing through the two locations where STM tip voltage pulses were applied. The measurement scheme is shown in Fig. 4.11c and $\mathrm{d}^2I/\mathrm{d}V_s^2(d, V_s)$ plots at four different V_g are shown in Figs 4.11d-g. The red and blue lines near $V_s = 0$V arise from phonon-assisted inelastic tunneling[49, 87]. Conspicuous peaks appear in $\mathrm{d}^2I/\mathrm{d}V_s^2(d, V_s)$ plots. And as was observed for circular p-n junctions in bilayer graphene (Section 6.3), the energy spacing between peaks increase as V_g is increased. While the resonances had parabola-like shape for circular p-n junctions, the resonances in Figs 4.11d-g reflect the non-circular geometry of the embedded gates.

Fig. 6.10 shows $\mathrm{d}I/\mathrm{d}V_s$ maps at $V_g = 53$V for four values of V_s. The locations of the STM tip pulses and scan window dimensions are sketched in Fig. 4.11b. Sharp elongated rings appear in $\mathrm{d}I/\mathrm{d}V_s$ maps. As the sample bias is lowered, the number of rings and the spatial density of rings decrease.

The precise shape and magnitude of the resulting local embedded gates in Figs 4.11 and 6.10 is not known with certainty. In particular, more analysis is necessary to decouple the effects of the STM tip as the top gate and of the effect of embedded bottom gates. Here we present several possible scenarios. First, the sharp resonances may indicate single electron

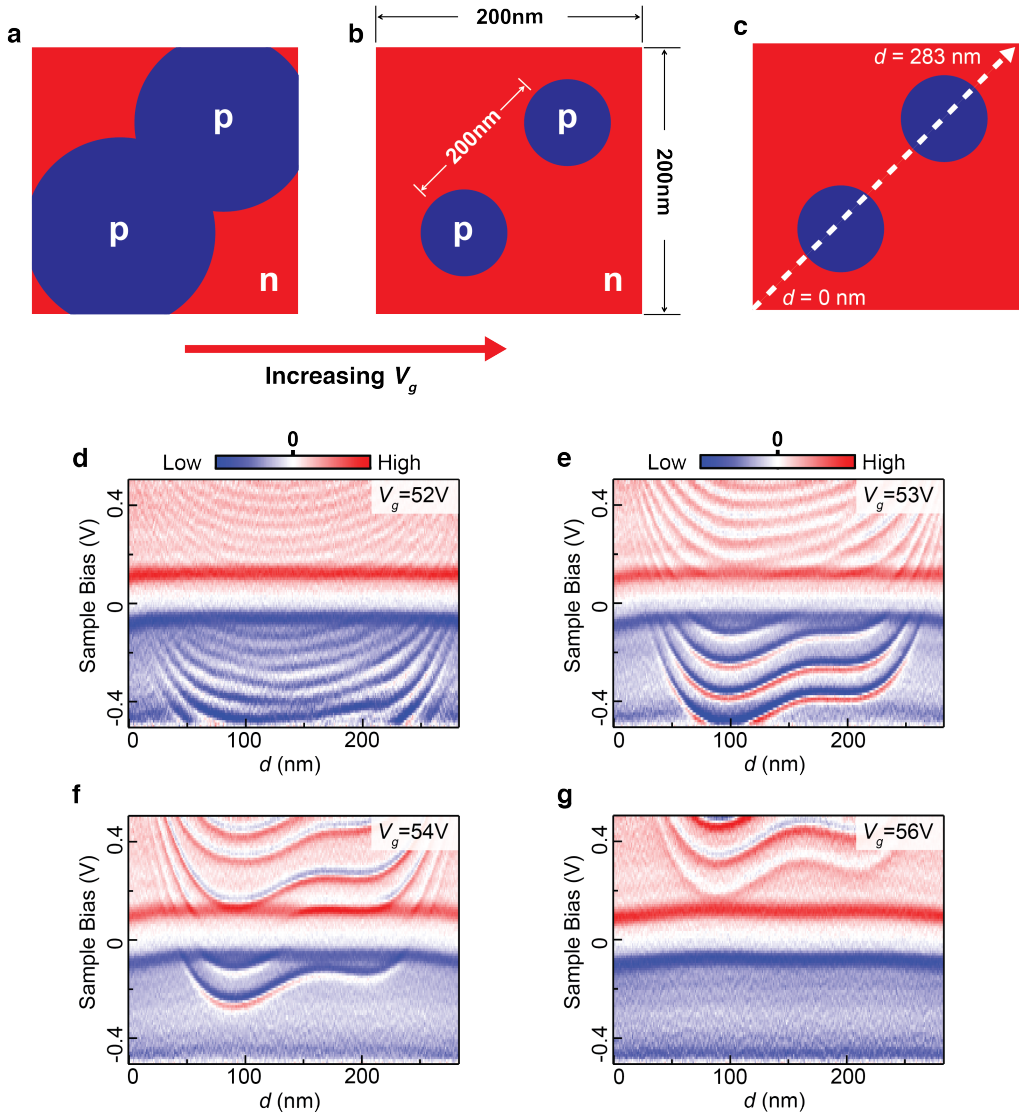

Figure 6.9: Spatially resolved STS on coupled bilayer graphene quantum dots (p-doped) (a-c) Measurement scheme for distance-resolved $\mathrm{d}I/\mathrm{d}V_s$ spectra and $\mathrm{d}I/\mathrm{d}V_s$ maps. STM tip voltage pulses were applied at two locations separated by 200 nm with parameters $\tilde{V_g}$ =80V, h_{lift}=1.9nm, V_s=5V, and Δt=3min. As V_g increases, the size of circular p-n junctions decreases. Distance d is defined as shown in (c). (d-g) $\mathrm{d}^2I/\mathrm{d}V_s^2(d, V_s)$ at various backgate voltages V_g. Initial tunneling parameters for all $\mathrm{d}I/\mathrm{d}V_s$ spectra: V_s =-0.5V, I=0.5nA, $V_{a.c.}$= 5mV.

charging of a quantum dot produced by the STM tip. As discussed in previous sections, the STM tip acts as a top gate that usually p-dopes the graphene below, which may create a

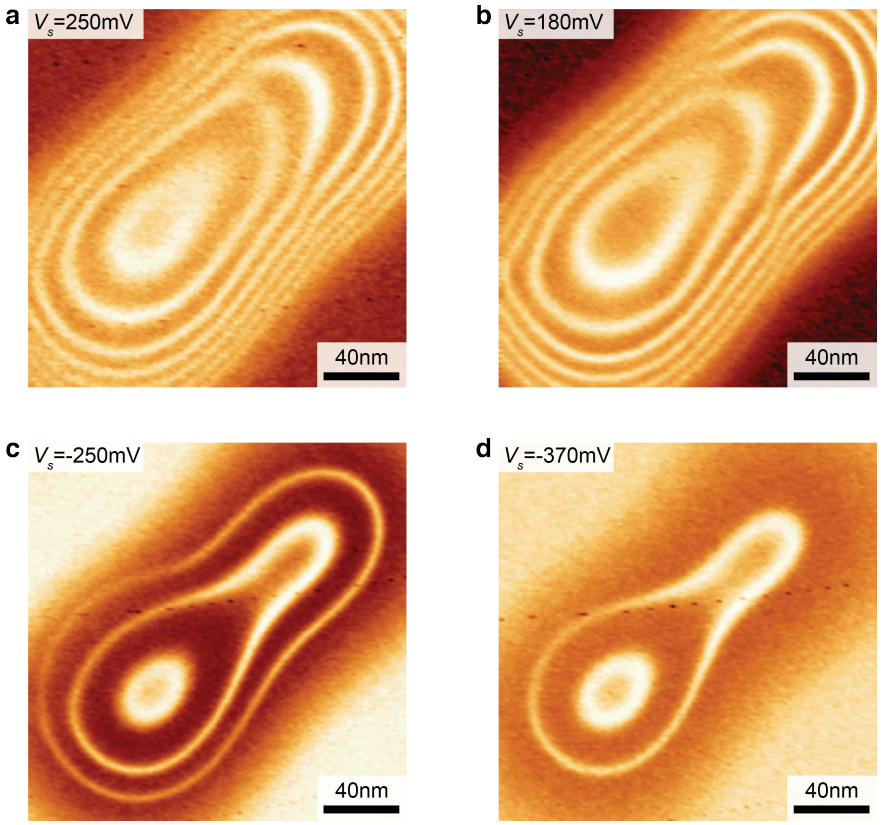

Figure 6.10: $\mathrm{d}I/\mathrm{d}V_s$ maps on coupled bilayer graphene quantum dots (p-doped) (a-d) $\mathrm{d}I/\mathrm{d}V_s$ maps showing charging rings for various sample biases V_s at a fixed backgate (V_g=53). The bilayer graphene was p-doped with STM tip pulses at $\tilde{V}_g$ =80V, h_{lift}=1.9nm, V_s=5V, and Δt=3min. Tunneling parameters for $\mathrm{d}I/\mathrm{d}V_s$ maps: I= 100pA, $V_{a.c.}$=5mV.

p-doped quantum dot. In this scenario, the embedded gates act to change the charge state of the quantum dot that follows the STM tip. Another possibility is that the embedded gates produce one bilayer graphene quantum dot defined by a non-circular p-n junction. The p-n junction shape changes as V_g is varied, but sharp charging resonances are always observed. This would then indicate that massive Dirac fermion confinement is very robust and occurs for various different non-circular p-n junction geometries. Finally, the charging resonances may come from two distinct quantum dots created by two separate circular p-n junctions. All three explanations are consistent with the trends observations in Figs 4.11 and 6.10. As V_g is increased, the quantum dots should decrease in size, which would result in greater E_{add} and larger peak-to-peak energy spacing, as observed in Figs 4.11 and 6.10. While further analysis is necessary to fully disambiguate between these three possibilities, the discussion in the following section (Sec. 6.6.2) suggests that the first possibility (quantum confinement occurs due to STM tip gating and embedded gates act to charge and discharge the quantum dot) is the most likely.

6.6.2 N-Doped Quantum Dots

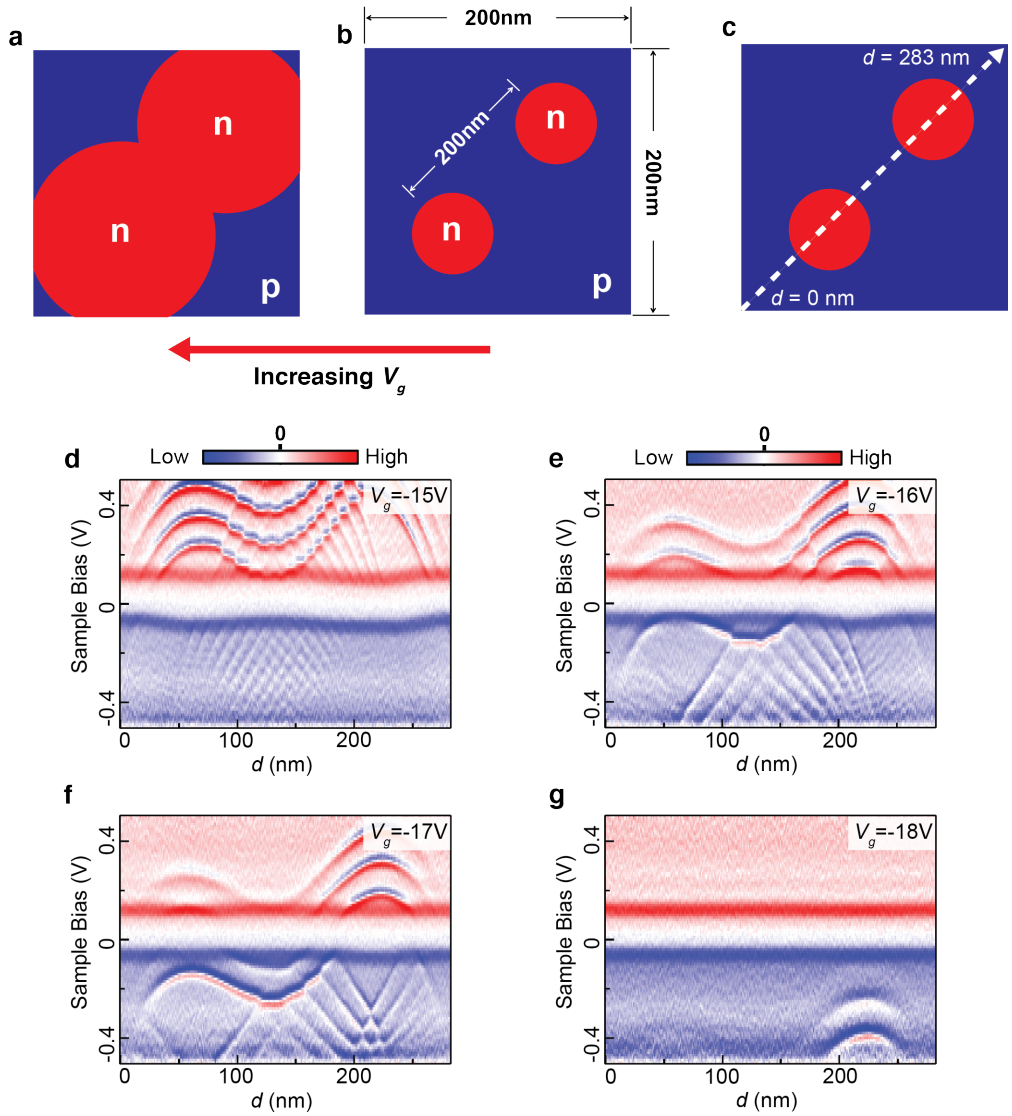

Figure 6.11: Spatially resolved STS on coupled bilayer graphene quantum dots (n-doped) (a-c) Measurement scheme for distance-resolved $\mathrm{d}I/\mathrm{d}V_s$ spectra and $\mathrm{d}I/\mathrm{d}V_s$ maps. STM tip voltage pulses were applied at two locations separated by 200 nm with parameters $\tilde{V}_g$ =-80V, h_{lift}=1.9nm, V_s=5V, and Δt=3min. As V_g increases, the size of circular p-n junctions increases. Distance d is defined as shown in (c). (d-g) $\mathrm{d}^2I/\mathrm{d}V_s^2(d, V_s)$ at various backgate voltages V_g. Initial tunneling parameters for all $\mathrm{d}I/\mathrm{d}V_s$ spectra: V_s =-0.5V, I=0.5nA, $V_{a.c.}$= 5mV.

We proceed to examine coupled n-doped quantum dots in bilayer graphene. As shown in Fig. 6.11b, we performed STM tip pulses at two locations 200 nm apart while holding the

backgate at $\tilde{V}_g$=-80V, which creates two positive embedded gates in hBN. The response of the charge carriers in the bilayer graphene is sketched in Figs 6.11a-b, where increasing V_g expands the region of the graphene that is n-doped.

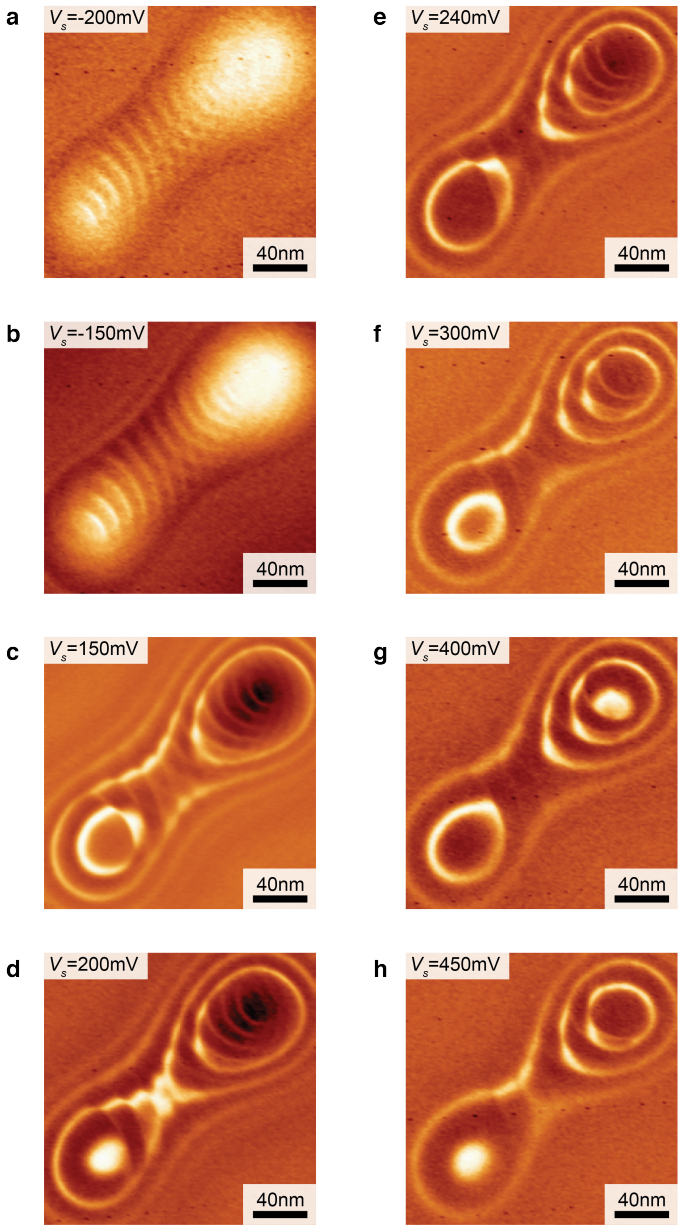

Figure 6.12: $\mathrm{d}I/\mathrm{d}V_s$ maps on coupled bilayer graphene quantum dots (n-doped) (a-h) $\mathrm{d}I/\mathrm{d}V_s$ maps showing charging rings observed for various sample biases V_s at a fixed backgate V_g=-15V. STM tip voltage pulses were applied at $\tilde{V}_g$ =-80V, h_{lift}=1.9nm, V_s=5V, and Δt=3min. Tunneling parameters for $\mathrm{d}I/\mathrm{d}V_s$ maps: I= 100pA, $V_{a.c.}$=5mV.

To investigate the elctronic structure of these p-n junctions, we obtained $\mathrm{d}I/\mathrm{d}V_s$ spec-

tra along an axis going through the locations of the STM tip voltage pulses, as shown in Fig. 6.11c. Data obtained for four values of V_g are plotted as $\mathrm{d}^2I/\mathrm{d}V_s^2(d, V_s)$ in Figs 6.11d-g. As always, the plots show a phonon gap [49, 87] around V_s=0V. Numerous charging peaks also appear. The upper quartet of peaks have larger widths and energy spacing, while the resonances occurring at lower V_s have narrower linewidths, vary in shape and number as V_g is changed, and are not limited to appear in quadruplets.

$\mathrm{d}I/\mathrm{d}V_s$ maps were obtained for these bilayer graphene p-n junctions at V_g=-15V for eight different values of V_s, as shown in Fig. 6.12. The locations and dimensions of the $\mathrm{d}I/\mathrm{d}V_s$ maps are sketched in Fig. 6.11b. Numerous bright peaks appear in these $\mathrm{d}I/\mathrm{d}V_s$ maps, and they may be divided into two groups based on their shape and brightness. There is a set of peaks that appear brighter and follow the contours of the doping landscape (like two-dimensional dumbbells or Cassini ovals). These non-circular peaks are similar in shape to the p-n junction boundary sketched in Fig. 6.11a. The other, less prominent set of peaks do not follow the curvature of the p-n junction boundary in Fig. 6.11a but are concentric about the centers of STM tip voltage pulses. This is apparent in Figs 6.11a-c or f, where these resonances form lines that are perpendicular to the dumbbell-shaped envelopes.

We now discuss the origin of peaks observed in Figs 6.11 and 6.12. There are at least three different types of p-n junctions that can act as quantum dots and produce Coulomb oscillations observed in our $\mathrm{d}I/\mathrm{d}V_s$ spectra and maps: (1) STM tip-induced, p-doped quantum dot, (2) two distinct n-doped quantum dots induced by two separate positive embedded gates, and (3) a non-circular, n-doped quantum dot defined by the combined confinement potential of the embedded gates.

Our experimental data can be consistently explained by positing that the more prominent peaks appearing in $\mathrm{d}I/\mathrm{d}V_s$ spectra and maps are Coulomb oscillations associated with an STM tip-induced quantum dot while the weaker resonances are charging rings for the two n-doped quantum dots induced by embedded gates. As mentioned above, $\mathrm{d}I/\mathrm{d}V_s$ maps in Fig. 6.12 revealed that weaker resonances are concentric about the locations of the two STM tip pulses. This suggests that these resonances are charging rings for quantum dots centered at those two positions. On the other hand, the stronger charging peaks are Cassini oval-shaped. This is consistent with the picture that a Cassini oval-shaped bottom gate causes charging and discharging of electrons from the quantum dot that moves with the STM tip. Furthermore, the stronger peaks have the expected V_s vs $|d|$ behavior of a quantum dot that is ionized by a positive gate (See discussion in Section 6.4). And the weaker peaks appear to branch out from the two tip pulse locations and increase in V_s away from those locations. In Figs 6.11e and f, for instance, V-shaped peaks appear near d =70 nm and d =220 nm. Again, this behavior is consistent with our model since charging rings induced by a negative gate should increase in energy V_s as a function of the distance from an ionizing gate, as is the case here.

6.7 Increasing Confinement Potential Strength in Bilayer Graphene Quantum Dots

In Sections 6.6.1 and 6.6.2, we found that the STM tip acts as a top gate on the bilayer graphene, which plays a significant role in STS characterization bilayer graphene p-n junctions. It is important, then, to be able to decouple the effects of the STM tip top gate and the embedded bottom gate. In particular, it would be useful to isolate the effect of the embedded bottom gate and minimize the intrusiveness of the STM tip top gate. In this section, we take a step towards this direction by creating an embedded gate whose confinement potential is significantly stronger than those reported in previous sections.

In order to create an embedded gate with steeper confinement potential, we made several changes to our STM tip voltage pulse procedure. First, we applied STM tip voltage pulses multiple times at numerous points scattered throughout the scan window with h_{lift}=1.2nm and V_s=5V while holding the backgate at $\tilde{V}_g$ = -80V. This effectively n-doped the region in and around the scan area uniformly. When we take $\mathrm{d}I/\mathrm{d}V_s$ spectra near the scan area after such a procedure at $V_g = \tilde{V}_g$, we obtain the $\mathrm{d}I/\mathrm{d}V_s$ spectrum for neutral bilayer graphene. This indicates that there is a uniform embedded gate that completely screens the backgate and is equivalent in magnitude to $\tilde{V}_g$. After creating a uniform background doping using this method, we fabricated a negative local gate in the center of the scan area by applying a voltage pulse with h_{lift} =800 pm. This means that the STM tip is much closer to the surface of the graphene than previously when h_{lift} ≈2 nm was used. We also used a lower pulse voltage and shorter pulse time (V_s=3.75V, Δt <1s).

To characterize the resulting electronic structure, we measured $\mathrm{d}I/\mathrm{d}V_s$ spectra as a function of radial distance d from the location of the last voltage pulse, as shown in Figure 6.13c. Smooth oscillatory features can be observed in the lower left part of the plot, while checkerlike pattern is visible on the upper right. A white line acts as a boundary between these two patterns. Figure 6.13d shows $\mathrm{d}I/\mathrm{d}V_s$ spectra obtained with the same measurement scheme as Figure 6.13c but for a different STM tip voltage pulse. Parameters similar to what was used for creating embedded gates in previous Sections 6.6.1 and 6.6.2 were used ($\tilde{V}_g$ =60V, h_{lift}=1.8nm, V_s=5V, Δt=1min) in the absence of any background doping. Similar to Figure 6.13c, there is a white diagonal line dividing blue and red regions. Unlike Fig. 6.13d, however, there are four narrow resonances that move up with distance d but other oscillatory features are absent.

The two embedded gates in Fig. 6.13c and d clearly produces different electronic structures. The local charge neutrality point approximately follows the white diagonal lines in these plots. The CNP moves about 100 mV in Fig. 6.13c over a distance of 120 nm while the CNP moves half as much or less over the same distance in Fig. 6.13d. As illustrated in Fig. 6.13a and b, measurement of the CNP reveals the confinement potential profile induced by the embedded gate. Hence, it is evident that the confinement potential is much stronger in Fig. 6.13c than in Fig. 6.13d. The interpretation of the charging resonances in Fig. 6.13d were discussed in previous sections. The new features observed in Fig. 6.13c have

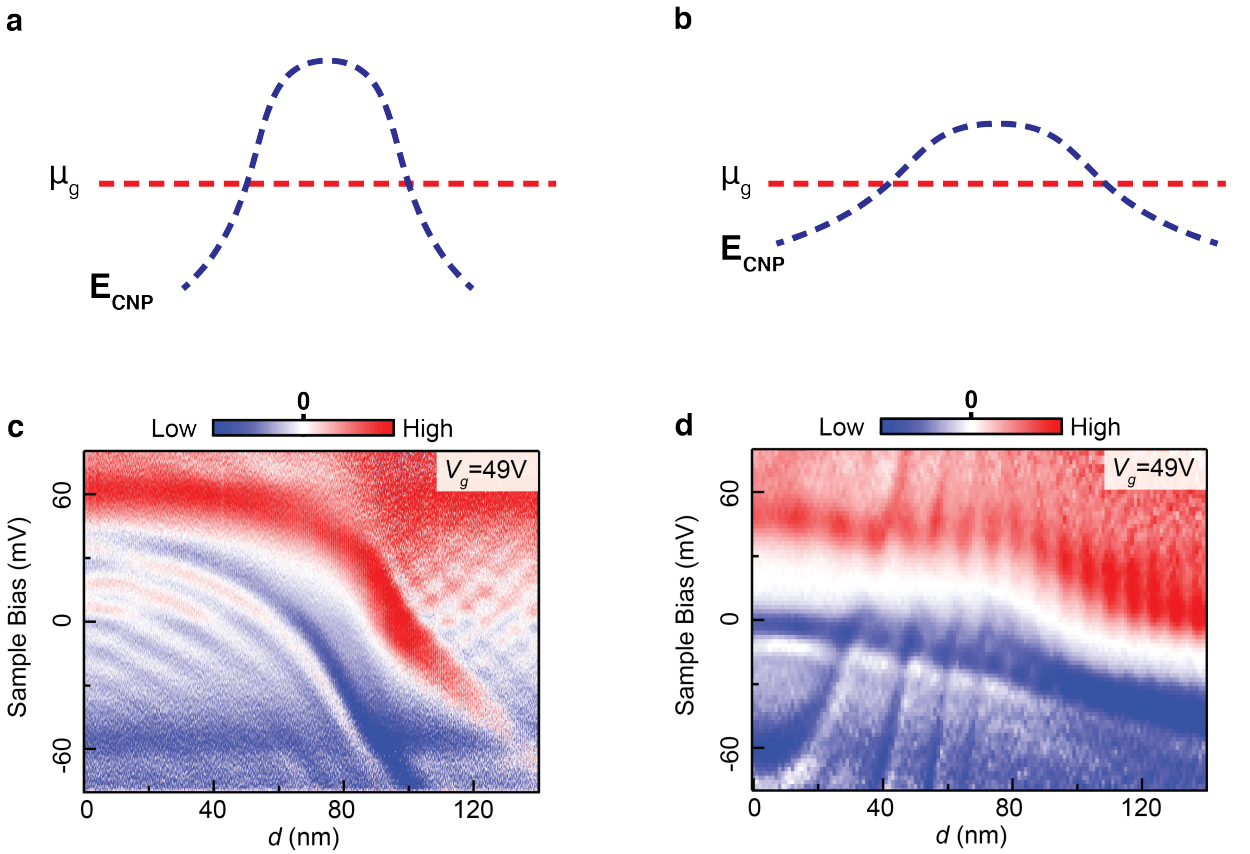

Figure 6.13: Effect of confinement potential on the electronic structure of quantum dots in bilayer graphene (a-b) Schematics showing a deep, sharp confinement potential (a) and shallow confinement potential (b). (c) $\mathrm{d}^2I/\mathrm{d}V_s^2(d, V_s)$ for a strong confinement potential created with an STM tip pulse at $\tilde{V_g}$ =80V, h_{lift}=800pm, V_s=3.75V, Δt <1s and background doping at $\tilde{V_g}$ =-80V h_{lift}=1.2nm. Initial tunneling parameters: V_s =-0.1V, I=1nA, $V_{a.c.}$= 1mV.(d) $\mathrm{d}^2I/\mathrm{d}V_s^2(d, V_s)$ for a shallow confinement potential created with an STM tip pulse at $\tilde{V_g}$ =60V, h_{lift}=1.8nm, V_s=5V, Δt=1min. Initial tunneling parameters: V_s =-0.1V, I=1nA, $V_{a.c.}$= 2mV.

not been discussed so far, and they provide an exciting invitation for future experimental and theoretical investigations.

Thus, we have demonstrated that by changing parameters of the STM tip voltage pulse procedure, we are able to create quantum dot confinement potentials of variable strength.

Bibliography

[1]P. R. Wallace, "The band theory of graphite", Phys. Rev. **71**, 622–634 (1947).

[2]A. H. Castro Neto, F. Guinea, N. M. R. Peres, K. S. Novoselov, and A. K. Geim, "The electronic properties of graphene", en, Reviews of Modern Physics **81**, 109–162 (2009).

[3]M. I. Katsnelson, K. S. Novoselov, and A. K. Geim, "Chiral tunnelling and the Klein paradox in graphene", Nature Physics **2**, 620–625 (2006).

[4]L. A. Ponomarenko, F. Schedin, M. I. Katsnelson, R. Yang, E. W. Hill, K. S. Novoselov, and A. K. Geim, "Chaotic Dirac Billiard in Graphene Quantum Dots", en, Science **320**, 356–358 (2008).

[5]S. Schnez, J. Gttinger, M. Huefner, C. Stampfer, K. Ensslin, and T. Ihn, "Imaging localized states in graphene nanostructures", en, Physical Review B **82** (2010) 10.1103/PhysRevB.82.165445.

[6]K. Todd, H.-T. Chou, S. Amasha, and D. Goldhaber-Gordon, "Quantum Dot Behavior in Graphene Nanoconstrictions", en, Nano Letters **9**, 416–421 (2009).

[7]M. Y. Han, B. zyilmaz, Y. Zhang, and P. Kim, "Energy Band-Gap Engineering of Graphene Nanoribbons", en, Physical Review Letters **98** (2007) 10.1103/PhysRevLett.98.206805.

[8]S. K. Hmlinen, Z. Sun, M. P. Boneschanscher, A. Uppstu, M. Ijs, A. Harju, D. Vanmaekelbergh, and P. Liljeroth, "Quantum-Confined Electronic States in Atomically Well-Defined Graphene Nanostructures", en, Physical Review Letters **107** (2011) 10.1103/PhysRevLett.107.236803.

[9]D. Subramaniam, F. Libisch, Y. Li, C. Pauly, V. Geringer, R. Reiter, T. Mashoff, M. Liebmann, J. Burgdrfer, C. Busse, T. Michely, R. Mazzarello, M. Pratzer, and M. Morgenstern, "Wave-Function Mapping of Graphene Quantum Dots with Soft Confinement", en, Physical Review Letters **108** (2012) 10.1103/PhysRevLett.108.046801.

[10]S.-h. Phark, J. Borme, A. L. Vanegas, M. Corbetta, D. Sander, and J. Kirschner, "Direct Observation of Electron Confinement in Epitaxial Graphene Nanoislands", en, ACS Nano **5**, 8162–8166 (2011).

[11]M. T. Allen, O. Shtanko, I. C. Fulga, A. R. Akhmerov, K. Watanabe, T. Taniguchi, P. Jarillo-Herrero, L. S. Levitov, and A. Yacoby, "Spatially resolved edge currents and guided-wave electronic states in graphene", Nature Physics **12**, 128–133 (2015).

[12]J. Lu, P. S. E. Yeo, C. K. Gan, P. Wu, and K. P. Loh, "Transforming C60 molecules into graphene quantum dots", Nature Nanotechnology **6**, 247–252 (2011).

[13]S. Jung, G. M. Rutter, N. N. Klimov, D. B. Newell, I. Calizo, A. R. Hight-Walker, N. B. Zhitenev, and J. A. Stroscio, "Evolution of microscopic localization in graphene in a magnetic field from scattering resonances to quantum dots", Nature Physics **7**, 245–251 (2011).

[14]Y. Wang, D. Wong, A. V. Shytov, V. W. Brar, S. Choi, Q. Wu, H.-Z. Tsai, W. Regan, A. Zettl, R. K. Kawakami, S. G. Louie, L. S. Levitov, and M. F. Crommie, "Observing Atomic Collapse Resonances in Artificial Nuclei on Graphene", en, Science **340**, 734–737 (2013).

[15]G.-H. Lee, G.-H. Park, and H.-J. Lee, "Observation of negative refraction of Dirac fermions in graphene", Nature Physics **11**, 925–929 (2015).

[16]S. Chen, Z. Han, M. M. Elahi, K. M. M. Habib, L. Wang, B. Wen, Y. Gao, T. Taniguchi, K. Watanabe, J. Hone, A. W. Ghosh, and C. R. Dean, "Electron optics with p-n junctions in ballistic graphene", en, Science **353**, 1522–1525 (2016).

[17]Y. Zhao, J. Wyrick, F. D. Natterer, J. F. Rodriguez-Nieva, C. Lewandowski, K. Watanabe, T. Taniguchi, L. S. Levitov, N. B. Zhitenev, and J. A. Stroscio, "Creating and probing electron whispering-gallery modes in graphene", Science **348**, 672–675 (2015).

[18]J. Lee, D. Wong, J. Velasco Jr, J. F. Rodriguez-Nieva, S. Kahn, H.-Z. Tsai, T. Taniguchi, K. Watanabe, A. Zettl, F. Wang, L. S. Levitov, and M. F. Crommie, "Imaging electrostatically confined Dirac fermions in graphene quantum dots", Nature Physics **12**, 1032–1036 (2016).

[19]C. Gutirrez, L. Brown, C.-J. Kim, J. Park, and A. N. Pasupathy, "Klein tunnelling and electron trapping in nanometre-scale graphene quantum dots", Nature Physics **12**, 1069–1075 (2016).

[20]F. Ghahari, D. Walkup, C. Gutirrez, J. F. Rodriguez-Nieva, Y. Zhao, J. Wyrick, F. D. Natterer, W. G. Cullen, K. Watanabe, T. Taniguchi, and others, "An on/off Berry phase switch in circular graphene resonators", Science **356**, 845–849 (2017).

[21]N. Gu, M. Rudner, and L. Levitov, "Chirality-Assisted Electronic Cloaking of Confined States in Bilayer Graphene", en, Physical Review Letters **107** (2011) `10.1103/PhysRevLett.107.156603`.

[22]K. Lee, S. Lee, Y. S. Eo, C. Kurdak, and Z. Zhong, "Evidence of electronic cloaking from chiral electron transport in bilayer graphene nanostructures", en, Physical Review B **94** (2016) `10.1103/PhysRevB.94.205418`.

[23]K. S. Novoselov, A. K. Geim, S. V. Morozov, D. Jiang, M. I. Katsnelson, I. V. Grigorieva, S. V. Dubonos, and A. A. Firsov, "Two-dimensional gas of massless Dirac fermions in graphene", Nature **438**, 197–200 (2005).

[24]Y. Zhang, Y.-W. Tan, H. L. Stormer, and P. Kim, "Experimental observation of the quantum Hall effect and Berry's phase in graphene", Nature **438**, 201–204 (2005).

[25]A. F. Young and P. Kim, "Quantum interference and Klein tunnelling in graphene heterojunctions", Nature Physics **5**, 222–226 (2009).

[26]N. Stander, B. Huard, and D. Goldhaber-Gordon, "Evidence for Klein Tunneling in Graphene p n Junctions", en, Physical Review Letters **102** (2009) 10.1103/PhysRevLett.102.026807.

[27]V. V. Cheianov and V. I. Falko, "Selective transmission of Dirac electrons and ballistic magnetoresistance of n p junctions in graphene", en, Physical Review B **74** (2006) 10.1103/PhysRevB.74.041403.

[28]A. V. Shytov, M. S. Rudner, and L. S. Levitov, "Klein Backscattering and Fabry-Prot Interference in Graphene Heterojunctions", en, Physical Review Letters **101** (2008) 10.1103/PhysRevLett.101.156804.

[29]N. Gu and others, "Relativistic dynamics and Dirac particles in graphene", PhD thesis (Massachusetts Institute of Technology, 2011).

[30]E. McCann and V. I. Falko, "Landau-Level Degeneracy and Quantum Hall Effect in a Graphite Bilayer", en, Physical Review Letters **96** (2006) 10.1103/PhysRevLett.96.086805.

[31]Y. Zhang, T.-T. Tang, C. Girit, Z. Hao, M. C. Martin, A. Zettl, M. F. Crommie, Y. R. Shen, and F. Wang, "Direct observation of a widely tunable bandgap in bilayer graphene", Nature **459**, 820–823 (2009).

[32]S. Park and H.-S. Sim, " Berry phase and Veselago lens in a bilayer graphene n p junction", en, Physical Review B **84** (2011) 10.1103/PhysRevB.84.235432.

[33]G. M. Rutter, S. Jung, N. N. Klimov, D. B. Newell, N. B. Zhitenev, and J. A. Stroscio, "Microscopic polarization in bilayer graphene", Nature Physics **7**, 649–655 (2011).

[34]M. Yankowitz, J. I.-J. Wang, S. Li, A. G. Birdwell, Y.-A. Chen, K. Watanabe, T. Taniguchi, S. Y. Quek, P. Jarillo-Herrero, and B. J. LeRoy, "Band structure mapping of bilayer graphene via quasiparticle scattering", en, APL Materials **2**, 092503 (2014).

[35]A. Varlet, M.-H. Liu, D. Bischoff, P. Simonet, T. Taniguchi, K. Watanabe, K. Richter, T. Ihn, and K. Ensslin, "Band gap and broken chirality in single-layer and bilayer graphene", en, physica status solidi (RRL) - Rapid Research Letters **10**, 46–57 (2016).

[36]A. Matulis and F. M. Peeters, "Quasibound states of quantum dots in single and bilayer graphene", en, Physical Review B **77** (2008) 10.1103/PhysRevB.77.115423.

[37]J. M. Pereira, P. Vasilopoulos, and F. M. Peeters, "Tunable Quantum Dots in Bilayer Graphene", en, Nano Letters **7**, 946–949 (2007).

[38]J. Bardeen, "Tunnelling from a Many-Particle Point of View", en, Physical Review Letters **6**, 57–59 (1961).

[39]J. Tersoff and D. R. Hamann, "Theory and application for the scanning tunneling microscope", Physical review letters **50**, 1998 (1983).

[40]J. Tersoff and D. R. Hamann, "Theory of the scanning tunneling microscope", en, Physical Review B **31**, 805–813 (1985).

[41]T. Taniguchi and K. Watanabe, "Synthesis of high-purity boron nitride single crystals under high pressure by using BaBN solvent", en, Journal of Crystal Growth **303**, 525–529 (2007).

[42]C. R. Dean, A. F. Young, I. Meric, C. Lee, L. Wang, S. Sorgenfrei, K. Watanabe, T. Taniguchi, P. Kim, K. L. Shepard, and J. Hone, "Boron nitride substrates for high-quality graphene electronics", Nature Nanotechnology **5**, 722–726 (2010).

[43]L. Britnell, R. M. Ribeiro, A. Eckmann, R. Jalil, B. D. Belle, A. Mishchenko, Y.-J. Kim, R. V. Gorbachev, T. Georgiou, S. V. Morozov, A. N. Grigorenko, A. K. Geim, C. Casiraghi, A. H. C. Neto, and K. S. Novoselov, "Strong Light-Matter Interactions in Heterostructures of Atomically Thin Films", en, Science **340**, 1311–1314 (2013).

[44]K. Watanabe, T. Taniguchi, and H. Kanda, "Direct-bandgap properties and evidence for ultraviolet lasing of hexagonal boron nitride single crystal", Nature Materials **3**, 404–409 (2004).

[45]Z. Remes, M. Nesladek, K. Haenen, K. Watanabe, and T. Taniguchi, "The optical absorption and photoconductivity spectra of hexagonal boron nitride single crystals", en, physica status solidi (a) **202**, 2229–2233 (2005).

[46]L. Ju, J. Velasco, E. Huang, S. Kahn, C. Nosiglia, H.-Z. Tsai, W. Yang, T. Taniguchi, K. Watanabe, Y. Zhang, G. Zhang, M. Crommie, A. Zettl, and F. Wang, "Photoinduced doping in heterostructures of graphene and boron nitride", Nature Nanotechnology **9**, 348–352 (2014).

[47]J. Xue, J. Sanchez-Yamagishi, D. Bulmash, P. Jacquod, A. Deshpande, K. Watanabe, T. Taniguchi, P. Jarillo-Herrero, and B. J. LeRoy, "Scanning tunnelling microscopy and spectroscopy of ultra-flat graphene on hexagonal boron nitride", Nature Materials **10**, 282–285 (2011).

[48]R. Decker, Y. Wang, V. W. Brar, W. Regan, H.-Z. Tsai, Q. Wu, W. Gannett, A. Zettl, and M. F. Crommie, "Local Electronic Properties of Graphene on a BN Substrate via Scanning Tunneling Microscopy", en, Nano Letters **11**, 2291–2295 (2011).

[49]Y. Zhang, V. W. Brar, F. Wang, C. Girit, Y. Yayon, M. Panlasigui, A. Zettl, and M. F. Crommie, "Giant phonon-induced conductance in scanning tunnelling spectroscopy of gate-tunable graphene", Nature Physics **4**, 627–630 (2008).

[50]D. Wong, J. Velasco, L. Ju, J. Lee, S. Kahn, H.-Z. Tsai, C. Germany, T. Taniguchi, K. Watanabe, A. Zettl, F. Wang, and M. F. Crommie, "Characterization and manipulation of individual defects in insulating hexagonal boron nitride using scanning tunnelling microscopy", Nature Nanotechnology **10**, 949–953 (2015).

[51]Y. Wang, V. W. Brar, A. V. Shytov, Q. Wu, W. Regan, H.-Z. Tsai, A. Zettl, L. S. Levitov, and M. F. Crommie, "Mapping Dirac quasiparticles near a single Coulomb impurity on graphene", Nature Physics **8**, 653–657 (2012).

[52]K. Teichmann, M. Wenderoth, S. Loth, R. G. Ulbrich, J. K. Garleff, A. P. Wijnheijmer, and P. M. Koenraad, "Controlled Charge Switching on a Single Donor with a Scanning Tunneling Microscope", en, Physical Review Letters **101** (2008) 10.1103/PhysRevLett.101.076103.

[53]V. W. Brar, R. Decker, H.-M. Solowan, Y. Wang, L. Maserati, K. T. Chan, H. Lee,. O. Girit, A. Zettl, S. G. Louie, M. L. Cohen, and M. F. Crommie, "Gate-controlled ionization and screening of cobalt adatoms on a graphene surface", Nature Physics **7**, 43–47 (2011).

[54]M. Scheffler, D. Haberer, L. Petaccia, M. Farjam, R. Schlegel, D. Baumann, T. Hnke, A. Grneis, M. Knupfer, C. Hess, and B. Bchner, "Probing Local Hydrogen Impurities in Quasi-Free-Standing Graphene", en, ACS Nano **6**, 10590–10597 (2012).

[55]M. Fanciulli and T. Moustakas, "Study of defects in wide band gap semiconductors by electron paramagnetic resonance", en, Physica B: Condensed Matter **185**, 228–233 (1993).

[56]A. Katzir, J. T. Suss, A. Zunger, and A. Halperin, "Point defects in hexagonal boron nitride. I. EPR, thermoluminescence, and thermally-stimulated-current measurements", en, Physical Review B **11**, 2370–2377 (1975).

[57]E. Y. Andrei, A. Katzir, and J. T. Suss, "Point defects in hexagonal boron nitride. III. EPR in electron-irradiated BN", en, Physical Review B **13**, 2831–2834 (1976).

[58]A. Zunger and A. Katzir, "Point defects in hexagonal boron nitride. II. Theoretical studies", en, Physical Review B **11**, 2378–2390 (1975).

[59]C. Attaccalite, M. Bockstedte, A. Marini, A. Rubio, and L. Wirtz, "Coupling of excitons and defect states in boron-nitride nanostructures", en, Physical Review B **83** (2011) 10.1103/PhysRevB.83.144115.

[60]S. Das Sarma, S. Adam, E. H. Hwang, and E. Rossi, "Electronic transport in two-dimensional graphene", en, Reviews of Modern Physics **83**, 407–470 (2011).

[61]M. T. Woodside, "Scanned Probe Imaging of Single-Electron Charge States in Nanotube Quantum Dots", Science **296**, 1098–1101 (2002).

[62]N. A. Pradhan, N. Liu, C. Silien, and W. Ho, "Atomic Scale Conductance Induced by Single Impurity Charging", en, Physical Review Letters **94** (2005) 10.1103/PhysRevLett.94.076801.

[63]N. Kharche and S. K. Nayak, "Quasiparticle Band Gap Engineering of Graphene and Graphone on Hexagonal Boron Nitride Substrate", en, Nano Letters **11**, 5274–5278 (2011).

[64]J. K. Garleff, A. P. Wijnheijmer, C. N. v. d.Enden, and P. M. Koenraad, "Bistable behavior of silicon atoms in the (110) surface of gallium arsenide", en, Physical Review B **84** (2011) 10.1103/PhysRevB.84.075459.

[65]J. Repp, G. Meyer, F. E. Olsson, and M. Persson, "Controlling the charge state of individual gold adatoms", Science **305**, 493–495 (2004).

[66]J. Velasco, L. Ju, D. Wong, S. Kahn, J. Lee, H.-Z. Tsai, C. Germany, S. Wickenburg, J. Lu, T. Taniguchi, K. Watanabe, A. Zettl, F. Wang, and M. F. Crommie, "Nanoscale Control of Rewriteable Doping Patterns in Pristine Graphene/Boron Nitride Heterostructures", en, Nano Letters **16**, 1620–1625 (2016).

[67]J.-S. Wu and M. M. Fogler, "Scattering of two-dimensional massless Dirac electrons by a circular potential barrier", en, Physical Review B **90** (2014) 10.1103/PhysRevB.90.235402.

[68]C. Schulz, R. L. Heinisch, and H. Fehske, "Scattering of two-dimensional Dirac fermions on gate-defined oscillating quantum dots", en, Physical Review B **91** (2015) 10.1103/PhysRevB.91.045130.

[69]H.-Y. Chen, V. Apalkov, and T. Chakraborty, "Fock-Darwin States of Dirac Electrons in Graphene-Based Artificial Atoms", en, Physical Review Letters **98** (2007) 10.1103/PhysRevLett.98.186803.

[70]J. H. Bardarson, M. Titov, and P. W. Brouwer, "Electrostatic Confinement of Electrons in an Integrable Graphene Quantum Dot", en, Physical Review Letters **102** (2009) 10.1103/PhysRevLett.102.226803.

[71]M. F. Crommie, C. P. Lutz, and D. M. Eigler, "Confinement of electrons to quantum corrals on a metal surface", Science **262**, 218–220 (1993).

[72]M. M. Fogler, D. S. Novikov, and B. I. Shklovskii, "Screening of a hypercritical charge in graphene", en, Physical Review B **76** (2007) 10.1103/PhysRevB.76.233402.

[73]W. G. van der Wiel, S. De Franceschi, J. M. Elzerman, T. Fujisawa, S. Tarucha, and L. P. Kouwenhoven, "Electron transport through double quantum dots", en, Reviews of Modern Physics **75**, 1–22 (2002).

[74]R. Hanson, L. P. Kouwenhoven, J. R. Petta, S. Tarucha, and L. M. K. Vandersypen, "Spins in few-electron quantum dots", en, Reviews of Modern Physics **79**, 1217–1265 (2007).

[75]D. Loss and D. P. DiVincenzo, "Quantum computation with quantum dots", en, Physical Review A **57**, 120–126 (1998).

[76]C.-H. Park, L. Yang, Y.-W. Son, M. L. Cohen, and S. G. Louie, "New Generation of Massless Dirac Fermions in Graphene under External Periodic Potentials", en, Physical Review Letters **101** (2008) 10.1103/PhysRevLett.101.126804.

[77]H. C. Manoharan, C. P. Lutz, and D. M. Eigler, "Quantum mirages formed by coherent projection of electronic structure", Nature **403**, 512–515 (2000).

[78]E. J. Heller, M. F. Crommie, C. P. Lutz, and D. M. Eigler, "Scattering and absorption of surface electron waves in quantum corrals", en, Nature **369**, 464–466 (1994).

[79]E. J. Heller, "Bound-State Eigenfunctions of Classically Chaotic Hamiltonian Systems: Scars of Periodic Orbits", en, Physical Review Letters **53**, 1515–1518 (1984).

[80]H. Xu, L. Huang, Y.-C. Lai, and C. Grebogi, "Chiral Scars in Chaotic Dirac Fermion Systems", en, Physical Review Letters **110** (2013) 10.1103/PhysRevLett.110.064102.

[81]R. V. Jensen, "Quantum chaos", en, Nature **355**, 311–318 (1992).

[82]C. M. Marcus, A. J. Rimberg, R. M. Westervelt, P. F. Hopkins, and A. C. Gossard, "Conductance fluctuations and chaotic scattering in ballistic microstructures", en, Physical Review Letters **69**, 506–509 (1992).

[83]P. B. Wilkinson, T. M. Fromhold, L. Eaves, F. W. Sheard, N. Miura, and T. Takamasu, "Observation of 'scarred' wavefunctions in a quantum well with chaotic electron dynamics", en, Nature **380**, 608–610 (1996).

[84]R. Crook, C. G. Smith, A. C. Graham, I. Farrer, H. E. Beere, and D. A. Ritchie, "Imaging Fractal Conductance Fluctuations and Scarred Wave Functions in a Quantum Billiard", en, Physical Review Letters **91** (2003) 10.1103/PhysRevLett.91.246803.

[85]R. Nandkishore and L. Levitov, "Common-path interference and oscillatory Zener tunneling in bilayer graphene pn junctions", Proceedings of the National Academy of Sciences **108**, 14021–14025 (2011).

[86]M. T. Allen, J. Martin, and A. Yacoby, "Gate-defined quantum confinement in suspended bilayer graphene", Nature Communications **3**, 934 (2012).

[87]D. Wong, Y. Wang, J. Jung, S. Pezzini, A. M. DaSilva, H.-Z. Tsai, H. S. Jung, R. Khajeh, Y. Kim, J. Lee, S. Kahn, S. Tollabimazraehno, H. Rasool, K. Watanabe, T. Taniguchi, A. Zettl, S. Adam, A. H. MacDonald, and M. F. Crommie, "Local spectroscopy of moir-induced electronic structure in gate-tunable twisted bilayer graphene", en, Physical Review B **92** (2015) 10.1103/PhysRevB.92.155409.

[88]A. E. Hanna and M. Tinkham, "Variation of the Coulomb staircase in a two-junction system by fractional electron charge", Physical review B **44**, 5919 (1991).

[89]N. M. Freitag, L. A. Chizhova, P. Nemes-Incze, C. R. Woods, R. V. Gorbachev, Y. Cao, A. K. Geim, K. S. Novoselov, J. Burgdrfer, F. Libisch, and M. Morgenstern, "Electrostatically Confined Monolayer Graphene Quantum Dots with Orbital and Valley Splittings", en, Nano Letters **16**, 5798–5805 (2016).

[90]L. L. Sohn, L. P. Kouwenhoven, and G. Schn, eds., *Mesoscopic Electron Transport*, DOI: 10.1007/978-94-015-8839-3 (Springer Netherlands, Dordrecht, 1997).

[91]D. V. Averin, A. N. Korotkov, and K. K. Likharev, "Theory of single-electron charging of quantum wells and dots", Physical Review B **44**, 6199 (1991).